Technische Universität München

Fakultät für Informatik

Dissertation

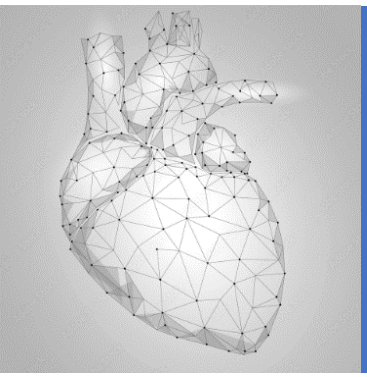

Application of image registration in cardiac T1 mapping and strain analysis

Shufang Liu

Technische Universität München
Fakultät für Informatik

Application of image registration in cardiac T1 mapping and strain analysis

Shufang Liu

Vollständiger Abdruck der von der Fakultät für Informatik der Technischen Universität München zur Erlangung des akademischen Grades einer

Doktorin der Naturwissenschaften (Dr. rer. nat.)

genehmigten Dissertation.

Vorsitzender: Prof. Dr.-Ing. Georg Carle

Prüfende(r) der Dissertation: 1. Prof. Dr.-Ing. Darius Burschka

2. Priv.-Doz. Dr. Marion I. Menzel

Die Dissertation wurde am 10.06.2021 bei der Technischen Universität München eingereicht und durch die Fakultät für Informatik am 19.01.2022 angenommen.

Abstract

Magnetic resonance imaging is the gold standard for cardiac diseases diagnosis because of the variability of sequences and good interobserver agreement. In recent years, new imaging technologies, e.g. T_1 mapping, MR Fingerprinting, compressed sensing, have emerged. Therefore, investigations in post-processing and clinical workflow are needed to (i) extract new quantitative parameters, which can better characterize pathology or better evaluate the severity of diseases; (ii) improve the accuracy and precision (noise-robustness) of these parameters; (iii) deal with increasingly large data sets with computationally efficient algorithms. In this work, two subtopics were investigated, cardiac T_1 mapping and strain analysis. These two subtopics are important in cardiac MRI evaluation: T_1 mapping is the key imaging tool for tissue characterization, while strain analysis is the key technique for the functional assessment of the heart.

Cardiac T_1 mapping can provide quantitative measurement of the relaxation process of myocardial tissue. By measuring pre-contrast and post-contrast T_1 maps, extracellular volume can be determined. This is an important parameter for early detection of diffuse fibrosis, which cannot be detected with conventional methods such as delayed enhancement imaging. However, due to cardiac motion and limited time for image acquisition, the raw images are usually noisy and not well aligned. In this work, T_1 map computation was optimized in 3 aspects: 1) a vectorized Levenberg-Marquardt algorithm was proposed, 2) spatial regularization was added, 3) region-based initialization was applied. Simulation experiment was conducted to validate the vectorized Levenberg-Marquardt algorithm. Then, the proposed algorithm was validated on 28 patient data, with both pre-contrast and post-contrast images. The result showed improved robustness of T_1 estimation using vectorized Levenberg-Marquardt algorithm with spatial regularization and region-based initialization. In addition, performance improvement with GPU implementation was evaluated and showed higher computational efficiency. Finally, software for clinical use has been implemented.

Myocardial strain analysis is used for early detection of myocardial dysfunction. Currently, echography and tagged MRI are more widely used in clinical routine. However,

echography is usually limited by beam direction and tagged MRI has lower temporal resolution. Thanks to the recently developed super-resolution technique, 3D cine images of the heart are now available. Therefore, new data processing tool is needed. In this work, we proposed a 3D strain analysis framework, in which myocardial mask-based registration was used to extract dense motion field. Incompressibility regularization and rotation regularization were added to obtain physically plausible motion fields. Peak systolic strain and strain curves were then calculated on each pixel. The calculation framework was validated with simulation and clinical data of 18 Duchenne muscular dystrophy (DMD) patients. The 3D peak strain was first compared with global 2D strain. Significant differences were found in circumferential and radial strain, whereas the difference in longitudinal strain was not significant. Then comparison study between patients with fibrosis and without fibrosis was performed. For patients with fibrosis, circumferential strain in the septal and anterior regions showed significantly smaller values ($p<0.05$). The correlation between the regional strain curve and the average circumferential strain curve for those patients also showed significantly smaller values.

In summary, two clinical topics were investigated in this project, T1 mapping and myocardial strain analysis based on 3D cine image. Improved algorithms and workflows were proposed and validated for T1 mapping. First investigation on the validity of strain measurement using 3D cine images was performed and those 3D strain parameters could be potentially used as new imaging biomarkers for the assessment of DMD patients.

ZUSAMMENFASSUNG

Die Magnetresonanztomografie ist der Goldstandard für die Diagnose vieler Herzerkrankungen aufgrund der Vielfalt der Sequenzen und der guten Übereinstimmung zwischen verschiedenen Beobachtern. In den letzten Jahren sind viele neue Bildgebungstechnologien entstanden, z.B. T1-Mapping, MR-Fingerprinting und Compressed Sensing. Daher sind neuartige Untersuchungen in der Nachbearbeitung und im klinischen Arbeitsablauf erforderlich, um: (I) neue quantitative Informationen zu extrahieren, die die Pathologie besser charakterisieren können oder den Schweregrad der Krankheit besser einschätzen können, (II) die Genauigkeit und Präzision der Parameter zu verbessern; (III) die immer größeren Datenmengen mit rechnerisch effizienten Algorithmen zu verarbeiten. In dieser Arbeit wurden zwei Technologien bearbeitet: das kardiale T1-Mapping und die Strainanalyse des Herzmuskels. Die beiden Methoden sind wichtige Elemente in der MRT-Bewertung für Herzpatienten: Das T1-Mapping ist das wichtigste MR-Imaging-Tool für die Gewebecharakterisierung, während die Strainanalyse die Schlüsseltechnik für die Beurteilung der kontraktilen Funktion ist.

Das kardiale T1-Mapping kann quantitative Informationen über die Relaxationsprozesse von Myokardgewebe anbieten. Mittels T1-Map vor und nach Injektion von Kontrastmittel kann das extrazelluläre Volumen errechnet werden. Dies ist ein wichtiger Parameter für die Früherkennung der diffusen Fibrose, die mit einer herkömmlichen Bildgebung nicht erkennbar ist. Aufgrund der Herzbewegung und der begrenzten Zeit für die Bilderfassung sind die rohen Bilddaten normalerweise verrauscht und räumlich nicht registriert. In dieser Arbeit wird die T1-Mapping-Berechnung in drei Aspekten optimiert: 1) ein vektorisierter Levenberg-Marquardt-Algorithmus wird verwendet, 2) eine räumliche Regularisierung wird hinzugefügt, 3) eine Region-basierte Initialisierung wird durchgeführt. Der vektorisierte Levenberg-Marquardt-Algorithmus wurde durch ein Simulationsexperiment validiert. Anschließend wurde der Workflow anhand von 28 Patientendaten mit den Bildern sowohl vor als auch nach dem Kontrastmittelgabe validiert. Das Ergebnis zeigt eine verbesserte Robustheit der T1-Schätzung unter Verwendung eines vektorisierten Levenberg-Marquardt-Algorithmus mit räumlicher Regularisierung und Region-basierter Initialisierung. Darüber hinaus wird eine GPU-

Implementierung verwendet, die eine verbesserte Berechnungseffizienz aufweist. Die Software wurde anschließend für den klinischen Einsatz implementiert.

Die myokardiale Strainanalyse wird zur früheren Erkennung von Myokardfunktionsstörungen verwendet. Derzeit werden dafür in der klinischen Anwendung häufig Echografie und getaggte MRT Bilder eingesetzt. Die Echografie ist jedoch normalerweise durch die Strahlrichtung begrenzt und die getaggten MRT Bilder haben eine relativ geringe zeitliche Auflösung. Dank der kürzlich entwickelten Super-Resolution-Technik sind nun 3D-Cine Bilder des Herzens verfügbar, für die neue Datenverarbeitungsmethoden notwendig sind. In dieser Arbeit wurde ein Strainanalyse-Rahmen auf Grundlage von 3D-Cine vorgeschlagen, in welchem ein Registrierung auf Basis von Myokardmasken verwendet wurde, um das Bewegungsfeld zu extrahieren. Inkompressibilitätsregulierung und Rotationsregulierung wurden hinzugefügt, um physikalisch plausible Bewegungsfelder zu erhalten. Der maximale systolische 3D-PeakStrain und die 2D-Strainkurven wurden danach berechnet. Der vorgeschlagene Workflow wurde durch Simulationen und an Daten von 18 Patienten mit Duchenne-Muskeldystrophie (DMD) validiert. Der systolische 3D-Peak-Strain wurde zunächst mit dem globalen 2D-Strain verglichen. Es gab signifikante Unterschiede im Strain in Umfangsrichtung und in radialer Richtung, während der Unterschied in longitudinaler Richtung nicht signifikant war. Dann wurde der 3D-Strain zwischen den DMD-Patienten mit und ohne Fibrose verglichen. Die Strain in Umfangsrichtung im Septum- und Anteriorbereich zeigte bei Patienten mit Fibrose signifikant geringere Werte ($p<0.05$). Die Korrelation zwischen der regionalen Strainkurve und der durchschnittlichen Strainkurve in Umfangsrichtung ergab ebenfalls einen deutlich kleineren Wert.

Zusammenfassend wurden in diesem Projekt zwei klinische Themen untersucht: T_1-Mapping und myokardiale Strainanalyse auf der Basis von 3D-Cine Bildern. Für das T_1-Mapping wurden verbesserte Algorithmen und Workflows vorgeschlagen und validiert. Erste Untersuchungen zur Validität der Strain-Messungen an 3D-Cine Bildern wurden durchgeführt und zeigen vielversprechende Parameter, die als neue bildgebende Biomarker für die Bewertung von DMD-Patienten verwendet werden könnten.

Acknowledgement

First of all, I would like to thank Marie Curie project for funding this project and thank BERTI for offering me this opportunity to investigate further in cardiac MRI. Next, I would like to thank Prof. Darius Burschka, Dr. Freddy Odille and Dr. Timo Schirmer for this interesting research proposal. I would also like to thank TUM for hosting and providing infrastructure during my PhD project.

During my external stay in the research lab IADI in Brabois hospital in Nancy, I had really enjoyable research experience and very happy to work with colleagues there. I would like to thank Prof. Jacques Felblinger, Dr. Freddy Odille, Dr. Bailiang Chen, Dr. Pierre-Andre Vissoz for the supervision and discussion. Dr. Pauline Ferry and Dr. Laurent Bonnemains provided important clinical data for my work. It is also very nice to meet Dr. Lin Zhang, Dr. Yu Xie, Dr. Sarra Aissani, Dr. Andre Guillou.

Colleagues in GE Global Research Center also helped me a lot during this work. Thank Dr. Anne Menini for discussions and suggestions during the daily work. Those suggestions are very helpful for me to understanding the problem and to further validate my work. Thank Dr. Ana BeatrizSolana, Dr. Guido Kudielka for discussions and helps.

Finally, but most importantly I would like to thank my parents for their support and understanding during my PhD project. And I would like to thank all my friends for their encourage and help.

Contents

Chapter 1 Introduction

1.1 MOTIVATION

Cardiovascular disease (CVD) is the leading cause of death worldwide. Every year, more than 17.3 million people die due to cardiovascular disease[1]. According to the statistic report by European heart network in 2017, the economic cost is approximately €210 per year, which includes healthcare costs (€111 billion), productivity lost (€54) and other informal care costs[2].

Cardiovascular diseases can be divided into atherosclerosis caused diseases and other cardiovascular diseases. Among all CVD deaths, atherosclerosis accounts for more than 70% of deaths [3]. Atherosclerosis is caused by the artery narrowing. It can progressively lead to coronary artery disease, stroke and peripheral artery disease. However, 80% of premature heart disease and stroke can be prevented and early diagnosis is critical.

Nuclear magnetic resonance was first detected by Erwin Hahn in the 1950s and 2D imaging using gradient was invented by Paul Lauterbur in 1973. Since the invention of MRI, it has been widely used in different areas. Numerous studies and researches have been conducted to obtain high quality images and to improve clinical diagnosis. It has gradually become the gold standard for cardiovascular disease analysis. Compared to other imaging techniques, MRI has the following advantages:

- Good contrast between different soft tissues
- Versatile sequence to provide various diagnostic information
- High reproducibility and accuracy
- Non-radioactive
- Less dependent on user operation

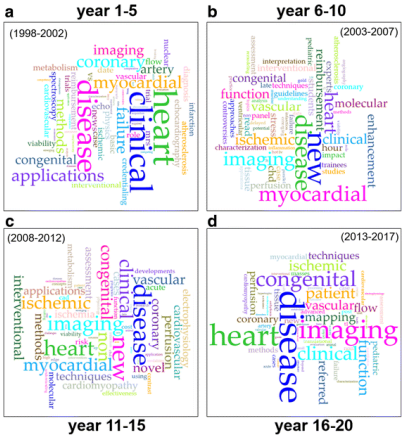

Figure 1. Word clouds visualizing the frequency of words used in SCMR scientific session titles over past 20 years. [4]

"clinical" and "diseases" have always been the focus during the development of MRI[4]. To answer the clinical questions, different protocols have been developed. The routinely performed protocols are "Left ventricle function and scar/fibrosis protocol" and "Myocardial stress perfusion protocol" [5]. The analysis of MR images in these clinical protocols includes:

i. Cardiac contractile function quantification. This is the basic analysis during cardiac MR examination. The mechanical property of the heart can be estimated by volumetric analysis in systolic/diastolic phases, flow calculations, visual assessment of segmental contraction or wall thickening from cine images etc. Parameters routinely measured include ejection fraction, wall thickness, wall thickening, segmental strain, etc. In addition to volumetric analysis, global longitudinal strain has been proved to be a more sensitive measure of systolic function than ejection fraction and can be used to identify subclinical LV dysfunction in cardiomyopathies.

ii. Myocardial tissue characterization. This technique is used to distinguish between healthy and abnormal tissue, such as edema, infarction, scar or fibrosis. MRI data can be used as imaging biomarkers to make an early diagnosis of myocardial disease, to decide which treatment should be given, or to provide an early prediction of the patient's long-term outcome[6]. Late gadolinium enhancement is the first MR technique developed to differentiate between ischemic heart disease and non-ischemic heart disease. Parametric maps are later developed to provide quantitative measurement. One of the most important parametric

mappings for estimating myocardial composition is T_1 mapping. The increase in T_1 value is accompanied by many cardiac diseases, including myocardial infarction, myocarditis, hypertrophic and dilated cardiomyopathy etc[7]. The changes in T_1 values may also indicate structural changes in tissues, e.g. a remodeling process, which may have long-term consequences on cardiac function. T_2 mapping can be used to quantify edema and the extent of inflammation, which is an important indicator of myocardial infarction, myocarditis, graft rejection, etc [8]. Besides parametric mappings, local strain analysis is another widely used tool for tissue characterization. The changes in local myocardial strain may occur before the global cardiac function change. Therefore, strain analysis can be used for early diagnosis of heart failure. Another application of local strain analysis is to guide the placement of LV pacing leads for patients in the cardiac resynchronization therapy.

iii. Perfusion analysis. This examination is performed as a further investigation for patients with suspected ischemia. The first pass of gadolinium-based contrast is imaged, under stressed- and rest- conditions. Perfusion analysis can predict the risk of developing cardiac events after treatment[9].

In cardiac MRI, one special problem is motion. On the one hand, myocardial contractile function is an important parameter to evaluate the heart function. On the other hand, myocardial motion is a big challenge to obtain high quality image and accurate measurements. In this research, the motion problem in T_1 mapping and strain analysis were investigated with the help of image processing. These two technologies are key components in cardiac MRI evaluation.

- T_1 mapping is the most important MR imaging tool for tissue characterization. Compared with other imaging methods, T_1 mapping can provide quantitative measurement and allow early detection of myocardial fibrosis, which can limit the supply of oxygen and nourishment to the myocardium and eventually lead to ischemia or heart failure. Although different sequences and data processing methods have been proposed and evaluated, the workflow in clinical routine still needs to be optimized. A critical problem that prevents accurate measurement in clinical workflow is image noise. Figure 2 shows an example data series acquired

for T_1 mapping. In general, the images have lower signal-to-noise ratio than normal cine images. This is partly caused by the limited acquisition time and relative slow relaxation process. Another problem is the cardiac motion. Although many motion control methods, such as breath holding and ECG-gating, have been applied and advanced image reconstruction technologies, such as motion corrected reconstruction([10,11]), have been used, the myocardium regions are still deformed and misaligned. Both the noise and the misalignment lead to inaccurate assessment of the myocardial tissue. Therefore, improvement of post-processing steps is needed. Currently, most work on T_1 mapping focused on one particular step, such as improving acquisition sequence[12] or using additional information for motion correction[13]. In this study, we examined the entire T_1 mapping workflow and identified several steps that could be optimized.

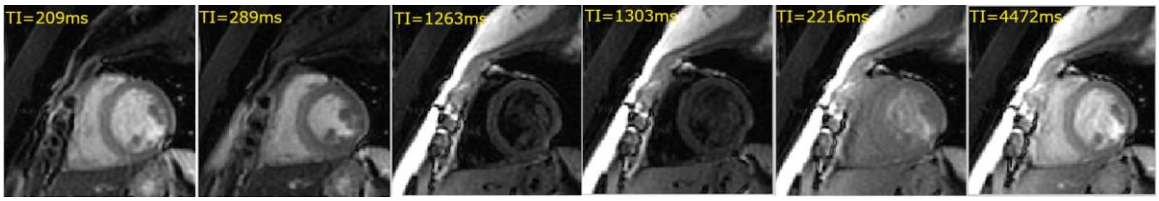

Figure 2. An example T_1 series sampled at different inversion time

- Another important parameter for the evaluation of ischemic disease is myocardial strain. Evaluation techniques have evolved from echocardiography to 2D MRI image based analysis, then to tissue Doppler measurement with speckle tracking. Currently, most researches are performed on echography or tagged MRI[14]. Cine MRI has been proved to be an key technique for the assessment of cardiac anatomy and contractile function. However there are not many researches for strain analysis based on cine images. The clinically available cine data are usually 2D images, and analysis based on 2D images is subject to through-plan motion, which makes the evaluation less accurate. Recent improvements in MRI make 3D cine images available for clinical use. We would like to investigate how well is 3D cine based strain compared to conventional 2D strain and whether 3D cine based strain can be used to assess myocardial properties. The challenge in strain analysis using 3D cine images is to calculate the dense motion field, which is then used to calculate myocardial strain. In this study, 3D cine images were analyzed and the application in Duchenne muscular dystrophy diagnosis was evaluated.

The main contributions in this research are:

- T_1 mapping workflow was optimized in several aspects. A vectorized Levenberg Marquardt algorithm was proposed to make the T_1 mapping workflow more resistant to image noise by applying spatial regularization. Region-based initialization and efficient non-rigid image registration were incorporated to further improve the measurement. Those post-processing steps for T_1 mapping were evaluated with simulation and patient data. In addition, a clinical software was implemented for large scale study use and the vectorized Levenberg Marquardt algorithm was further optimized on GPU.
- Strain analysis based on 3D cine images was investigated and a framework for calculating strain was proposed. In this framework, a non-rigid image registration with incompressibility regularization in myocardium was proposed to obtain more physically meaningful motion field. Simulation experiments were performed to evaluate the proposed framework. The estimated 3D strain was compared to the 2D strain using clinical data. A correlation index is derived from strain curve, and could potentially be used as a new parameter to estimate the severity of Duchenne muscular dystrophy.

1.2 OUTLINE

Chapter 2 and Chapter 3 describe the technical background. In Chapter 2, MRI physics and cardiac imaging techniques are briefly introduced. Different imaging modalities and sequences are described to give a better overview of clinical application in the cardiac area. Chapter 3 describes the basic framework and regularization schemes for medical image registration. Image registration is a key tool in this thesis, as it is necessary to correct the spatial misalignment so that reliable T_1 mapping can be obtained. It is also necessary for strain analysis, not to correct but to measure accurately the cardiac motion pattern throughout the cardiac cycle.

Chapter 4 describes the optimized T_1 mapping workflow. Vectorized Levenberg-Marquardt algorithm with spatial regularization and region-based initialization was proposed to improve the curve fitting in T_1 mapping calculation. In addition, GPU implementation was proposed and compared to CPU implementation. In Chapter 6,

experiments to evaluate the optimized steps were performed, including image registration, region-based initialization and vectorized curve fitting. The accuracy of vectorized curve fitting was first validated with simulation experiments and then with clinical data for both native and post-contrast T_1 mapping.

In Chapter 5, a myocardial strain analysis framework for 3D cine images was proposed. Novel regularization schemes were proposed to obtain physically plausible solutions for the displacement field. Chapter 7 presents the evaluation of the proposed framework. 3D global strain was first compared with conventional 2D global strain. Then the 3D strain between different patient groups were compared. We also investigated novel indices derived from the 3D deformation patterns throughout the cardiac cycle (strain curves) to better characterize local abnormalities in cardiac contraction.

Finally, in Chapter 8 gives a summary of the work and future direction.

Chapter 2 Cardiac MRI

In this chapter, MRI physics and imaging principle are introduced to provide basic background. Important MR sequences for cardiac analysis and their clinical application are described in more detail.

2.1 MRI PHYSICS AND IMAGING

2.1.1 MRI PHYSICS

Moving electric particles, like protons, can produce a magnetic field. This is characterized by a property called spin, which can be interpreted as the rotation of the particle around some axis. A spin can be seen macroscopically as a magnetic dipole. Normally, if we consider a population of spins, their orientations are randomly distributed, as a result their net magnetization is null. If they are subjected to an external magnetic field B_0, the spins will undergo a precession motion (like a gyroscope) around the axis of the external field, characterized by the Larmor frequency ω_0, which is also called resonance frequency:

$$\omega_0 = \gamma \cdot B_0$$

Normally the B_0 direction is defined as Z-direction and the plane perpendicular to B_0 is defined as XY-plane. After applying B_0 the net magnetization is aligned with the direction of B_0. If an external radiofrequency pulse at the resonance frequency is further applied, the spin will absorb the energy and tilt down towards XY-plan. Meanwhile, as the spins deviate from the external field, the net magnetization begins to precess around the B_0 direction. After the removal of the radio frequency, the spins will return to lower energy state and return to Z-direction. This process is called relaxation. There are two types of relaxation, longitudinal relaxation (spin-lattice relaxation) and transverse relaxation (spin-spin relaxation). The longitudinal relaxation is related to the loss of the signal intensity and the transverse relaxation is related to the dispersion of the signal.

2.1.2 LONGITUDINAL RELAXATION

The longitudinal relaxation can be described by an exponential curve characterized by a time constant, T_1. This time constant is affected by the type of tissue, external magnetic field and presence of a contrast agency. The exponential curve can be described as

$$M_z(t) = M_{z,eq} - [M_{z,eq} - M_z(0)]e^{-\frac{t}{T_1}}$$

$M_z(0)$ is the Z-component of the magnetization at time 0 (right after application of the radiofrequency pulse) and $M_{z,eq}$ is the magnetization at equilibrium state. $M_z(0)$ is determined by the flip angle. If the flip angle is 90°, then $M_z(0) = 0$,

$$M_z(t) = M_{z,eq} \cdot (1 - e^{-\frac{t}{T_1}})$$

2.1.3 TRANSVERSE RELAXATION

As the external radio frequency pulse is removed, the tilted spins start to return to the initial state. Meanwhile, the spins get dephased, which is called T_2 relaxation. The signal also follows an exponential curve, and the time constant is denoted as T_2. In practice, because the external magnetic field is not perfectly homogeneous spatially, the observed relaxation has an actual time constant that is shorter than T_2, denoted as T_2*.

$$\mathrm{M_{xy}} = \mathrm{M_{xy}}(0) \cdot e^{-\frac{1}{T_2}}$$

$$\frac{1}{T_2^*} = \frac{1}{T_2} + \frac{1}{T_{inhom}} = \frac{1}{T_2} + \gamma \Delta B_0$$

2.1.4 IMAGING FORMATION

2.1.4.1 SLICE SELECTION

The Larmor frequency is affected by the strength of the external field. This can be used to selectively activate the spins at certain locations. For example, one can apply a magnetic field gradient in the z direction. Then, the spins with different z locations will rotate at different speeds, $\omega_0 > \omega_1 > \omega_2 > \omega_3$, as shown in the Figure 3. If we apply a radiofrequency pulse at ω_1, then only the spins at this z location will be flipped.

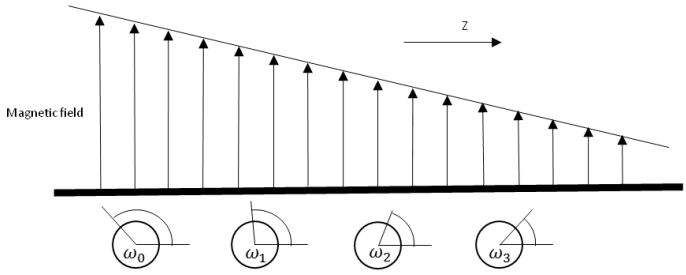

Figure 3. Illustration of slice selection by applying a magnetic field gradient

2.1.4.2 FREQUENCY ENCODING

After the remove the Z-direction gradient, the spins at z_1 location start the relaxation process. If we apply a magnetic field gradient in the x-direction, then the spins with different x locations send out signals with different frequencies. The received signal is the sum of all the spins. With Fourier transform, the signal can be decoded. The locations of the spins are encoded by the frequency of the signal.

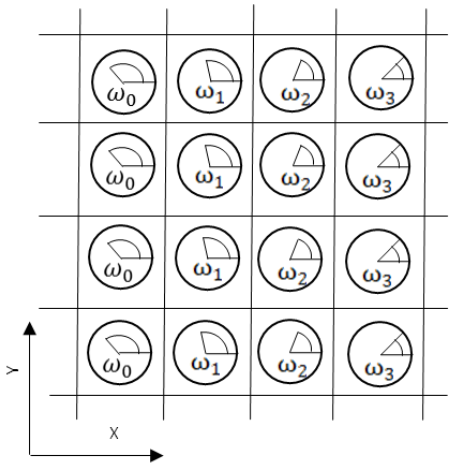

Figure 4. Illustration of frequency encoding

2.1.4.3 PHASE ENCODING

In order to encode the y-direction, the phase of the signal can be used. This can be archived by adding an additional gradient for a short time period before the frequency encoding, so the start position of the spin is depend on the location in y-direction.

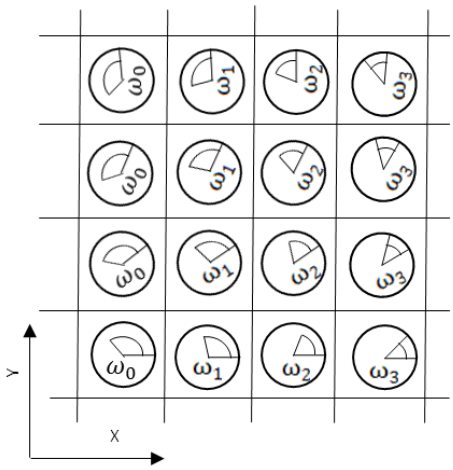

Figure 5. Illustration of phase encoding

By changing the magnitude of the gradient, the initial phase difference can be set differently. This y-direction phase encoding needs to be performed many times so that each pixel has a specific phase and frequency. All the data acquired are placed in a matrix, which is named as k-space. By doing inverse Fourier transform of this matrix, the target image can be obtained.

2.1.4.4 IMAGE CONTRAST

The image intensity depends on the relative density of the water protons and the relaxation times. Therefore there are three main types of image contrasts:

- proton density weighted image: Higher brightness means higher density of protons, this is achieved by using long repetition time (2000-5000ms) and short echo time (10-20ms)
- T_1 weighted image : The image contrast is depending on the T_1 relaxation time, therefore can be used to identify fat tissue or get morphological information. This is achieved by using short repetition time and short echo time.
- T_2 weighted image : The image contrast reflect the transverse relaxation. By using long repetition time and echo time. This type of image can be used to detect edema and inflammation.

2.1.4.5 ACQUISITION SEQUENCES

There are variety of sequences for different application, however, they can generally be divided as two families: gradient echo and spin echo.

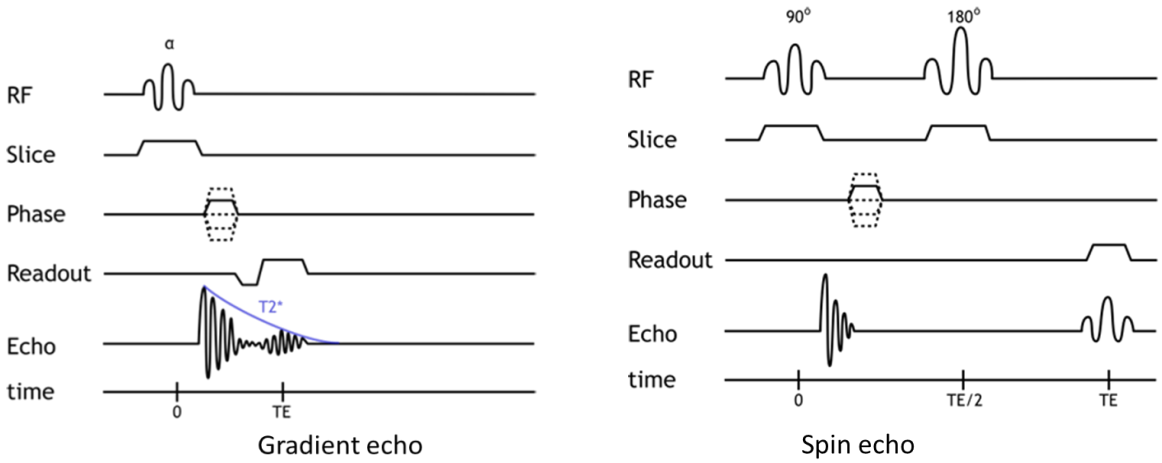

Figure 6. Illustration of Gradient echo sequence and Spin echo sequence. (left) Gradient Echo sequence; (right) Spin Echo sequence.

The gradient Echo sequence is composed of one RF pulse, a dephasing gradient, which followed by the rephrasing gradient of opposite polarity, and a readout gradient (Figure 6). The dephasing gradient causes an accelerated decay of the signal and the rephrasing gradient resynchronizes the signal. There are two types of gradient echo sequences:

- Spoiled Gradient echo: The residual transverse magnetization signal is destroyed by an additional dephasing gradient or by changing the phase of the RF pulse from one repetition to the next. Typical sequences include FLASH, TurboFLASH etc.
- Steady-State Gradient echo: The residual transverse magnetization signal is not destroyed but refocused. After a few repetition, a steady state of longitudinal and transverse signal is reached, which is called steady state free precession (SSFP). Typical sequences include FISP, PSIF etc. One widely used gradient echo sequence in cardiac applications is Balanced Steady-State Free Precession (bSSFP).

The other type of sequence is Spin-Echo sequence, which contains two RF pulses, as shown in Figure 6. The first 90˚ RF pulse flips the spins to the transverse plan, then the spins dephase with a T_2* time constant due to the inhomogeneity of the magnetic field. The 180˚ RF pulse reverses the phase of the spins, so that the spins are refocused after certain amount of time called echo time (TE). More detailed descriptions can be found in [15,16].

2.2 CARDIAC IMAGING

MRI is widely used to diagnose cardiac diseases. Different sequences have been developed to evaluate the anatomic structure, heart function, myocardial infarction, etc.

2.2.1 CARDIAC CINE IMAGING

Cardiac cine images can show the dynamic motion of the heart. In cine images, a cardiac cycle is divided into multiple cardiac phases, usually 20-30 phases. For each cardiac phase, 8-10 short axis images are taken to cover the whole left ventricle of the heart, Figure 7 (Left). Typically, a balanced SSFP sequence is used to acquire cine images due to its short TR and TE, which allows fast data collection. In addition, it can provide excellent contrast between blood and myocardium. In clinical practice, k-space signal is acquired continuously during the heart cycle, a breath hold is used to prevent respiratory motion artifacts and retrospective ECG gating is used to bin data into different cardiac phases, Figure 7 (Right). A multi-slice cine image stack usually takes 5-10 min (1 or 2 slices are acquired during successive breath hold periods of 10-15 s each).

Alternately, a continuous, free-breathing acquisition can be used to avoid the idle time periods between breath holds. However respiratory motion needs to be compensated for during the reconstruction process. The cine-GRICS method proposed in [17] allows an image stack to be acquired in 3-5 min.

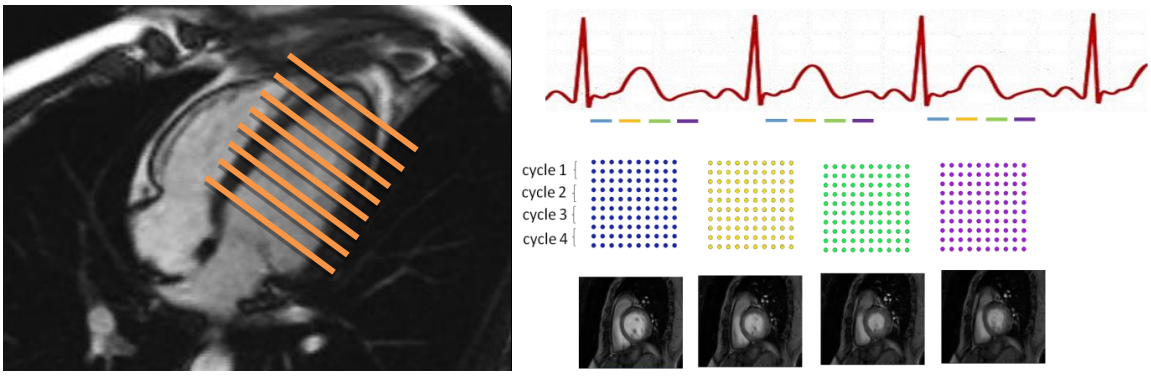

Figure 7. Cardiac cine image. (Left) Location of 2Dcine stack (Right) Illustration of continuous image acquistion and cine image reconstruction by binning data.

Cardiac cine imaging by MRI is the gold standard to assess the ejection function of heart. There are dark-blood image and bright-blood image. The black-blood sequence uses inversion recovery sequence, and the bright-blood image uses SSFP sequence.

Although multi-slice 2D cine imaging is widely used, 3D cine imaging gains more and more interest. A 3D version of the bSSFP sequence does exist but has less good contrast than the 2D sequence due to a reduced “in-flow” effect (fresh spins moving out of the imaging slice). Another difficulty is that respiratory motion needs to be corrected efficiently. A solution has been proposed combining multiple near-orthogonal 2D stacks into a 3D isotropic volume, using cine-GRICS motion correction and a super-resolution reconstruction [17]. Compared to multi-slice 2D images, this 3D cine imaging provides isotropic measurements, which allows more accurate estimation of the heart volume.

2.2.2 LATE GADOLINIUM ENHANCEMENT IMAGING

Late Gadolinium enhancement image (LGE), which is also called myocardial delayed enhancement images (MDE), is used to assess the viability of the myocardium. In LGE, contrast agent is injected into the patient (0.1 - 0.2 mmol/kg). Gadolinium compounds are the most often used contrast agent. Due to the delayed washout process, an excess of contrast agent accumulates in the pathological tissues, therefore the myocardium affected by fibrosis (e.g. following a myocardial infarction) shows higher intensity than normal myocardium after 10-15min. The inversion time of the sequence can be adjusted to null the signal from the normal myocardial tissue.

The LGE image shows different patterns with different diseases [18]. The myocardium can be divided as subendocardial, subepicardial and mesocardial (or midmyocardium) region. For ischemic myocardial disease, the delayed enhancement image shows higher intensity in subendocardial or transmural regions, limited to the area of the vascular obstruction. For non-ischemic myocardial diseases, the delayed enhancement distribute in more diffuse areas. When more than 50% of the myocardium thickness shows enhanced intensity, the infarct is regarded as transmural. Delayed enhancement in transmural myocardium is an indicator for atherosclerosis or myocarditis. The subepicardial enhancement is related with myocarditis and mesocardial enhancement suggests hypertrophic cardiomyopathy or dilated cardiomyopathy.

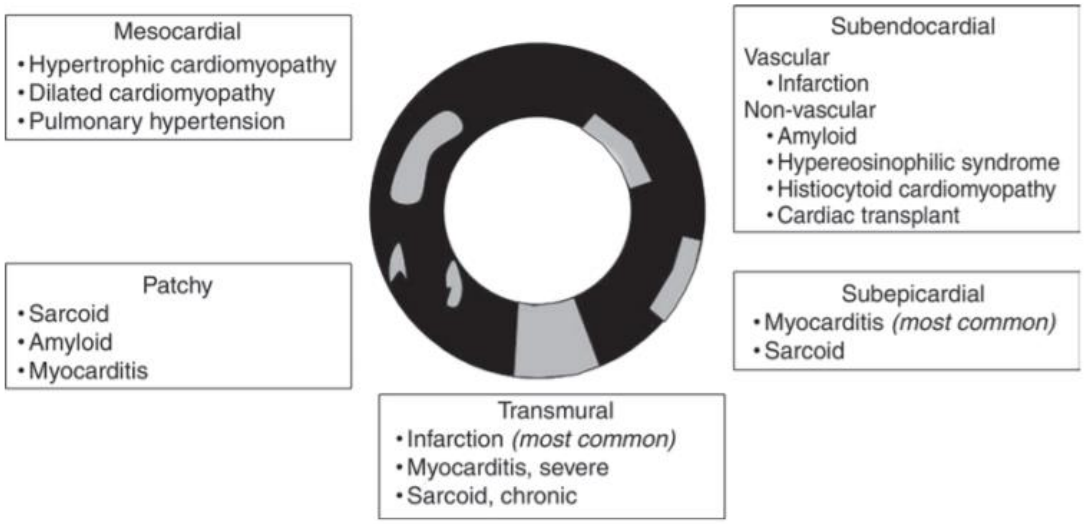

Figure 8. Cardiac delayed enhancement imaging for cardiac disease diagnosis [18].

2.2.3 T_1 & T_2 (T_2*) MAPPING

T_1 mapping and T_2 mapping are parametric mappings of the relaxation process of myocardial tissue. In parametric mapping, the physical value (T_1 or T_2) of pixels are rendered as an image. Compared to conventional MR images, parametric mapping can provide quantitative measurements of myocardial tissue.

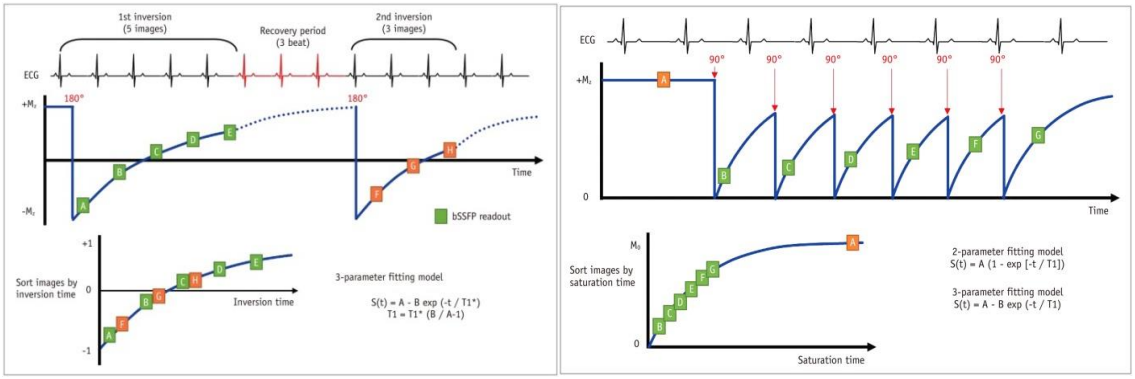

Figure 9. Illustration of MOLLI sequence (Left) and Saturation recovery sequence (Right) [19].

T_1 mapping shows the longitudinal relaxation time of each pixels. LGE is the most widely used technique to evaluate ischemic myocardial diseases, however, it is unable to detect diffuse fibrosis because its contrast is an unknown function of the tissue properties. The T_1 value of the myocardial tissue is dependent on the composition of the tissue. For example, higher water content or larger interstitial space result in larger T_1 value, and

overload of fat or iron lead to smaller T_1 value [20]. Therefore, T_1 mapping can provide diagnostic information for diffuse fibrosis.

To get T_1 mapping, a variety of sequences has been proposed. Those sequences can generally be divided into two categories: inversion recovery methods and saturation recovery methods. In inversion recovery sequences, the magnetization is inverted by 180 degrees and in saturation recovery sequences, the magnetization is flipped by 90 degrees. The most popular inversion recovery method is MOLLI, which acquires 8 images within one breath-hold, as shown in Figure 9 (Left). Usually a 5(3)3 scheme is used, which means that images are acquired in each the first 5 heart beats, then there is a rest period of 3 heart beats and finally images are acquired during the last 3 heart beats. In saturation recovery sequences, the longitudinal magnetization is saturated to zero, so there is no need for a rest period to ensure full recovery as in MOLLI, since the next recovery cycle always starts from the saturation state, Figure 9 (Right). In this sequence, usually one image is acquired in one recovery cycle.

It needs to be mentioned that the estimated T_1 value depends on the acquisition scheme and sequence used. T_1 value from the different acquisition methods are not comparable. Table 1 summarized the T_1 values reported from different researches.

Table 1. Comparison of T_1 value in myocardium and blood pool with different sequence and number of parameters

	Setup	Native-myo (ms)	post-myo (ms)	Native-blood (ms)	post-blood (ms)
(Messroghli, 2004)[21]	MOLLI,1.5T(volunteer1)	1076±72	492±39	1551±55	313±10
	MOLLI,1.5T(volunteer2)	969±84	450±40	1544±69	325±14
(Dabir, 2014)[22]	MOLLI,3T	1025±23	-	-	-
(Sibley, 2011)[23]	MOLLI,3T	1347±37	-	2076±125	-
(Knobelsdorff-Brenkenhoff,2013)[24]	MOLLI	1157-1180	399-423	-	-
(Lee, 2011)[25]	MOLLI,3T	1315±39	-	2020±129	-
(Stainsby, 2013)[26]	MOLLI,1.5T	792(T1*)/1018(T1)	-	-	-
	SMART,1.5T	1193	-	-	-
(Ellims, 2014)[27]	IR,1.5T	937±158	380±82	1435±335	229±34
(Bhuva, 2015)[28]	MOLLI,T1star	-	-	1636±87	-
	MOLLI,T1	-	-	1613±71	-

T_1 mapping can be measured with or without contrast agent. The T_1 mapping without contrast agent is named as 'Native' or 'Pre-contrast' T_1 mapping and the T_1 mapping with contrast agent is called 'Post-contrast' T_1 mapping. Contrast agent is used to enhance the difference between the normal and fibrosis tissue. The shortening of the T_1 value is proportional to the concentration of contrast agent. This principle can be used to create

an extracellular volume map (ECV), which is a biomarker for myocardial tissue remodeling [20].

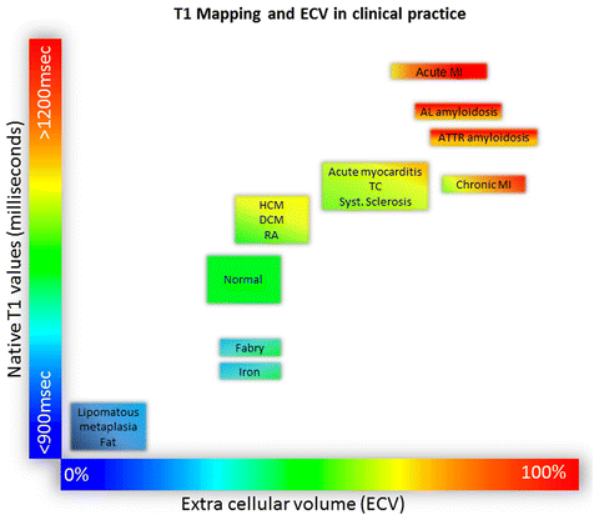

Figure 10. T1 mapping and ECV for cardiac disease diagnosis[20].

The ECV map is generated by combining the information in native and post contrast T_1 maps.

$$\mathrm{ECV} = (1 - \mathrm{haematocrit}) \frac{\frac{1}{T_{1,\mathrm{myo,post-contrast}}} - \frac{1}{T_{1,\mathrm{myo,native}}}}{\frac{1}{T_{1,\mathrm{blood,post-contrast}}} - \frac{1}{T_{1,\mathrm{blood,native}}}}$$

T_2 mapping provides the transverse relaxation maps. The T_2 value of the myocardial tissue is mainly affected by the water content, which is related to myocardial edema as in acute myocardial infarction. Similar as T_1 mapping, several images are acquired and curve fitting is performed to estimate the T_2 value.

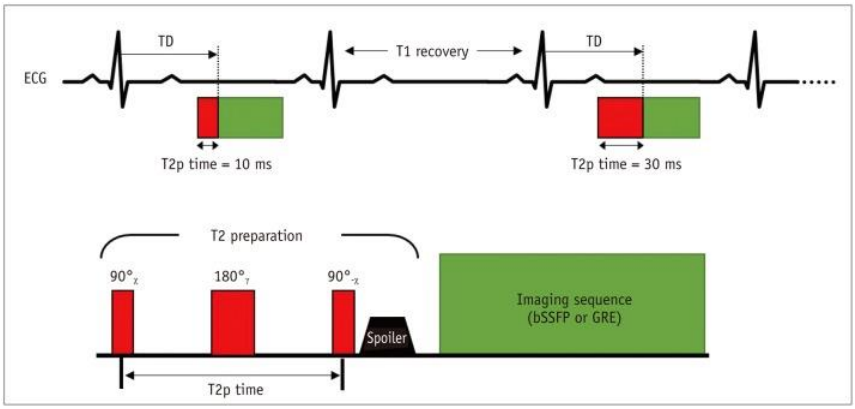

Figure 11. Illustration of T_2 mapping sequence [19]

Figure 11 shows the acquisition sequence for T_2 mapping. The acquisition sequence usually contains a preparation module and a fast imaging acquisition module. More detailed description can be found in [19].

2.2.4 FLOW IMAGING

Flow or motion information can be obtained from the phase information of the MR signal. The velocity of the moving particle can be encoded using a velocity encoding gradient. Suppose B_0 is the static magnetic field, ΔB_0 is the local field inhomogeneity and $G(t)$ is the magnetic field gradient, then the lamor frequency of the moving particle located at r is:

$$\omega_L(\vec{r},t) = \gamma \cdot (B_0 + \Delta B_0 + r(t)G(t))$$

If we change to the rotating coordinate [29], the relative frequency become:

$$\omega(\vec{r},t) = \gamma \cdot (\Delta B_0 + r(t)G(t))$$

Then the phase change of the particle at location r is

$$\varphi(r,TE) - \varphi(r,t_0) = \int_{t_0}^{TE} \omega(r,t)dt = \gamma \Delta B_0(TE - t_0) + \gamma \int_{t_0}^{TE} G(t)r(t)dt$$

the gradient related phase change can be expanded:

$$\varphi(r,TE) = \varphi_0 + \sum_{n=0}^{\infty} \gamma \frac{r^{(n)}}{n!} \int_{t_0}^{TE} G(t)(t - t_0)^n dt$$

where $r^{(n)}$ is the n-th derivative of r. if we keep only the 0-th and 1-th order, then

$$\varphi(r,TE) = \varphi_0 + \gamma r_0 \int_0^{TE} G(t)dt + \gamma v \int_0^{TE} G(t)tdt + \cdots$$

Here $\gamma r_0 \int_0^{TE} G(t)dt$ measures the phase change of the static spins (denoted as M_0) and $\gamma v \int_0^{TE} G(t)tdt$ measures the phase change of moving spins (denoted as M_1).

Velocity encoding is realized by bipolar gradients. However, the phase difference induced by the inhomogeneity of the magnetic field cannot be compensated, therefore a pair of bipolar gradient of reversed order is used [30]. By subtracting the phase of the two bipolar

gradients, the velocity can be measured. It needs to be mentioned that the measured velocity is the projection of the true velocity in the direction of the applied velocity-encoding gradient.

$$\varphi_1 - \varphi_2 = \Delta\varphi = \gamma \cdot v \cdot \Delta M_1$$

So that

$$v = \frac{\Delta\varphi}{\gamma \Delta M_1}$$

Traditional 2D phase contrast image can be used to measure the flow in the arteries or veins. One important use is to estimate the instantaneous flow rate and ejection volume curve. Another application use is to calculate the ratio between pulmonary flow (Qp) and system flow (Qs). This ratio is called Qp:Qs measurement, and it is used to measure the cardiac shunt.

Nowadays, 4D flow imaging is getting more and more attention. Fast imaging techniques allow the acquisition of 3D velocity information in the 3D volume at once, using multiple images to cover the whole heart cycle in less than 10min. Compared to 2D flow imaging, 4D flow imaging allows more accurate measurement of the flow by adjusting the measurement plane according to the flow direction and heart movement[31]. Another topic under research is the intra-cardiac flow pattern, which can provide new parameters for cardiac disease diagnostic[32].

2.2.5 DIFFUSION WEIGHTED IMAGING AND DIFFUSION TENSOR IMAGING

Diffusion imaging is based on the Brownian motion of the molecules. For molecules inside cells, the Brownian motion is constrained by the boundary of the cells.

Diffusion imaging uses a pulsed gradient spin-echo sequence to encode the diffusion motion, which is composed by a 90 degree pulse followed by 180 degree pulse, with diffusion-encoding gradients on both sides of the 180° pulse [33].

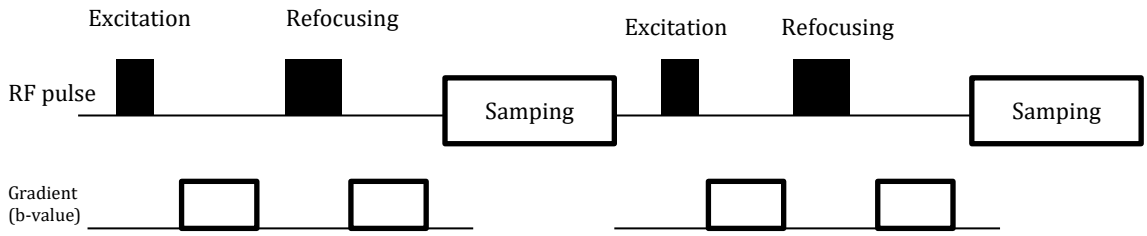

Figure 12. Sequence for diffusion tensor image.

If molecules are static, the phase accumulated during the first diffusion gradient would be fully compensated by the phase accumulated during the second one (same phase with reversed polarity). Due to the Brownian motion, the spatial position of the water molecules will be different during the first and second diffusion gradient, resulting in a phase shift and an attenuation of the average signal of the voxel. The attenuation of the signal can be described as

$$SI = SI_0 \times exp(-b \times D),$$

Here SI is the attenuated signal, SI_0 is the original signal. b is a parameter determined by the amplitude, duration and the spacing of the diffusion encoding pulse. D is the diffusion coefficient. In clinical practice, the measured diffusion coefficient can be obtained by measuring signals under different b value, which is named as ADC (Appearance diffusion coefficient).

In diffusion tensor imaging, the diffusion gradient is defined. By varying the direction of the diffusion gradient, a sampling space is formed, named as q-space. If 3-diffusion tensor images along 3 orthogonal axis are acquired, a model of the 3d diffusion movement can be established. However, the fiber orientation can be more complicated, and [34] proposed to use ellipsoid to model the local orientation of the fibers. Therefore, 6 diffusion weighted images are sampled in the q-space. In this case, the diffusion coefficient is a matrix and can be decomposed along 3 principal axes.

$$D = \begin{bmatrix} D_{00} & D_{01} & D_{02} \\ D_{10} & D_{11} & D_{12} \\ D_{20} & D_{21} & D_{22} \end{bmatrix} = E \begin{bmatrix} \lambda_0 & 0 & 0 \\ 0 & \lambda_1 & 0 \\ 0 & 0 & \lambda_2 \end{bmatrix} E^T$$

Diffusion tensor imaging is quite useful to establish the fiber orientation model of the heart. However this is particularly challenging for the heart due to the moving nature of

the heart. A variety of fast acquisition and post-processing techniques have been developed to improve the quality of cardiac diffusion imaging [35].

2.2.6 IMAGING PLANES

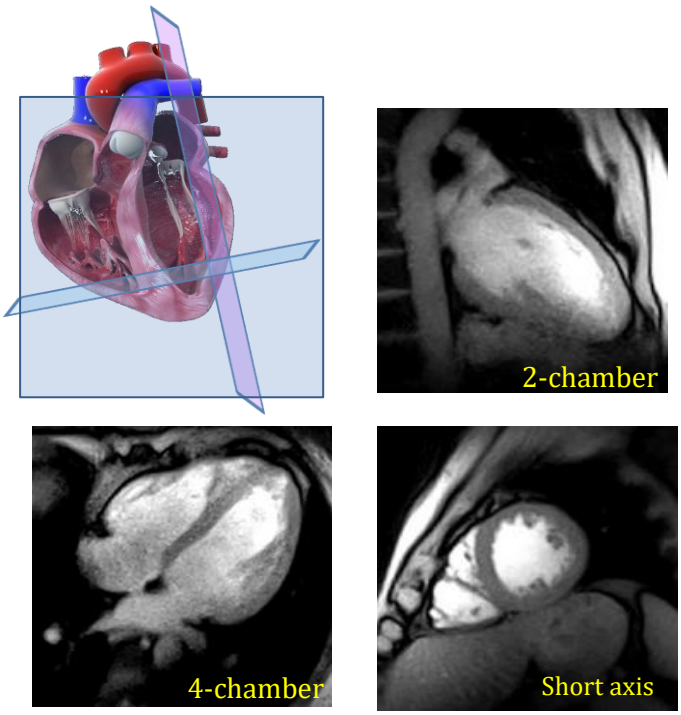

Figure 13. Illustration of cardiac imaging planes

For the heart, the most often used views include short axis images, 4-chamber view, 2-chamber view and 3-chamber view, as shown in Figure 13. The local long axis is defined as the line from mitral valve to the apex of the heart. The plane perpendicular to the long axis is defined as short-axis plane. More detailed description about how to find the imaging planes can be found in [36].

2.2.7 AHA 17 SEGMENT MODEL AND BULL'S EYES

In clinical applications, heart function is evaluated globally and locally. Global parameters including end-diastolic volume, end-systolic volume, ejection volume, ejection fraction and so on. Local parameter are usually evaluated by segmenting the heart into several regions and the results are summarized and visualized using a Bull's eyes plot. The AHA 16-segment model is a standard way to segment the left ventricle. The definition of the AHA16-segment model is shown in Figure 14. In AHA-16 segment model, short axis slices

at apex, mid-cavity and basal are taken. On each slice, the myocardium region is divided into 6 (basal and mid-cavity) or 4 (apex) region. The regions are grouped into different area, as color coded in Figure 14 (Left). In clinical report, bull's eye is usually used to visualize the regional result Figure 14 (Right).

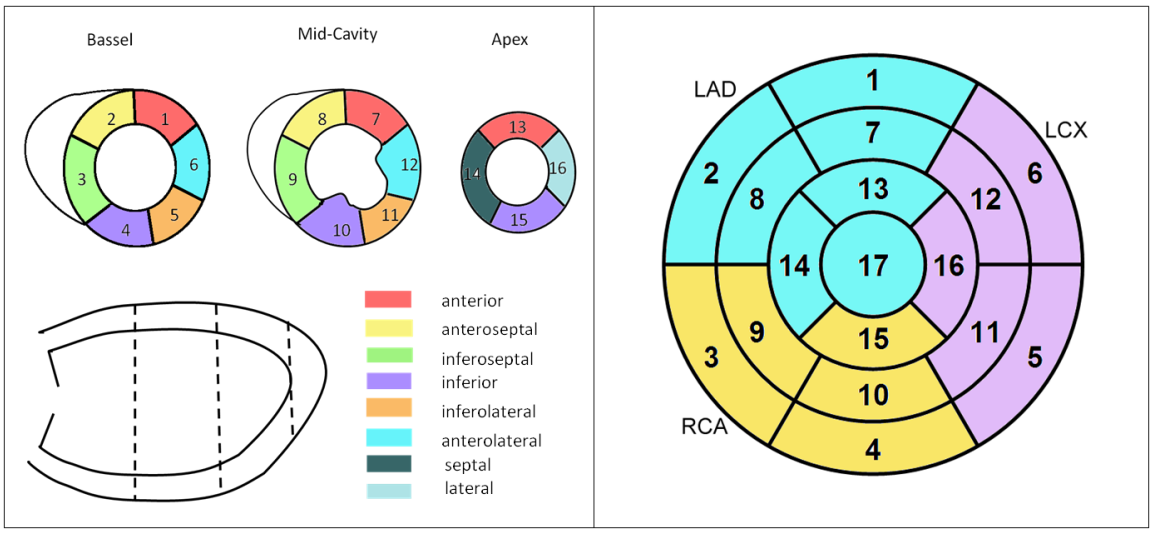

Figure 14. AHA-16 segment definition

Chapter 3 Image registration

Image registration is a widely used technique in medical image analysis. It tries to match the coordinates of different images so that the images are aligned with each other. In this chapter, the basic components and workflow of image registration are introduced. Several image registration frameworks are explained in more detail.

3.1 Introduction

For medical application, image registration can be applied in several ways. The most important use is to align the images acquired at different times or by different imaging techniques so that the information from different images can be fused [37]. Another important use is to measure the deformation between the two images. The measured deformation can either be used as motion field to extract clinical information like myocardial contraction, or it can also be used as intermediate information to improve the image quality of a moving organ like the heart [10,38].

In image registration cost function is defined to measure how well the two images aligned. The cost function can be defined based on geometric features or/and image intensity. For feature based image registration, anatomical landmarks are extracted and the correspondence is established. Then the motion field in the rest of the image is obtained by interpolation. For intensity based image registration, a transformation model is defined based on the application purpose and the intensity of the images is used to measure the similarity between the images. The following paragraph explains the intensity based image registration.

3.2 Intensity based image registration

Intensity based image registration can be formulated as an optimization problem, which can be defined as

$$Argmax_T C(I_F(x,y), I_M(T(x,y)))$$

Where $C(I_F, I_M)$ is the similarity function to estimate the similarity between fixed image I_F and moving image I_M. And $(x', y') = T(x, y)$ is the spatial transformation. To solve this optimization problem, iterative methods are usually used. The moving image is distorted step by step to match the fixed image, therefore in addition to the optimizer and similarity module, an interpolator is needed to create a new deformed image from a moving image I_M. The diagram can be summarized as below.

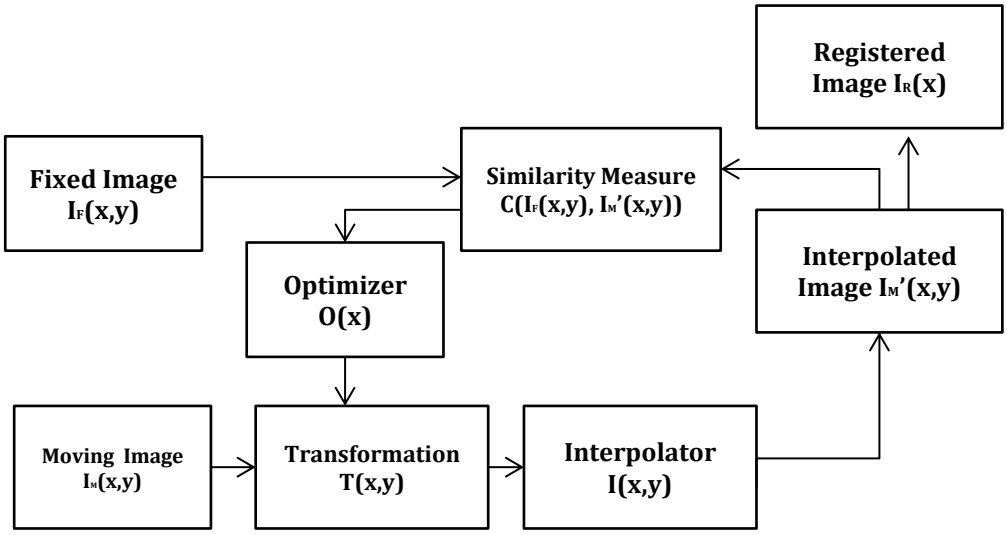

Figure 15. Image registration framework

In practice, a multi-level approach is used to reduce the number of parameters and improve the accuracy of registration in case of large deformation. In multi-level framework, a pyramid of images is created, the images are registered from coarse to fine. The deformation grid got from the coarse level is used as an initial guess for the finer level.

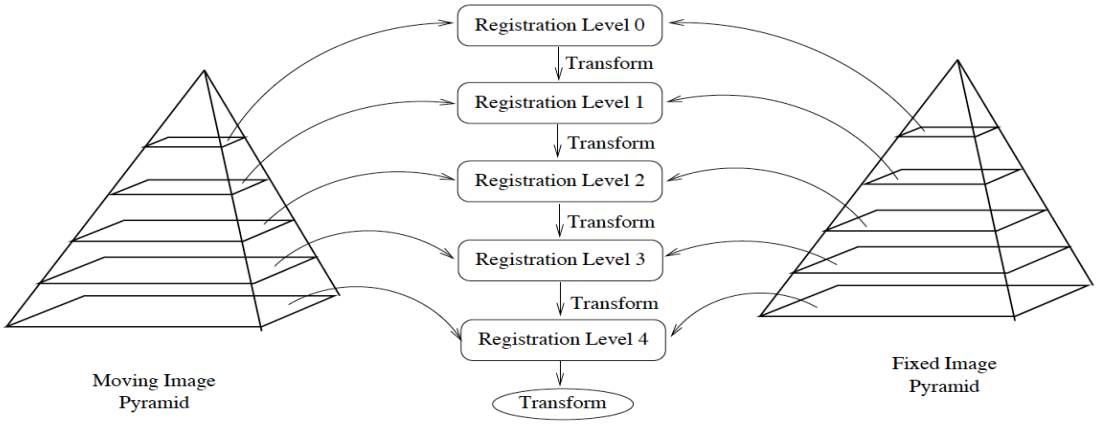

Figure 16. Illustration of multi-level image registration framework.

3.3 TRANSFORMATION

3.3.1 RIGID TRANSFORMATION

The rigid transformation is a global transformation for the whole image. Depending on the number of degrees of freedom, there are different transformations models:

- *TRANSLATION*

$$\begin{bmatrix} x' \\ y' \end{bmatrix} = \begin{bmatrix} x \\ y \end{bmatrix} + \begin{bmatrix} t_x \\ t_y \end{bmatrix}$$

- *ROTATION*

$$\begin{bmatrix} x' \\ y' \end{bmatrix} = \begin{bmatrix} cos\,(\theta) & sin\,(\theta) \\ -sin\,(\theta) & cos\,(\theta) \end{bmatrix} \begin{bmatrix} x \\ y \end{bmatrix}$$

- *RIGID TRANSFORMATION*

$$\begin{bmatrix} x' \\ y' \end{bmatrix} = s \begin{bmatrix} cos\,(\theta) & sin\,(\theta) \\ -sin\,(\theta) & cos\,(\theta) \end{bmatrix} \begin{bmatrix} x \\ y \end{bmatrix} + \begin{bmatrix} t_x \\ t_y \end{bmatrix}$$

- *AFFINE TRANSFORMATION*

$$\begin{bmatrix} x' \\ y' \end{bmatrix} = \begin{bmatrix} a_{00} & a_{01} \\ a_{10} & a_{11} \end{bmatrix} \begin{bmatrix} x \\ y \end{bmatrix} + \begin{bmatrix} b_0 \\ b_1 \end{bmatrix} = A \begin{bmatrix} x \\ y \end{bmatrix} + b$$

3.3.2 NON-RIGID REGISTRATION

3.3.2.1 POLYNOMIAL TRANSFORMATION.

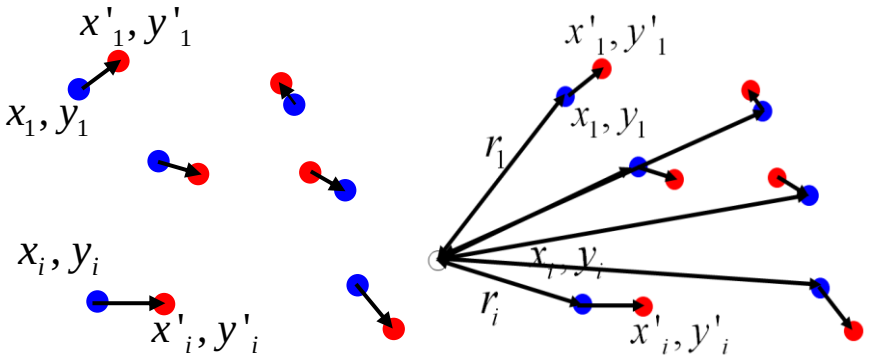

Figure 17. (Left) polynomial transformation (Right) Thin-plate transformation

For polynomial transformation, a set of feature points are detected, the transformation is modeled as a polynomial function of the position of the points (Figure 17). The transformation parameters are estimated from a feature set and applied to the whole image.

$$\begin{cases} x' = a_{0,0} + a_{1,0}x + a_{0,1}y + a_{1,1}xy + a_{2,0}x^2 + a_{0,2}y^2 + \cdots \\ y' = b_{0,0} + b_{1,0}x + b_{0,1}y + b_{1,1}xy + b_{2,0}x^2 + b_{0,2}y^2 + \cdots \end{cases}$$

3.3.2.2 THIN-PLATE

The thin-plate transformation model assumes a smooth transformation surface. Similarly to the polynomial transformation, a set of feature points is needed and the transformation parameters are estimated using those points. For the other points, the transformation is like a global polynomial transformation plus the weighted local shift depending on the distance of this point to the feature point.

$$x' = a_0 + a_1 x + a_2 y + \sum_{1}^{N} F_i r_i^2 \log(r_i)$$

$$y' = b_0 + b_1 x + b_2 y + \sum_{1}^{N} G_i r_i^2 \log(r_i)$$

Where $r_i^2 = (x - x_i)^2 + (y - y_i)^2$

This is equivalent to minimizing the bending energy of the transformation[39]

$$E_{bending} = \iint \left(\left(\frac{\partial^2 T}{\partial x_1^2}\right)^2 + 2\left(\frac{\partial^2 T}{\partial x_1 \partial x_2}\right)^2 + \left(\frac{\partial^2 T}{\partial x_2^2}\right)^2 \right) dx_1 dx_2$$

Where $T(x, y) = a_1 + a_x x + a_y y + \sum_{i=1}^{n} F_i r_i^2 log r$

For example, given N=5 points, the parameters can be estimated by solving the following equation. This equation can be solved efficiently using LU decomposition method.

$$\begin{bmatrix} x'_1 \\ x'_2 \\ x'_3 \\ x'_4 \\ x'_5 \\ 0 \\ 0 \\ 0 \end{bmatrix} = \begin{bmatrix} 1 & x_1 & y_1 & r_{1,1}^2 \ln r_{1,1}^2 & r_{1,2}^2 \ln r_{1,2}^2 & r_{1,3}^2 \ln r_{1,3}^2 & r_{1,4}^2 \ln r_{1,4}^2 & r_{1,5}^2 \ln r_{1,5}^2 \\ 1 & x_2 & y_2 & r_{2,1}^2 \ln r_{2,1}^2 & r_{2,2}^2 \ln r_{2,2}^2 & r_{2,3}^2 \ln r_{2,3}^2 & r_{2,4}^2 \ln r_{2,4}^2 & r_{2,5}^2 \ln r_{2,5}^2 \\ 1 & x_3 & y_3 & r_{3,1}^2 \ln r_{3,1}^2 & r_{3,2}^2 \ln r_{3,2}^2 & r_{3,3}^2 \ln r_{3,3}^2 & r_{3,4}^2 \ln r_{3,4}^2 & r_{3,5}^2 \ln r_{3,5}^2 \\ 1 & x_4 & y_4 & r_{4,1}^2 \ln r_{4,1}^2 & r_{4,2}^2 \ln r_{4,2}^2 & r_{4,3}^2 \ln r_{4,3}^2 & r_{4,4}^2 \ln r_{4,4}^2 & r_{4,5}^2 \ln r_{4,5}^2 \\ 1 & x_5 & y_5 & r_{5,1}^2 \ln r_{5,1}^2 & r_{5,2}^2 \ln r_{5,2}^2 & r_{5,3}^2 \ln r_{5,3}^2 & r_{5,4}^2 \ln r_{5,4}^2 & r_{5,5}^2 \ln r_{5,5}^2 \\ 0 & 0 & 0 & 1 & 1 & 1 & 1 & 1 \\ 0 & 0 & 0 & x_1 & x_2 & x_3 & x_4 & x_5 \\ 0 & 0 & 0 & y_1 & y_2 & y_3 & y_4 & y_5 \end{bmatrix} \begin{bmatrix} a_0 \\ a_1 \\ a_2 \\ F_1 \\ F_2 \\ F_3 \\ F_4 \\ F_5 \end{bmatrix}$$

The thin-plate transformation can guarantee to have a smooth surface, implemented by adding a regularization in the cost function. The regularization term is the second order gradient of the deformation field.

3.3.2.3 CUBIC B-SPLINE

In cubic B-spline transformation, a regular grid is defined and the interception points are defined as control points. Perturbation of a control point can affect and only affect the neighboring point. For points other than control points, the local translation is obtained by cubic b-spline interpolation of the shifted control points. For 2D images, the transform can be formulated as

$$\begin{bmatrix} x' \\ y' \end{bmatrix} = T(x,y) = \begin{bmatrix} \sum_{l=0}^{3}\sum_{m=0}^{3} B_3^l(u)B_3^m(v)\varphi_{x,i+l,j+m} \\ \sum_{l=0}^{3}\sum_{m=0}^{3} B_3^l(u)B_3^m(v)\varphi_{y,i+l,j+m} \end{bmatrix}$$

Where ($\varphi_{x,i,j}$, $\varphi_{y,i,j}$) is the deformation at control point (i,j) and $\{\mathrm{B_i}\}$ are the spline functions

$$\mathrm{B}_3^0(\mathrm{u}) = (1-\mathrm{u}^3)/6$$

$$\mathrm{B}_3^1(\mathrm{u}) = (3\mathrm{u}^3 - 6\mathrm{u}^2 + 4)/6$$

$$\mathrm{B}_3^2(\mathrm{u}) = (-3\mathrm{u}^3 + 3\mathrm{u}^2 + 3\mathrm{u} + 1)/6$$

$$\mathrm{B}_3^3(\mathrm{u}) = \mathrm{u}^3/6$$

Similar to the 2D case, the 3D cubic B-spline transformation can be defined as

$$\begin{bmatrix} x' \\ y' \\ z' \end{bmatrix} = T(x) = \begin{bmatrix} \sum_{l=0}^{3}\sum_{m=0}^{3}\sum_{n=0}^{3} B_3^l(u)B_3^m(v)B_3^n(w)\varphi_{x,i+l,j+m,k+n} \\ \sum_{l=0}^{3}\sum_{m=0}^{3}\sum_{n=0}^{3} B_3^l(u)B_3^m(v)B_3^n(w)\varphi_{y,i+l,j+m,k+n} \\ \sum_{l=0}^{3}\sum_{m=0}^{3}\sum_{n=0}^{3} B_3^l(u)B_3^m(v)B_3^n(w)\varphi_{z,i+l,j+m,k+n} \end{bmatrix}$$

3.4 SIMILARITY MEASUREMENT

The most often used cost function for intra modality registration are sum of square difference (SSD, also named as Least square difference) and normalized cross correlation (NCC)

$$SSD(T) = \sum_i (I_{F,i} - I_{M,i}(T))^2$$

$$NCC(T) = \frac{\sum_i (I_{F,i} - \mu_F)(I_{M,i}(T) - \mu_M)}{\sqrt{\sum_i (I_{F,i} - \mu_F)^2}\sqrt{\sum_i (I_{M,i}(T) - \mu_M)^2}}$$

Where i is the index of pixels, μ_F, μ_M are the average intensity of the fixed image and moving image, T is the transforamtion.

Mutual information (*MI*) or normalized mutual information (*NMI*) are more widely used for images with different contrasts, e.g. different modalities. In information theory, the *MI* is defined as:

$$MI = H(I_F) + H(I_M) - H(I_F, I_M)$$

where $H(I_F) = -\sum_{i_{F,}} p(I_F = i_{F,}) \cdot log(p(I_F = i_{F,}))$ is the entropy of the fixed image I_F and $H(I_F, I_M)$ is the joint entropy of fixed image and moving image.

For image registration, MI can be rewritten as:

$$MI(u) = \sum_{i_{F,} i_M} P_{I_{F,} I_M}(I_F = i_F, I_M(u) = i_M) \cdot log \frac{P_{I_{F,} I_M}(I_F = i_F, I_M(u) = i_M)}{P_F(I_F = i_F) \cdot P_M(I_M(u) = i_M)}$$

Here $i_{F,} i_M$represent the intensity in the fixed image and moving image respectively.

During the image registration process, a challenge is to calculate the derivative of the similarity measurement with respect to the deformation parameters. For SSD

$$\frac{\partial SSD(T)}{\partial T} = \sum_{i_{F,} i_M} 2 \cdot (I_{F,i} - I_{M,i}(T)) \cdot \frac{\partial I_{M,i}}{\partial T}$$

For mutual information, the derivative is more difficult to calculate. In order to simplify the annotation, suppose $P_{I_{F,} I_M}(I_F = i_F, I_M(u) = i_M) = P_{F,M}$, then

$$\begin{aligned}
\frac{\partial MI(T)}{\partial T} &= \sum_{i_{F,} i_M} \left[\left(P_{F,M}\right)' log \frac{P_{F,M}}{P_F P_M} + P_{F,M} \frac{P_F P_M}{P_{F,M}} \frac{\partial}{\partial u} \left(\frac{P_{F,M}}{P_F P_M} \right) \right] \\
&= \sum_{i_{F,} i_M} \left[\left(P_{F,M}\right)' log \frac{P_{F,M}}{P_F P_M} + P_F P_M \left(-(P_F P_M)^2 \frac{\partial P_F P_M}{\partial u} P_{F,M} + \frac{(P_{F,M})'}{P_F P_M} \right) \right] \\
&= \sum_{i_{F,} i_M} \left[\left(P_{F,M}\right)' log \frac{P_{F,M}}{P_F P_M} - \frac{(P_M)' P_{F,M}}{P_M} + (P_{F,M})' \right] \\
&= \sum_{i_{F,} i_M} \left(P_{F,M}\right)' \left[log \frac{P_{F,M}}{P_F P_M} + 1 \right] - \sum_{i_{F,} i_M} \frac{(P_M)' P_{F,M}}{P_M}
\end{aligned}$$

The last term $\sum_{i_{F,} i_M} \frac{(P_M)' P_{F,M}}{P_M} = \sum_{i_M} \frac{(P_M)'}{P_M} \sum_{i_{F,}} P_{F,M} = \sum_{i_M} (P_M)' = 0$ because the entropy of the image does not depend on the transformation.

Similarly, the first term $\sum_{i_F,i_M}(P_{F,M})' \left[log \frac{P_{F,M}}{P_F P_M} + 1\right] = \sum_{i_F,i_M}(P_{F,M})' log \frac{P_{F,M}}{P_M}$

So

$$\frac{\partial MI(T)}{\partial T} = \sum_{i_F,i_M} (P_{F,M})' log \frac{P_{F,M}}{P_M}$$

More details about how to get the gradient of the probability distribution function can be found in [40].

3.5 OPTIMIZATION

3.5.1 STEEPEST DESCENT

Steepest descent optimization, also named as gradient descent optimization, is a first-order iterative optimization algorithm. Starting from the initial position, the steepest descent algorithm takes steps in the negative gradient direction to find the minimum.

Suppose u_n is the displacement field at iteration n. The relationship between transformation T and displacement u is

$$T = I + u$$

In steepest decent algorithm,

$$u_{n+1} = u_n - \gamma \nabla E(u; I_F, I_M)$$

Here E is the cost function (including the similarity function and the regularization in image registration), γ is the step size. Usually γ is also updated in each iteration.

$$\gamma_n = \frac{(u_n - u_{n-1})^T [\nabla E(u_n) - \nabla E(u_{n-1})]}{\|\nabla E(u_n) - \nabla E(u_{n-1})\|^2}$$

if E is convex, the gradient descent algorithm is guaranteed to converge.

3.5.2 STOCHASTIC GRADIENT DESCENT

In stochastic gradient method, the true gradient is replaced by an approximated gradient obtained from a randomly selected subset of samples, which can reduce the calculation time.

$$u_{k+1} = u_k - \gamma\widetilde{\nabla E}$$

Where $\widetilde{\nabla \mathrm{E}}$ is an approximation of the $\nabla \mathrm{E}$ and the step size γ is adjusted

$$\gamma_k = a/(k+A)^{\alpha}$$

Parameters $\mathrm{a} > 0$, $\mathrm{A} \geq 1$ and $0 < \alpha \leq 1$. Theoretically $\alpha = 1$ gives optimum rate of convergence [41], however, in practices $\alpha < 1$ is often used to prevent the step size decay from being too fast. The choice of the parameters should be scaled as the cost function changes. In [42], an adaptive stochastic gradient descent algorithm is proposed to adjust γ_{k} based on $\widetilde{\nabla \mathrm{E}_{\mathrm{k}}}^{\mathrm{T}} \widetilde{\nabla \mathrm{E}}_{\mathrm{k-1}}$. The idea is that when two consecutive steps are in similar direction, then larger step sizes should be taken. It can be formulated as the following:

$$\gamma_k \equiv \gamma(t_k) = a/(t_k + A)^{\alpha}$$

$$t_{k+1} = max\,(0, t_k + f(-\widetilde{\nabla E_k}^{T} \nabla \tilde{E}_{k-1}))$$

Where f is the sigmoid function and $\alpha = 1$ is used. More details about the selection of a and A are given in [42].

3.5.3 CONJUGATE DESCENT

Conjugate gradient algorithm
$r_0 = b - Ax_0$
$p_0 = r_0$
K=0
Repeat
$\alpha_k = \frac{r_k^T r_k}{p_k^T A p_k}$
$x_{k+1} = x_k + \alpha_k p_k$
$r_{k+1} = r_k - \alpha_k A p_k$
If $\mathrm{r}_{\mathrm{k+1}}$ is sufficiently small, the exit loop
$\beta_{k+1} = \frac{r_{k+1}^T r_{k+1}}{r_k^T r_k}$
$p_{k+1} = r_{k+1} + \beta_k p_k$
k=k+1
End repeat

The conjugate gradient algorithm is used for solving linear systems. It is regarded as a method between steepest decent and Newton's method, therefore reaching a good compromise between speed and complexity. In the conjugate gradient algorithm, the

conjugate direction is used instead of the gradient direction. The pseudo code is shown as above.

3.5.4 POWELL'S METHOD

Powell's method is a conjugate direction method. This algorithm starts from a set of initial mutually conjugate directions $\{s_i\}$. It tries to minimize the cost function on each direction by searching along the searching direction.

Powell's method
$x_0 \in R^N$: initial position $\{s_i\}$: initial searching direction Repeat: Search along each direction in $\{s_i\}$ to get minimum $\{\alpha_i\}$ and set $x_i = x_{i-1} + \alpha_i s_i$ Adjust searching direction, for i=1,…,N-1, set $s_i = s_{i+1}$ $s_N = x_N - x_0$ Move x_N to the minimum along the direction s_N and set this point to x_0 End repeat

For quadratic cost function $E(x) = c - b \cdot x + \frac{1}{2} x \cdot A \cdot x^T$, where $x_0 \in R^N$, Powell's algorithm can reach a minimum with N iteration. Powell's method does not need to calculate the gradient of the cost function, however, this method may fail when the new search direction is not independent from the previous one. An improved method has be proposed by [43].

3.5.5 QUASI-NEWTON METHOD

Quasi-Newton method
x_0 : initial guess H_0 : nxn matrix Repeat Compute $\nabla f(x_k)$ and take the search direction as $h_k = -H_k \nabla f(x_k)$ Search along h_k direction and take $x_{k+1} = x_k + \alpha h_k$ where $f(x_k + \alpha h_k)$ is mimium $H_{k+1} = H_k + U_k$ where U_k is the updating matrix End repeat

Newton method is a second order optimization. Compared to first order methods, newton method converges much faster, however, the secondary derivative is computationally expensive. The quasi-Newton method uses line search, similar as conjugate gradient

methods, but converge faster for quadratic cost function by calculating the inverse of the approximate Hessian matrix at each iteration, which is denoted as $\mathrm{H_k}$.

$\mathrm{H_{k+1}}$ satisfy $x_{k+1} - x_k = H_{k+1}(\nabla f(x_{k+1}) - \nabla f(x_k))$. In each iteration, H_k is updated by adding an correction term U_k. There are algorithms proposed to find the $\mathrm{U_k}$. The Davidon-Fletcher-Powell method(DFP) [44]proposed

$$U_k = \frac{\Delta x_k \Delta x_k{}^T}{\Delta x_k{}^T \Delta g_k} - \frac{(H_k \Delta g_k)(H_k \Delta g_k)^T}{\Delta g_k{}^T H_k \Delta g_k}$$

Where $\Delta g_k = \nabla f(x_{k+1}) - \nabla f(x_k)$ and $\Delta x_k = x_{k+1} - x_k$

BFGS [44] is another widely used quasi-Newton method, where $\mathrm{H_k}$ is updated as the following

$$U_k = \left(1 + \frac{\Delta g_k^T H_k \Delta g_k}{\Delta x_k^T \Delta g_k}\right)\frac{\Delta x_k \Delta x_k^T}{\Delta x_k^T \Delta g_k} - \frac{H_k \Delta g_k \Delta x_k^T + (H_k \Delta g_k \Delta x_k^T)^T}{\Delta x_k^T \Delta g_k}$$

$$H_k = H_{k-1} + \frac{yy^T}{y^T s} - \frac{H_{k-1} s s^T H_{k-1}}{s^T H_{k-1} s}$$

Where $s = x_{k+1} - x_k$ and $y = \nabla f(x_{k+1}) - \nabla f(x_k)$

$$H_k^{-1} = \left(I - \frac{sy^T}{y^T s}\right) H_{k-1}^{-1} \left(I - \frac{ys^T}{y^T s}\right) + \frac{ss^T}{y^T s}$$

3.6 REGULARIZATION

Image registration is an ill-posed problem that the solution is not unique. Therefore additional regularization is usually needed to get a physically realistic solution.

3.6.1 DIFFUSION REGULARIZATION

$\mathrm{L^2}$ norm is quite often used in regularization. Diffusion regularization, also named as Tikhonov regularization or 1st order regularization, is a widely used regularization in image registration. The regularization is defined as:

$$R(T) = \|\nabla T\|^2 = \sum_{x\epsilon\Omega} (\frac{du}{dx})^2 + (\frac{du}{dy})^2 + (\frac{dv}{dx})^2 + (\frac{dv}{dy})^2$$

Where (u, v) is the displacement vector at (x, y). The diffusion regularization attempts to make the displacement smooth. More details can be find in [45].

3.6.2 CURVATURE REGULARIZATION

The curvature regularization proposed in [46] reached good smoothness while automatically correcting the global rigid misalignment. The regularization is defined as

$$R(T) = \|\Delta T\|^2 = (\frac{d^2u}{dx^2})^2 + 2(\frac{d^2u}{dxdy})^2 + (\frac{d^2u}{dy^2})^2 + (\frac{d^2v}{dx^2})^2 + 2(\frac{d^2v}{dxdy})^2 + (\frac{d^2v}{dy^2})^2$$

3.6.3 TOTAL VARIATION REGULARIZATION

Total variation is an l_1-norm regularization. Compared to l_2-norm regularization, the total variation has better edge-preserving capability. This is a desired property in medical image registration because of the sliding between the interfaces of the organs. However, the total variation is computational more complex and might introduce staircase artifact.

The total variation regularization is defined as :

$$R(T) = \|\nabla T\| = |\nabla T|$$

To solve the total variation regularization, it can be reformulated as the following. However this makes the solution unstable because the formula is not differentiable at 0.

$$|\nabla T| \approx \sqrt{\|\nabla T\|^2} = \sqrt{\mathrm{T}^{\mathrm{t}} \nabla^t \nabla T} = \sqrt{(\frac{du}{dx})^2 + (\frac{du}{dy})^2 + (\frac{dv}{dx})^2 + (\frac{dv}{dy})^2}$$

V. Vishnevskiy et al proposed to use Alternating Directions Methods of Multipliers (ADMM) method to solve this problem and the result shows accurate estimation of the motion fields [47].

3.6.4 RIGIDITY PENALTY

Rigidity is estimated by combining the linearity $\partial_{i,j} T_k = 0$, orthogonality $\nabla T^T \nabla T = I$ and orientation preservation $det \nabla T = 1$ [48] [49].

$$R(T) = \frac{1}{2}\left\|\left[\partial_{1,1}T_1, \dots, \partial_{d,d}T_1, \partial_{1,1}T_2, \dots\right]\right\|^2 + \frac{1}{2}\|\nabla T^T \nabla T - I\|^2 + \frac{1}{2}\|det\nabla T - 1\|^2$$

To keep the rigidity locally, a weight function can be applied before integrated into the cost function

$$R_{local}(T) = \|B \cdot T\|^2 \text{ where } B \text{ is the weight function}$$

This problem can be solved as a constrained nonlinear optimization, and sequential quadratic programming can be used to solve it[48,50].

3.6.5 ELASTIC REGULARIZATION

The elastic regularization models the image as an elastic membrane, and the regularization is the internal force. It is defined as

$$R(T) = \frac{\mu}{2}\sum_{i=1}^{K}\left\|\nabla u^i\right\|^2 + \frac{\lambda+\mu}{2}(\nabla \cdot u)^2$$

Where u is the displacement field and u^i is the i-th component of u. μ represent the rigidity or stiffness of the material and λ is the Lamé's first coefficient. The elastic model can derive a smooth motion field, however, might not reach the desired deformation because of the internal force. More detailed description can be found in [51],[52].

3.6.6 FLUID REGULARIZATION

The fluid regularization uses the viscous fluid model to control the deformation

$$R(T) = \frac{\mu}{2}\sum_{i=1}^{K}\left\|\nabla v^i\right\|^2 + \frac{\lambda+\mu}{2}(\nabla \cdot v)^2$$

Where $v = \frac{d}{dt}u(x,t)$ is the velocity field. Fluid regularization allows large deformations and forces them to be continuous. More detailed descriptions can be found in [53].

3.6.7 VOLUME PRESERVING CONSTRAINTS

To achieve volume preserving, additional constraint can be added. Eldad H et al formulate the image registration problem as the following [54]

$$E(u) = E(u; I_F, I_M) + R(u)$$

$$\text{subject to } C(u) = det(I + \nabla u) - 1 = 0$$

Where E is the similarity between fixed image and moving image, R could be any other regularization and $C(u)$ is the volume preserving term.

To solve this problem, [54] used the Sequential Quadratic Programming algorithm.

3.6.8 SHAPE CONSTRAINT

The previous regularization in this section are based on the image information and physical model. Another possible constrain is by introducing user labeled points or contours or automatically detected feature points. For example, suppose $\{\mathrm{p_i}\}$ are the points in the fixed image, and $\{\mathrm{p_i'}\}$ are the points in the moving image, then regularization can be written as

$$R = \sum_{i=0}^{n} \|p_i - p_i'\|^2$$

[55] shows how the contours can be used to make the registration more robust and accuracy.

3.7 EXAMPLES OF IMAGE REGISTRATION FRAMEWORKS

3.7.1 B-SPLINE BASED

For B-spline based image registration, the motion field is controlled by control points as described in 3.3.2.3. Taken SSD similarity as an example:

$$C_{similarity} = \|I_m(T(x)) - I_f\|^2 = \sum_{x \epsilon \Omega} (I_m(T(x)) - I_f)^2$$

To solve the displacement $\varphi_{i,j,k}$ at the control point $(\mathrm{i, j, k})$, the derivative of the measurement matrix then needs to be calculated

$$\frac{dC}{d\varphi_{i,j,k}} = \frac{dC}{dI_m}\frac{dI_m}{dT}\frac{dT}{d\varphi_{i,j,k}}$$

Because

$$\frac{dT(x)}{\varphi_{i,j.k}} = \sum_{l=0}^{3}\sum_{m=0}^{3}\sum_{n=0}^{3} B_3^l(u)B_3^m(v)B_3^n(w)$$

So that

$$\frac{dC}{d\varphi_{i,j,k}} = 2\cdot\sum_{x\epsilon\Omega}(I_m(T(x)) - I_f)\cdot[\frac{\partial I_M}{\partial \mathrm{x}}\ \frac{\partial I_M}{\partial \mathrm{y}}\ \frac{\partial I_M}{\partial \mathrm{z}}]\cdot\sum_{l=0}^{3}\sum_{m=0}^{3}\sum_{n=0}^{3} B_3^l(u)B_3^m(v)B_3^n(w)$$

It needs to be mentioned that $\frac{dC}{d\varphi_{i,j,k}}$ is a vector.

Different regularizations can be added to this framework. For diffusion regularization, the derivative is then

$$\begin{aligned}\frac{dR}{d\varphi_{i,j,k}} &= \sum_{x\epsilon\Omega} 2\cdot(\frac{du}{dx})\cdot\frac{d}{d\varphi_{i,j,k}}(\frac{du}{dx}) + \cdots.\\ &= \sum_{x\epsilon\Omega} 2\cdot(\frac{du}{dx})\cdot\frac{d}{d\varphi_{i,j,k}}(\frac{d}{dx}(\sum_{l=0}^{3}\sum_{m=0}^{3}\sum_{n=0}^{3} B_3^l(u)B_3^m(v)B_3^n(w)\varphi_{i+l,j+m,k+n})) + \cdots.\\ &= \sum_{x\epsilon\Omega} 2\cdot(\frac{du}{dx})\cdot\frac{d}{d\varphi_{i,j,k}}(\sum_{l=0}^{3}\sum_{m=0}^{3}\sum_{n=0}^{3}\frac{dB_3^l(u)}{du}B_3^m(v)B_3^n(w)\varphi_{i+l,j+m,k+n}) + \cdots.\\ &= \sum_{x\epsilon\Omega} 2\cdot(\frac{du}{dx})\cdot(\sum_{l=0}^{3}\sum_{m=0}^{3}\sum_{n=0}^{3}\frac{dB_3^l(u)}{du}B_3^m(v)B_3^n(w)) + \cdots.\end{aligned}$$

For curvature based regularization, the derivative is

$$\begin{aligned}\frac{dR}{d\varphi_{i,j,k}} &= \sum_{x\epsilon\Omega} 2\cdot(\frac{d^2u}{dx^2})\cdot\frac{d}{d\varphi_{i,j,k}}(\frac{d^2u}{dx^2}) + \cdots.\\ &= \sum_{x\epsilon\Omega} 2\cdot(\frac{du}{dx})\\ &\quad\cdot\frac{d}{d\varphi_{i,j,k}}(\frac{d}{dx}(\sum_{l=0}^{3}\sum_{m=0}^{3}\sum_{n=0}^{3} B_3^l(u)B_3^m(v)B_3^n(w)\varphi_{i+l,j+m,k+n})) + \cdots.\\ &= \sum_{x\epsilon\Omega} 2\cdot(\frac{du}{dx})\cdot\frac{d}{d\varphi_{i,j,k}}(\sum_{l=0}^{3}\sum_{m=0}^{3}\sum_{n=0}^{3} B_3^l(u)B_3^m(v)B_3^n(w)\varphi_{i+l,j+m,k+n})\cdot\\ &= \sum_{x\epsilon\Omega} 2\cdot(\frac{du}{dx})\cdot(\sum_{l=0}^{3}\sum_{m=0}^{3}\sum_{n=0}^{3}\frac{d^2B_3^l(u)}{du^2}B_3^m(v)B_3^n(w)) + \cdots.\end{aligned}$$

The B-spline transformation can reach a good computational efficiency, however, sometimes regularization is needed to prevent folding of the deformation field.

3.7.2 ELASTIC REGISTRATION

In elastic registration, the deformation is modeled as an elastic surface deforming under external force and internal force. The external force is the image force, defined by comparing the difference between fixed image and moving image. The internal force represents the smoothness. The image is deformed until equilibrium is reached. In [56], the smoothness constrain is defined based on kinematics of continuum mechanics

$$R(u) = \frac{1}{2}\sum_{i=1}^{3}\sum_{j=1}^{3}\int \lambda(\frac{\partial u_i(x)}{\partial x_i})(\frac{\partial u_j(x)}{\partial x_j}) + \mu(\frac{\partial u_i(x)}{\partial x_j} + \frac{\partial u_j(x)}{\partial x_i})^2 dx$$

The solution satisfies a partial differential equation

$$\mu\nabla^2 u(x) + (\lambda + \mu)\nabla(\nabla \cdot u(x)) = b(x - u(x))$$

where $\nabla = [\frac{\partial}{\partial x_1}, \frac{\partial}{\partial x_2}]^T$ is the divergence operator and $\nabla^2 = \frac{\partial^2}{\partial x_1} + \frac{\partial^2}{\partial x_2}$ is the laplacian operator. $b(x - u(x))$ is the body force $b(x - u(x)) = -\gamma(T(x - u(x)) - S(x)) \cdot \nabla T|_{x-u(x)}$

The elastic registration can provide good result, however there are several limitations. First of all, it assumes linear elasticity, which make the large deformation difficult. Secondly the elastic registration does not guarantee diffeomorphic transformation.

3.7.3 VISCOUS FLUID MODEL

The viscous fluid model allows large and highly localized deformations, therefore is capable to cover large mismatch [57]. However, it can only be applied to single modality images, because it assumes similar intensity between images. In the viscous fluid model, the instantaneous velocity v(x,t) is linked to external forces by Navier-Stokes viscous fluid partial differential equation

$$\alpha\nabla^2 v(x,t) + (\alpha + \beta)\nabla(\nabla^T \cdot v(x,t)) + b(x, u(x,t)) = 0$$

$u(x,t)$ is displacement field, $v(x,t)$ is instaneous velocity, $b(x, u(x,t))$ is the applied force, α and β are the viscous fluid coefficient. The viscous fluid method involves solving a set of partial differential equations and successive relaxation, therefore are computationally expensive.

3.7.4 DEMONS (APPROXIMATION OF FLUID MODEL)

The demon algorithm proposed by [58] is triggered by Maxwell's demon, which consider the image registration as a diffusion process. This algorithm is an approximation of a second order gradient descent on the sum of square of intensity difference criterion [59]. Suppose transformation T(x) maps the pixel x on image I to x on image J, then

$$I\big(T(x)\big) = I(x + u(x)) \sim J(x)$$

The image I deformed by T is $I \circ T^{-1}$, the SSD

$$SSD_I(T) = \int ((T \star I)(x) - J(x))^2 dx = \int (I \circ T^{(-1)} - J)^2$$

$$SSD_J(T) = \int (I - J \circ T)^2 dx = \int (I \circ T^{(-1)} - J)^2 \cdot \left|\nabla T^{(-1)}\right|$$

Suppose $(\nabla_{\mathrm{J}} \circ \mathrm{T})^{\mathrm{T}}$ is the transformed gradient of the image J, then

$$\big(J \circ (T + u)\big)(x) = (J \circ T)(x) + (\nabla_J \circ T)^T \cdot u(x) + \frac{1}{2} u(x)^T \cdot (\mathcal{H}_J \circ T) \cdot u(x)$$

The Taylor expansion of the $SSD_J(T + u)$

$$SSD_J(T + u) = SSD_J(T) + 2 \int (J \circ T - I) \cdot (\nabla_J \circ T)^T \cdot u + \int ((\nabla_{\mathrm{J}} \circ \mathrm{T})^{\mathrm{T}} \cdot \mathrm{u})^2$$

$$+ \int (\mathrm{J} \circ \mathrm{T} - \mathrm{I}) \cdot \mathrm{u}^{\mathrm{T}} \cdot \left(\mathrm{H}_{\mathrm{J}} \circ \mathrm{T}\right) \cdot \mathrm{u} + \mathrm{O}(\|\mathrm{u}\|^2)$$

Define $\nabla_{SSD_J}(T) = 2(J \circ T - I) \cdot \big(\nabla_J \circ T\big)$

$$\mathcal{H}_{SSD_J}(T) = 2\big(\nabla_J \circ T - I\big) \cdot (\nabla_J \circ T)^T + 2(J \circ T - I) \cdot (\mathcal{H}_J \circ T)$$

Which gives the solution

$$u = \frac{(I - J \circ T) \cdot \nabla_I}{\|\nabla_I\|^2 + \alpha \cdot (I - J \circ T)^2}$$

3.7.5 DIFFEOMORPHIC REGISTRATION

A deformation is called diffeomorphic when it is a bijection and its inverse deformation is differentiable. This is a nice property for medical image registration because it preserve the topology of the anatomical structures. For small deformation, the inverse deformation is usually approximated by subtracting the displacement field. However, this hypothesis is not valid for large deformation. In diffeomorphic registration, the transformation is modeled as a composition of a series of small deformations.

$$\frac{dT}{dt} = u_t(T^{(t)}) \text{ with } T^{(0)} = Id$$

where u_t is the velocity field at time t, and $T^{(1)}$ is the final deformation.

The diffeomorphic registration could be based on the viscous fluid model presented in 3.7.3. There are also different solutions proposed, including ANTS[60], DARTEL [61], Diffeomorphic DEMONS [62], LDDMM [63]. In DARTEL, a const flow field is assumed and transformation is then modeled as $T^{(1)}(x) = Exp(u(x))$. Levenberg-Marquardt algorithm is used to solve the problem. In Diffeomorphic DEMONS, the problem is solved iteratively update displacement field u and the transformation T. In addition, the filtering is applied to obtain smooth velocity field.

$$\begin{cases} \mathrm{u} \leftarrow \operatorname{argmin} \|\mathrm{I_F} - \mathrm{I_M}(\mathrm{T}(\exp(\mathrm{u})))\|^2 + \alpha \cdot \operatorname{dist}(\mathrm{T}, \mathrm{T}(\exp(\mathrm{u})))^2 \\ \mathrm{T} \leftarrow \mathrm{T}(\exp(\mathrm{u})) \end{cases}$$

3.7.6 HYPERELASTIC REGISTRATION

Hyperelastic is used to describe the non-linear relationship between strain and stress. Martin B and Modersityki J et al proposed a hyper elastic registration framework to solve the large and non-linear deformation problem [64]. This framework yields diffeomorphic transformation and proved to be particularly useful for higher order similarity measure e.g. mass-preserving registration. The proposed regularization is composed of 3 parts

$$R_{hyper} = \int \alpha_1 length(T) + \alpha_2 surface(T) + \alpha_3 volume(T) dx$$

Where $length(T) = \|\nabla T - I\|^2$, $surface(T) = (\|cof\nabla T\|^2 - 3)^2$ and $volume(T) = ((det\nabla T - 1)^2 / det\nabla T)^2$, with $cof\nabla T$ as the cofactor matrix of ∇T and $det\nabla T$ as the determinant of ∇T. More detailed description about the numerical solution can be find in [64,65].

3.7.7 OPTICAL FLOW

The optical flow algorithm is widely used in computer vision problems. This framework is based on the assumption that the image intensity of the objects is not changed and the changes in the images are caused by the motion.

$$I(u,t) = I(u + \Delta u, t)$$

The right side of the equation can be approximated as

$$I(u + \Delta u, t) \approx I(u,t) + I_x \Delta u_x + I_y \Delta u_y + I_t \Delta t$$

Therefore

$$I_x u + I_y v + I_t \sim 0$$

The formula can be reformed as

$$I(x,y) - I_t(x,y) = [u_x(x,y), u_y(x,y)] \begin{bmatrix} \frac{\partial I}{\partial x} \\ \frac{\partial I}{\partial y} \end{bmatrix}$$

The solution is

$$\begin{bmatrix} u_x(x,y) \\ u_y(x,y) \end{bmatrix} = \frac{(I - I_t)}{\left(\frac{\partial I}{\partial x}\right)^2 + \left(\frac{\partial I}{\partial y}\right)^2} \begin{bmatrix} \frac{\partial I}{\partial x} \\ \frac{\partial I}{\partial y} \end{bmatrix}$$

To avoid the singularity problem, additional term is added

$$\begin{bmatrix} u_x(x,y) \\ u_y(x,y) \end{bmatrix} = \frac{(I - I_t)}{(\frac{\partial I}{\partial x})^2 + (\frac{\partial I}{\partial y})^2 + (I - I_t)^2} \begin{bmatrix} \frac{\partial I}{\partial x} \\ \frac{\partial I}{\partial y} \end{bmatrix}$$

The optical flow works well with small motion, therefore a multi-level approach as in 3.2 is often used to overcome this problem. A variety of methods has been proposed to improve the results. Sun et al evaluated different optimization techniques and implementations and proposed using median filter to improve the registration at boundaries [66]. Brox et al integrated rich descriptors into the optical flow setting to get good results for large displacements [67].

In the following work, the optical flow based registration combined with a multi-level approach and different regularization terms is used for image alignment and motion field extraction. The advantage of this framework is that it could provide accurate deformation estimation with efficient computation. In this framework, SSD is chosen as cost function, which could cover our use case for motion extraction from cine images and is easy to implement. For T_1 images with different contrast, histogram matching can be used as a

preprocessing step before registration (Chapter 4). This framework is fully compatible with the regularizations presented in section 3.6. In practice we choose to use linear operators for regularization, e.g. smoothness constraint, local divergence etc. Those linear operators have explicit analytical gradient description and allow the efficient optimizers like Gauss-Newton method. In addition, we proposed to use regional based regularization instead of global regularization, which could better model the deformation in different tissues and compartments in the heart (Chapter 5).

Chapter 4 Optimization on cardiac T_1 mapping

In this chapter we aim at optimizing the workflow for T_1 mapping, which is nowadays one the most popular MRI imaging techniques for quantitative tissue characterization. Challenges that have not been fully resolved in current clinical practice include: (i) the need to correct for patient motion (due to imperfect breath-holding and cardiac motion); (ii) the need to improve the accuracy and precision (especially noise-robustness) of the quantitative T_1 values; (iii) the need to improve the computational efficiency of the model fitting, as it is foreseeable that the 2D sequences used today for T_1 mapping will be generalized to high-resolution 3D sequences in the near future, as a result of novel acquisition/reconstruction techniques. This chapter focus specifically on the second and third points. To this end, we propose improvements of the conventional model fitting techniques to include spatial regularization (denoising) while providing a computationally efficient implementation that will be applicable for large scale 3D datasets.

The work described in this chapter was published in S.Liu et al, "A vectorized Levenberg-Marquardt model fitting algorithm for efficient post-processing of cardiac T_1 mapping MRI" and S.Liu et al, "GPU Implementation of Levenberg-Marquardt Optimization for T_1 Mapping"

4.1 RELEVANT STUDIES

Cardiac fibrosis is caused by excessive deposition of myocardial collagen and is accompanied by many myocardial diseases [68,69] . Thanks to the rapid development of cardiac magnetic resonance imaging, the myocardial structure change can be assessed noninvasively by measuring the pixel-wise longitudinal relaxation time (T_1) of the heart tissue, before and/or after injection of a gadolinium-based contrast agent [70]. Cardiac T_1 maps are generally produced using a series of images acquired after a variable delay following the flipping of the magnetization, which allows a sampling of the T_1 relaxation curve for each pixel. The most commonly used acquisition schemes are inversion recovery (IR) sequence and saturation recovery (SR) sequence. IR techniques such as MOLLI [21]

are most commonly used due to their larger dynamic range and better precision and reproducibility, whereas SR techniques such as SASHA or SMART1Map [26] provide more accurate T_1 values [71]. For both sequences, a typical series contains 8 to 11 images with different inversion/saturation time. Then an exponential model fitting is performed for each pixel by using nonlinear least-squares optimization. Different models, e.g., the 2-parameter model and the 3-parameter model, are proposed to optimize the T_1 measurement depending on the acquisition sequence[12].

The accuracy and precision of T_1 mapping depends on many factors :

- The number of measurements (i.e., the number of input images)
- The number of parameters chosen for the fitting model (2 or 3)
- The algorithm used for the nonlinear optimization
- The choice of initial parameters for curve fitting
- The presence of artifacts and misregistration between the images

A lot of work has focused on investigating the acquisition sequence and motion correction techniques [13,72–74]. Fitting the recovery curve from magnitude images is a well-known difficulty in IR sequences because the phase of the complex MR signal is lost during the magnitude reconstruction. In [75], a multi-fit algorithm has been proposed to solve this problem, however it is relatively inefficient because multiple fits have to be performed. An alternative method is to use phase-sensitive reconstruction and restore the signal polarity in the images [76]. However, the phase data are not always clinically available. Moreover, accurate reconstruction of the phase signal is difficult in MRI because such method requires accurate calibration of the phase of the transmitting and receiving coils (typically 8 to 30+ receiver channels in cardiac MRI), and good coil combination algorithm is still a research topic [77,78]. In [79], Bloch Equation simulations combined with FLASH readout has been proposed to improve the robustness, however, this requires excessive simulation process. An inversion group fitting algorithm has also been proposed to better model the inversion recovery behavior [80].

Application of the Levenberg-Marquardt method to myocardial T_1 mapping was achieved using various model fitting functions. In the ideal case, a 2-paramater model was used, $y(t) = A \cdot (1 - \exp(-t/T_1))$ for SR experiments and $y(t) = A \cdot |1/2 - \exp(-t/T_1)|$ for

IR. The third parameter C can be added to model the imperfect saturation/inversion – e.g. which can be caused by transmit B1 field inhomogeneities or by apparent loss of saturation/inversion efficiency due to the readout pulses [81]. More generally, this C parameter can model other sources of bias in the acquisition. In particular the bias introduced by the non-central noise distribution (i.e. Rician noise in the magnitude MR images) is intrinsically taken into account in this 3-parameter model.

Model based image reconstruction has been investigated to accelerate the parametric mapping. In [82], compressed sensing has been used to reconstruct the parametric map using overcomplete dictionaries. Model based methods can also be used to estimate the T_2 maps and spin-density maps from the raw data [15]. Regularization has also been proposed to reduce the noise in the parametric map reconstruction [83]. However, all these methods need the raw image data and required time-consuming reconstruction methods. In the image domain, Poot et al. proposed an elegant framework based on maximum likelihood or maximum a posteriori estimation[84]. This approach can simultaneous estimate the parametric maps and noise maps with spatially smooth noise levels. This approach was shown to improve the precision of quantitative parameter estimation in diffusion tensor MRI.

In this work, we propose an alternative approach to optimize the model fitting process by reformulating the problem as a joint optimization whereby the T_1 models of all pixels in the image are solved simultaneously, using a matrix formulation. The hypothesize is that this matrix formulation has two benefits: (i) it provides a vectorized version of the Levenberg-Marquardt algorithm which is more computationally efficient than the standard pixel-wise approach and is particularly well suited for modern architectures such as vector CPUs or graphics processor units (GPUs); (ii) it makes additional constraints possible, spatial regularization can be incorporated into the optimization to stabilize the fitting process and speed up convergence.

In this section the optimized workflow is presented with the following focus points:

- The proposed vectorized Levenberg-Marquardt algorithm and its exemplary implementation for saturation recovery data and inversion recovery data with 2-parameter and 3-parameter model.

- Special care is given to the initialization: an automatic image segmentation technique is used as a preprocessing step to compute region-wise estimates of the model parameters (including T_1), which are used as initial guesses for the final vectorized T_1 fitting procedure.
- SSD based non-rigid registration techniques with histogram matching [73,74,85] have been applied to minimize the artifact caused by motion.

The evaluation of the optimized workflow is presented in Chapter 6.

4.2 THEORY

4.2.1 BACKGROUND ON LEVENBERG-MARQUARDT OPTIMIZATION

For simplicity purposes, we first consider the model fitting problem for one pixel. Suppose $f(p)$ is the model that describe the relaxation process, where p is the unknown parameter set that we would like to estimate. p is a vector of a N_p elements ($N_p = 2$ or 3 here). The parameter estimation problem can be treated as a least-squares minimization of the error between the predicted value based on unknown parameter set p and the acquired data y, which is a vector of N_m measurements ($N_m = 8$ to 11 in this work):

$$\min_p \|f(p) - y\|^2. \quad \textbf{(1)}$$

Levenberg-Marquardt algorithm (LM) [86–88] is a popular choice for solving Eq (1) when the function $f(p)$ is nonlinear. This method starts an iterative searching process from p_0, an initial guess of the parameters. In each iteration, an optimal refinement of the parameters δp is obtained by linearizing the cost function around the current estimate:

$$\min_{\delta p} \|f(p + \delta p) - y\|^2 \approx \min_{\delta p} \left\|J(p)\delta p - \big(y - f(p)\big)\right\|^2, \quad \textbf{(2)}$$

Where $J(p)$ is the Jacobian matrix of f with respect to the parameters, evaluated at the current iteration. $J(p)$ is of size $N_m \times N_p$. Therefore, LM involves solving a sequence of linear least squares problems. Usually a damping factor λ_k is added in order to get a good balance between robustness and speed. The calculated update of the solution at a given iteration k is then:

$$\delta p = p_{k+1} - p_k = (J(p_k)^T J(p_k) + \lambda_k Id)^{-1} J(p_k)^T \big(y - f(p_k)\big), \quad \textbf{(3)}$$

Where Id is the identity matrix and λ_k is the LM regularization coefficient which is adapted throughout iterations. The rationale of LM is to start with a large value of λ_k, so the method behaves like a steepest gradient descent in the beginning, then decrease λ_k as p approaches the solution, so the method behaves like a quasi-Newton method in the last iterations. Such schemes – i.e. combining gradient descent and quasi-Newton - are thought to yield optimal convergence speed in the nonlinear optimization literature. Several variations of the LM technique have been proposed depending on the choice of λ_0, update rule for λ_k and stopping condition. Here we choose the following update rule [88]:

$$\begin{cases} if\ \rho(p) > \varepsilon, set\ p_{k+1} = p_k + \delta p, \lambda_{k+1} = min(\lambda_k \times 2, 10^7) \\ if\ \rho(p) \leq \varepsilon, do\ not\ update\ p_k\ , \lambda_{k+1} = max(\ \lambda_k/2\ , 10^{-7})' \end{cases} \quad \textbf{(4)}$$

$$\text{with } \rho(p) = \frac{\|f(p)\|^2 - \|f(p+\delta p)\|^2}{\|f(p)\|^2 - \|f(p) + J(p)\delta p\|^2},$$

and iterations are stopped when $\|p_{k+1} - p_k\| / \|p_{k+1}\| < \tau$, where τ a given tolerance, or when a maximal number of iterations was reached. Table 2 shows the pseudo code the classic LM-algorithm.

Table 2. Pseudo code for LM-algorithm

INPUT: data y, inversion time,
Initialize parameter p_0
For iteration k
Get linearized problem using p_k and y
Solve linear equation Aδp = b
Update parameter $p_{k+1} = p_k + \delta p$, update λ
Check convergence
End
OUTPUT: p

4.2.2 VECTORIZED LEVENBERG-MARQUARDT FORMULATION

In computer programming, one typical way to improve the performance of an algorithm is vectorization. This consists of redesigning algorithms so that the same operations

performed multiple times on different data are grouped into a single operation performed once on a large array of data. Vectorization generally results in improved performances as modern computer architecture (CPU or GPU) can efficiently perform these vector operations. In our case, the vectorization means processing all the pixels jointly. Besides improving performance, It also provide the possibility to incorporate constraints such as spatial smoothness to improve the processing itself.

In order to formulate the vectorized version of LM for an image of N_{pix} pixels, we use the same framework as described in the previous section. f is the fitting model function, but operate on whole image. p is the concatenated parameter maps, a vector of $N_{pix}N_p$ elements. And y is the whole acquired image dataset, a vector of $N_{pix}N_m$ elements. In addition, a spatial smoothness constraint is added. This leads to a vectorized version of Eq. (1):

$$\min_p \|f(p) - y\|^2 + \mu\|Gp\|^2, \quad \textbf{(5)}$$

where μ is a scalar, controlling the spatial regularization weight and G is an operator returning a concatenation of the spatial gradients of each parameter map, computed by forward differences. G is a sparse matrix of size $N_{dims}N_{pix}N_p \times N_{pix}N_p$, with N_{dims} the number of dimensions in the image (here $N_{dims} = 2$). The vectorized LM update formula becomes:

$$\delta p = (J(p_k)^T J(p_k) + \Lambda_k + \mu G^T G)^{-1} J(p_k)^T (y - f(p_k) - \mu G^T G p_k) \ . \quad \textbf{(6)}$$

Note that the term $\lambda_k Id$ in Eq. (3) has been substituted by a diagonal matrix Λ_k, the diagonal elements of which contain the map of LM regularization coefficients at iteration k. $J(p_k)$ is now a large sparse matrix of size $N_{pix}N_m \times N_{pix}N_p$.

In contrast to the previous section, here the large sparse matrix inversion involved in Eq. (6) can be solved efficiently using iterative methods (here the conjugate gradient was used). It should be noted that the computational burden of such methods is mainly constrained by the application of the matrix operator to be inverted. In the present case, the forward and transpose Jacobian matrices are more efficiently applied if the following bracket priority rule is respected: $x \mapsto J(p_k)^T (J(p_k)x)$. Update rules for the LM regularization coefficients maps and stopping conditions are the same as in the pixel-wise

case (note that the stopping condition now applies to the whole parameter map vector). It needs to be mentioned that the LM regularization coefficient is now a map, each pixel has its own LM regularization coefficient.

4.3 T_1 MAPPING WORKFLOW

4.3.1 NON-RIGID REGISTRATION

Despite ECG gating and breath-holding during the image acquisition, there is still residual motion. Therefore non-rigid registration was applied to each series before model fitting. The image with longest saturation/inversion time was chosen as the reference image for the registration. The sum of squared difference (SSD) is used as cost function and the optimization is achieved by a multi-resolution Gauss-Newton technique. To compensate for the contrast changes, histogram matching is performed before the registration. A more detailed description of the algorithm can be found in [89].

4.3.2 DEFAULT AND REGION-BASED INITIALIZATION

Two initialization scheme are tested:

- Default initialization: an average relaxation rate 1000 ms is chosen as the initial value of T_1. For parameter A, the image intensity at infinite saturation times is used for saturation recovery data, and the maximum intensity is used for inversion recovery data. For parameter C, 0 is used for saturation recovery and the negative maximum intensity is selected for inversion recovery. Detailed expressions for the default initial guesses are given in Table 3. Here I_{Nt} is the image at infinite inversion/saturation time and I_{t} is the image at inversion time *t*.

Table 3. T1 fitting models and default initial values

	N parameters	Model	A_0	C_0
Saturation-recovery	3	$\mathrm{y_t} = \mathrm{A} * \left(1 - \mathrm{e}^{-\frac{\mathrm{t}}{\mathrm{T}}}\right) + \mathrm{C}$	$\mathrm{A}_0(\mathrm{i},\mathrm{j}) = \mathrm{I}_{\mathrm{Nt}}(\mathrm{i},\mathrm{j})$	$\mathrm{C}_0(\mathrm{i},\mathrm{j}) = 0$
	2	$\mathrm{y_t} = \mathrm{A} * \left(1 - \mathrm{e}^{-\frac{\mathrm{t}}{\mathrm{T}}}\right)$	$\mathrm{A}_0(\mathrm{i},\mathrm{j}) = \mathrm{I}_{\mathrm{Nt}}(\mathrm{i},\mathrm{j})$	-
Inversion-recovery	3	$\mathrm{y_t} = \left\lvert \mathrm{A} * \left(1 - \mathrm{e}^{-\frac{\mathrm{t}}{\mathrm{T}}}\right) + \mathrm{C} \right\rvert$	$\mathrm{A}_0(\mathrm{i},\mathrm{j}) = \max\{\mathrm{I_t}(\mathrm{i},\mathrm{j})\}$	$\mathrm{C}_0(\mathrm{i},\mathrm{j}) = -\max\{\mathrm{I_t}(\mathrm{i},\mathrm{j})\}$
	2	$\mathrm{y_t} = \left\lvert \mathrm{A} * \left(0.5 - \mathrm{e}^{-\frac{\mathrm{t}}{\mathrm{T}}}\right) \right\rvert$	$\mathrm{A}_0(\mathrm{i},\mathrm{j}) = \max\{\mathrm{I_t}(\mathrm{i},\mathrm{j})\}$	-

- Region based initialization: In this scheme pixels are grouped into a number of regions using a graph-based image segmentation technique [90]. This technique subdivides the image into a reduced number of connected regions, avoiding small "islands" to be created. Then the standard LM fitting is applied to each region using averaged signal intensities from all pixels inside this region. The parameters obtained from this fast computation in each region are then used as initial guesses for further optimization on the whole image, using either the standard pixel-wise or the vectorized LM algorithm. The validity of this region-wise model fit is checked based on the R^2 error of fitting ($R^2 > 0.97$). This threshold has been proposed in previous studies on myocardial T_2 mapping as a quality index to exclude outlier pixels/regions from the analysis [85,91].When this condition is not met, the default initial guess is used for the corresponding region. This second initialization scheme is termed as region-based initialization in the remainder.

4.3.3 Model Fitting Implementation

Application of the LM method to myocardial T_1 mapping was achieved using various model fitting functions. As described in previous section, both 2-parameter model and 3-parameter model are used in clinical application. In both case, the vectorized algorithm can be used, however, the Jacobian matrix is slightly different. Detailed expressions needed for the vectorized LM implementation (including the fitting functions and Jacobian matrices) are summarized in Table 4 and Table 5.

Table 4. Mathmatic model for SMART1Map

	SMART1Map,3 parameter	SMART1Map,2 parameter
Formula	$y = f(t;a,b,c) = a\left(1 - e^{-\frac{t}{b}}\right) + c$	$y = f(t;a,b) = a\left(1 - e^{-\frac{t}{b}}\right)$
Vectorization	$\begin{bmatrix} Y_{t_0} \\ \vdots \\ Y_{t_n} \end{bmatrix} = \begin{bmatrix} diag(A) & \cdots & 0 \\ \vdots & \ddots & \vdots \\ 0 & \cdots & diag(A) \end{bmatrix} (1 - \begin{bmatrix} e^{-\frac{t_0}{B}} \\ \vdots \\ e^{-\frac{t_n}{B}} \end{bmatrix}) + \begin{bmatrix} C \\ \vdots \\ C \end{bmatrix}$	$\begin{bmatrix} Y_{t_0} \\ \vdots \\ Y_{t_n} \end{bmatrix} = \begin{bmatrix} diag(A) & \cdots & 0 \\ \vdots & \ddots & \vdots \\ 0 & \cdots & diag(A) \end{bmatrix} (1 - \begin{bmatrix} e^{-\frac{t_0}{B}} \\ \vdots \\ e^{-\frac{t_n}{B}} \end{bmatrix})$
Jacobian	$J = \begin{bmatrix} diag(1 - e^{-\frac{t_0}{B}}) & \ldots & diag(1 - e^{-\frac{t_n}{B}}) \\ \frac{-t_0 diag(A) * e^{-\frac{t_0}{B}}}{diag(B) * diag(B)} & \ldots & \frac{-t_n diag(A) * e^{-\frac{t_n}{B}}}{diag(B) * diag(B)} \\ I & \ldots & I \end{bmatrix}$	$J = \begin{bmatrix} diag(1 - e^{-\frac{t_0}{B}}) & \ldots & diag(1 - e^{-\frac{t_n}{B}}) \\ \frac{-t_0 diag(A) * e^{-\frac{t_0}{B}}}{diag(B) * diag(B)} & \ldots & \frac{-t_n diag(A) * e^{-\frac{t_n}{B}}}{diag(B) * diag(B)} \end{bmatrix}$

Table 5. Mathmatic model for MOLLI

	MOLLI, 3 parameter	MOLLI, 2 parameter
Formula	$y = f(t;a,b) = \left\lvert a\left(1 - e^{-\frac{t}{b}}\right) + c\right\rvert$	$y = f(t;a,b) = \left\lvert a\left(0.5 - e^{-\frac{t}{b}}\right)\right\rvert$
Vectorization	$\begin{bmatrix} Y_{t_0} \\ \vdots \\ Y_{t_n} \end{bmatrix} = \left\lvert \begin{bmatrix} diag(A) & \cdots & 0 \\ \vdots & \ddots & \vdots \\ 0 & \cdots & diag(A) \end{bmatrix} \left(1 - \begin{bmatrix} e^{-\frac{t_0}{B}} \\ \vdots \\ e^{-\frac{t_n}{B}} \end{bmatrix} \right) + \begin{bmatrix} C \\ \vdots \\ C \end{bmatrix} \right\rvert$	$\begin{bmatrix} Y_{t_0} \\ \vdots \\ Y_{t_n} \end{bmatrix} = \left\lvert \begin{bmatrix} diag(A) & \cdots & 0 \\ \vdots & \ddots & \vdots \\ 0 & \cdots & diag(A) \end{bmatrix} \left(0.5 - \begin{bmatrix} e^{-\frac{t_0}{B}} \\ \vdots \\ e^{-\frac{t_n}{B}} \end{bmatrix} \right) \right\rvert$
Jacobian	$J = \begin{bmatrix} diag(1 - e^{-\frac{t_0}{B}}) & \cdots & diag(1 - e^{-\frac{t_n}{B}}) \\ \frac{-t_0 diag(A) * e^{-\frac{t_0}{B}}}{diag(B) * diag(B)} & \cdots & \frac{-t_n diag(A) * e^{-\frac{t_n}{B}}}{diag(B) * diag(B)} \\ I & \cdots & I \end{bmatrix} \cdot \begin{bmatrix} sign(diag(A) * \left(1 - e^{-\frac{t_0}{B}}\right) + C) \\ \vdots \\ sign(diag(A) * \left(1 - e^{-\frac{t_n}{B}}\right) + C) \end{bmatrix}$	$J = \begin{bmatrix} diag(1 - e^{-\frac{t_0}{B}}) & \cdots & diag(1 - e^{-\frac{t_n}{B}}) \\ \frac{-t_0 diag(A) * e^{-\frac{t_0}{B}}}{diag(B) * diag(B)} & \cdots & \frac{-t_n diag(A) * e^{-\frac{t_n}{B}}}{diag(B) * diag(B)} \end{bmatrix} \cdot \begin{bmatrix} sign(diag(A) * \left(1 - e^{-\frac{t_0}{B}}\right) + C) \\ \vdots \\ sign(diag(A) * \left(1 - e^{-\frac{t_n}{B}}\right) + C) \end{bmatrix}$

In Table 4 and Table 5, a,b,c are scalar, represent the T_1 relaxation parameter for each pixel. A,B,C are vectors, represent the T_1 relaxation parameter for all the pixels within the image. Diag(A) is a sparse matrix that take all elements in A and create a diagonal matrix.

The initial LM regularization coefficient was set to $\lambda_0 = 0.01$. The maximum number of LM iterations was set to 20. The tolerance for stopping iterations was set $\tau = 10^{-6}$ in both the pixel-wise case and the vectorized case. The spatial constraint weight was set to $\mu = 10^{-6}$ as default. To evaluate the goodness of the model fitting, the coefficient of determination R^2 was calculated.

4.4 Optimization on GPU

In this section, the T_1 mapping curve fitting using pixel-wise and the vectorized Levenberg-Marquardt algorithm described in 4.2 is further improved on GPU.

4.4.1 Technical background

GPU is designed with multiple processing unit (multiple multiprocessors), which allows the parallel processing of multiple data (SIMD strategy). This perfectly fit for most image processing task. Each multiple processor is called a block. A block can run multiple threads simultaneously. Threads within one block can be synchronized, which allows flexible

management of the threads. There are different types of memory on the GPU. Global memory, texture memory and constant memory can be accessed by all the thread. For each block, there is also shared memory that can be accessed only by the threads within the block.

CUDA is the application programming interface that allows the code to run on NVIDA GPU devices. In CUDA programming, kernel functions are implemented. The parallelization is realized by calling those kernel functions.

4.4.2 PIXEL-WISE LEVENBERG-MARQUARDT ALGORITHM ON GPU

Here 16x16 block size and 16x16 grid size are used to cover the 256x256 image size. Each image pixel is processed independently by a thread. Figure 18 shows an example calling of the kernel function. The kernel function is a small scale Levenberg-Marquardt solver, which solves a 3-paramter or 2-parameter non-linear curve fitting problem.

```
dim3 block(16,16,1);
dim3 grid(16,16,1);
// curve fitting
curve_fit_element_wise<<<grid, block>>>(p_ti, p_images,seq_type,
                    Nt,output,nparam, tol, max_iter_lm, init_lambda);
```

Figure 18. Illustration of the curve fitting kernel

4.4.3 VECTORIZED LEVENBERG-MARQUARDT ALGORITHM ON GPU

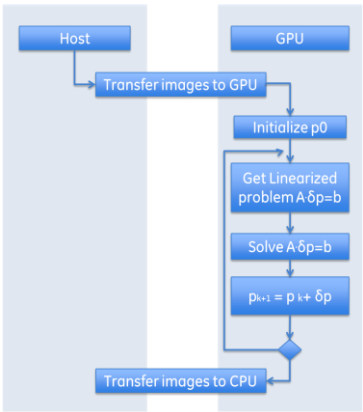

Figure 19. Workflow of vectorized curve fitting

In the vectorized version, the same steps for Levenberg-Marquardt algorithm are adopted, as shown in Figure 19. However, most of the work is done on the GPU.

For the vectorized curve fitting, a large matrix J^TJ needs to be calculated. Since J^TJ is a block-wise diagonal matrix, as shown in Figure 20. The image intensity at pixel i only affect the value of J^TJ at $(i + m \cdot N_{pix}, i + n \cdot N_{pix})$ where $m, n \in \{0,1,..N_p - 1\}$.

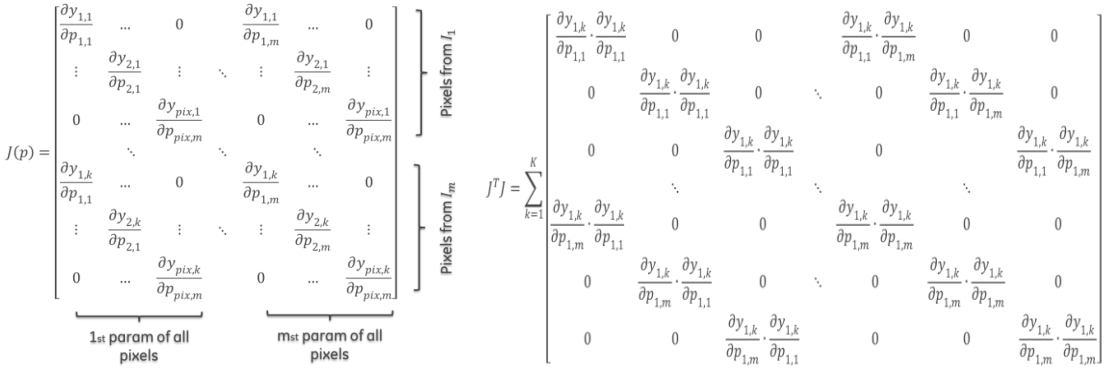

Figure 20. Description of Jacobian matrix and J^TJ

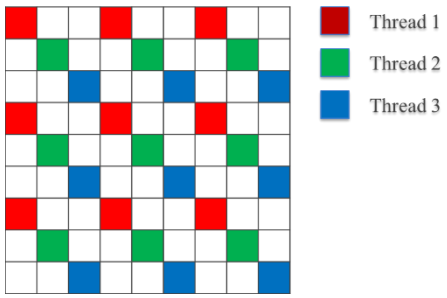

Figure 21. Illustration of J^TJ matrix for 3 pixels using 3 parameter model

Figure 21 shows an example image of 3 pixels using 3 parameter model fitting. Each thread works on one pixel, and fills the corresponding value in J^TJ.

The most time consuming part of the vectorized Levenberg-Marquardt algorithm is the solving of the linear equation. The QR factorization method from the standard CUDA library 'cuSolver' was first tested. The method works well. However, it costs relative longer time. Therefore a conjugate gradient solver [92] is implemented to accelerate the speed. The conjugate gradient algorithm searches iteratively in the conjugate direction, and is more suitable for large scale problems as we have. The implementation is based on the CUDA cuBLAS library.

Chapter 5 Strain analysis from 3D cine images

Cardiac MRI is the gold standard to assess global cardiac function. This is because it provides high-quality images of the cardiac cycle with a full spatial coverage of the heart (unlike ultrasound echography) and good temporal resolution (unlike computed tomography), which allows very accurate calculation of blood cavity and myocardium volumes. However, cardiac MRI does not currently allow quantification of regional contractile abnormalities as accurately as ultrasound (speckle tracking and Doppler techniques remain the clinical routine for this purpose). Although some dedicated MRI sequences have been developed to fill this gap (e.g., tagging MRI), they require additional scan time and are generally not included in clinical protocols, because it usually takes 30 to 45 minutes. An alternative would be to use the routinely acquired cine images to extract information about local cardiac function. Attempts have been made with methods such as feature tracking. One source of inaccuracy lies in the fact that, clinical cine images are usually acquired as thick 2D slices (8 mm thickness). However, with novel acquisition and reconstruction techniques, it is possible to obtain 3D cine images with an isotropic resolution of 1.5 mm, which are more suitable for analyzing 3D motion patterns of myocardial segments. Therefore, in this chapter, we focus on the analysis of such 3D cine datasets obtained using a recently developed motion-corrected super-resolution technique.

The main challenge in doing so is that the extraction of deformation information (i.e., strain) requires accurate non-rigid image registration of the beating heart. This is a difficult problem because cine images do not provide local tissue labeling information as in tagging MRI or speckle tracking ultrasound. Therefore only the contours of the myocardium can be reliably identified, making the registration results highly dependent on the regularization constraints. As a consequence, the subsequent motion analysis is also affected. Therefore, novel regularization schemes are proposed, as well as novel indices for statistical analysis.

5.1 WHAT IS STRAIN AND WHY IS STRAIN NEEDED?

5.1.1 BACKGROUND

Cardiac strain ε is a measurement of the myocardial fiber deformation relative to its initial length. Suppose L_0 is the initial length of the fiber, L is the final length of the fiber and ΔL is the change of the tissue length. The stretch ratio is defined as λ.

$$\lambda = \frac{\mathrm{L}}{\mathrm{L_0}}$$

There are different definitions of strain:

- Engineer strain, also called Cauchy strain, is the most widely used strain definition for mechanical and structural engineering

$$\varepsilon = \lambda - 1 = \frac{\Delta \mathrm{L}}{\mathrm{L_0}}$$

- Natural strain is also called true strain, which is defined as the time integration of the rate of deformation tensor. This definition provides better measurement when the deformation takes place in a series of increment.

$$\mathrm{E} = \ln\lambda = \ln\frac{\mathrm{L}}{\mathrm{L_0}}$$

- Lagrange strain

$$\varepsilon = \frac{1}{2}(\lambda^2 - 1)$$

- Euler strain

$$\varepsilon = \frac{1}{2}(1 - \frac{1}{\lambda^2})$$

The strain value calculated by different definitions are not directly comparable, however, there is no good or bad definition of the strain. Negative strain means shortening of the myocardial tissue and positive means elongation.

Strain rate is defined as the time gradient of strain. Strain rate can be used to describe how fast myocardial deformation occurs.

$$SR = \frac{\Delta\varepsilon}{\Delta t} = \frac{\Delta\frac{\Delta L}{L}}{\Delta t} = \frac{\Delta v}{L}$$

In the 2D and 3D cases, strain is described by a tensor.

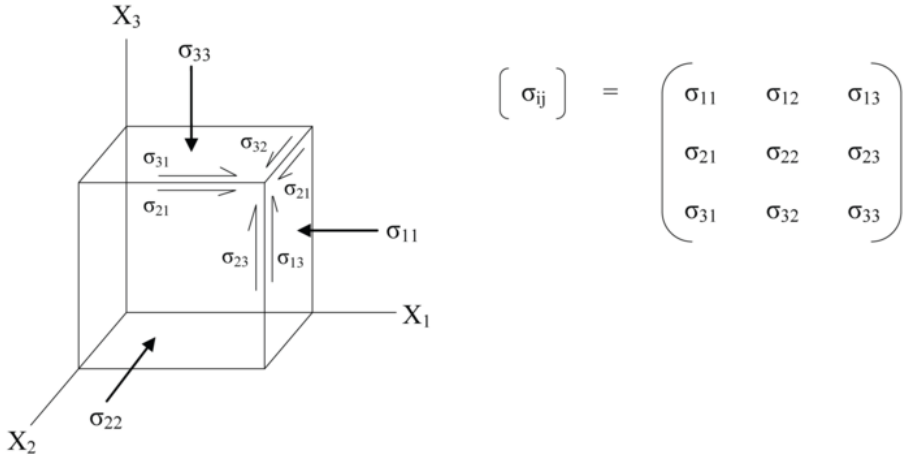

Figure 22. Illustration of 3D strain.

5.1.2 CLINICAL APPLICATION

Myocardial strain can be used as an important parameter to predict and diagnose myocardial dysfunction. It has been proved that myocardial strain correlates well with stroke volume and fibrosis, while strain rate reflects end-systolic elasticity [93]. The inter-segmental variability in the timing of peak myocardial strain has been suggested as a predictor of the risk of ventricular arrhythmias[94]. In [95], the relationship between longitudinal strain and the risk for heart failure was analyzed. The result shows that subjects with dyspnea have lower subendocardial/subepicardial longitudinal strain ratios.

Moreover, myocardial strain can be used to estimate regional function as well as global function of the heart, especially for heart failure with preserved ejection fraction. Global longitudinal strain (GLS) is more sensitive than left ventricular ejection fraction (LVEF) as a measure of systolic function and therefore can be used to identify subclinical LV dysfunction in cardiomyopathies [94]. Choi et al. (2009) showed that longitudinal 2D strain can be used to predict coronary artery disease [96]. The transmural strain is a function of wall shortening, wall thickness, and chamber diameter, whereas

circumferential shortening is mainly a function of wall thickening. It has been clinically shown that longitudinal strain rate and wall thickening are diagnostically equivalent.

5.1.3 DUCHENNE MUSCULAR DYSTROPHY

Duchenne Muscular Dystrophy (DMD) is a progressive myocardial muscular disease caused by genetic mutation. The DMD is accompanied with increased intracellular calcium level and appearance of fibrosis. The fibrosis usually begins from the epi-cardial surface of the posterior wall. The cardiomyopathy can happen as early as 10 years old [97,98]. However, the left ventricle function might not be affected in the early stage. Therefore 2D strain analysis is usually performed to detect and evaluate the early involvement. [99] shows that strain and strain rate are important parameters for the early detection of myocardial abnormalities.

Table 6. Myocardial strain for DMD group and control group [100].

	DMD	Control	P
Longitudinal strain(epi)	-9.3±3.8%	-12.3±4.3%	p=0.012
Radial strain	24.1±11.1%	37.3±25.9%	p=0.027
Circumferential strain (endo)	-17.5±4.7%	-24.2±5.3%	p<0.001
Circumferential strain (myo)	-12.7±3.8%	-18.0±4.0%	p<0.001
Circumferential strain (epi)	-8.4±4.0%	-12.2±5.0%	p=0.006

Currently, the clinical standard for DMD examination is Doppler echography. Mori K et al (2007) measured the peak systolic radial strain using Doppler echography [101]. The result shows a decrease in the posterial wall radial strain while no significant difference was found in the interventricular septum. [100] gave a more thorough study on the myocardial strain between DMD patient and control group using 2D echography imaging. The result shows that the myocardial strain in longitudinal, radial and circumferential directions are lower in the DMD group compared to the control group, and the difference in circumferential direction is significant. The values are shown in Table 6.

Another widely used imaging modality to estimate the myocardial strain is tagged MRI. Hor KN et al. (2009) investigated 70 DMD patients [102], the results showed a decrease of circumferential strain in DMD patients (<10 years old) compared to the control group and a continuous decrease in circumferential strain as age increases.

5.2 RELEVANT STUDIES ON MYOCARDIAL STRAIN

Myocardial strain analysis has been performed using different image modalities and with different methods. In [14] an overview of the current state of strain analysis was given and different techniques were compared.

To date, most researches have been performed using ultrasound images. Tissue-Doppler imaging is used to estimate strain by directly measuring tissue velocity. Speckle tracking echography(STE) further improved the reproducibility and accuracy by using the speckles created from the interaction between the ultrasound beam and tissue, providing a labeling of the moving tissues that can be tracked in a post-processing step [93].

However, MRI, as gold standard for the diagnosis of heart diseases, gains more and more interests. There are different MRI techniques to evaluate the myocardial deformation. Available imaging techniques include CMR tagged imaging, phase velocity mapping, DENSE encoding and strain encoded imaging (SENC)[103]. Tagged imaging is based on the selective saturation of myocardial tissue on different planes. Before imaging, the myocardial tissue is labeled by a selective radiofrequency pulse, generally with a grid-shape pattern. During myocardial contraction, the labeled tissue pattern remains visible as it undergoes deformation, and can be tracked by post-processing software to estimate the myocardial motion. There is a good correlation between tagging results and tissue Doppler imaging.

In recent years, some strain researches have been performed on cine images. Compared with tagged MRI, cine images are more widely available. In [104], strain from 2D cine images was compared with strain from tagging images. The result shows that radial strain from cine images is overestimated, while there is no significant difference for circumferential strain. Moreover, the strain pattern was different for the myocardial infarction region and for the normal region. In [105], the strain results from cine images have been validated against DENSE imaging and the circumferential strain extracted from cine images shows comparable diagnostic performance.

For post processing, there are two categories of methods for measuring strain from MRI images: Feature tracking and deformation tracking (image registration). In [105],

deformation tracking was used to extract the motion field, the result shows better reproducibility than feature tracking. Different methods were used to analyze the data, including general flow analysis, block matching, image registration, and model-based algorithms.

In [106], a hierarchical model was used to obtain the motion field, in addition, the endo- and epi-contours were integrated as prior information to further improve the registration result. The radial strain showed a different pattern for patients and healthy volunteers. In [107], an improved Demons algorithm was used to extract the motion field from 2D images. An additional incompressibility regularization was applied by forcing the Jacobian determinant of the deformation field to be equal to 1.

However, the strain result is strongly influenced by the algorithm used to analyze the data and by the image quality [108]. Robin J. et al. gave a normal value for the myocardium using feature tracking methods [109]. More strain results are summarized in Table 7.

Table 7. Normal value for myocardium from previous study.

	Longitudinal	Radial	Circumferential
Feature tracking, mri cine,2d [109]	-19.1±4.1% (-11.1 to-27.1)%	39.8±8.3% (23.5 to 56.1)%	-18.4±2.9% (-12.7 to -24.1)%
STE,2d [95]	23.4±2.7%	-	-
Global strain, mri cine, 2d [110]	-22.3 % (-20.5 to - 24.0)%	60.5 % (55.3 to 65.6)%	−25.0 % (−24.0 to −26.1)%

Currently, 2D strain is more commonly used in clinical applications compared to 3D strain. 2D radial strain and circumferential strain are usually measured on short-axis images. The radial strain is measured by calculating wall-thickening, and the circumferential strain is approximated by the change in mid-layer myocardium perimeter [111]. Usually, the image with the same slice number is selected to calculate the wall thickening. The longitudinal strain is estimated from long-axis images. However, there are a few drawbacks with 2D images. The most obvious problem is that 2D strain analysis does not consider the inter-slice.

Nowadays, 3D cine images are more and more available and have gained more interest from researchers. In [108], an overview about current 3D strain analysis was given. In

[112], 3D speckle tracking was compared with 2D speckle tracking. For global strain, the 3D strain correlates well with the 2D result (R=0.83 for longitudinal strain and R=0.86 for circumferential strain), but the absolute value is much smaller. For regional strain, the correlation between the 3D and 2D results is poor (R=0.63 for longitudinal strain and R=0.43 for circumferential strain). Tomoyuki et al. also compared 3D strain with 2D strain and investigated the correlation between strain and ejection fraction. The result shows that the 3D and 2D longitudinal strain are not significantly different, while the circumferential strain is significantly different. The result also shows that the principal strain has the strongest correction with ejection fraction (R= -0.93, R=-0.86 for circumferential strain) [113]. Nguyen et al. investigated the correlation between 2D/3D strain and ejection fraction, and the result shows that 3D strain can provide a better estimate of left ventricular function than 2D strain [114].

Table 8. Correlation coefficient between strain and ejection fraction [114].

	Radial strain	Circumferential strain	Longitudinal strain
2D strain[114]	0.709	-0.775	-0.638
3D strain[114]	0.742	-0.862	-0.720

Alessandro et al. (2017) investigated 3D principal strain from 2D cine image stack [115]. In this study, a 3D mesh model of the heart was generated and deformation was estimated using a feature-based optical flow algorithm. The principal strain was calculated at each epi- and endocardial surface point. The 3D principal strain was compared with the 3D STE strain and 2D strain. The result shows good agreement between the different techniques.

5.3 PEAK STRAIN ANALYSIS BASE ON 3D DATA

To obtain the 3D strain, a new workflow was proposed (Figure 23). The 3D volumes at end-diastolic (ED) phase and at end-systolic (ES) phase were taken. Left ventricle segmentation was first performed on each volume, which resulted in a 3D binary mask and a 3D surface model. Then image registration was used to calculate the dense motion fields. Together with the 3D surface model, the motion field was converted to strain at each voxel. Finally the bull's eyes plot was generated for clinical use.

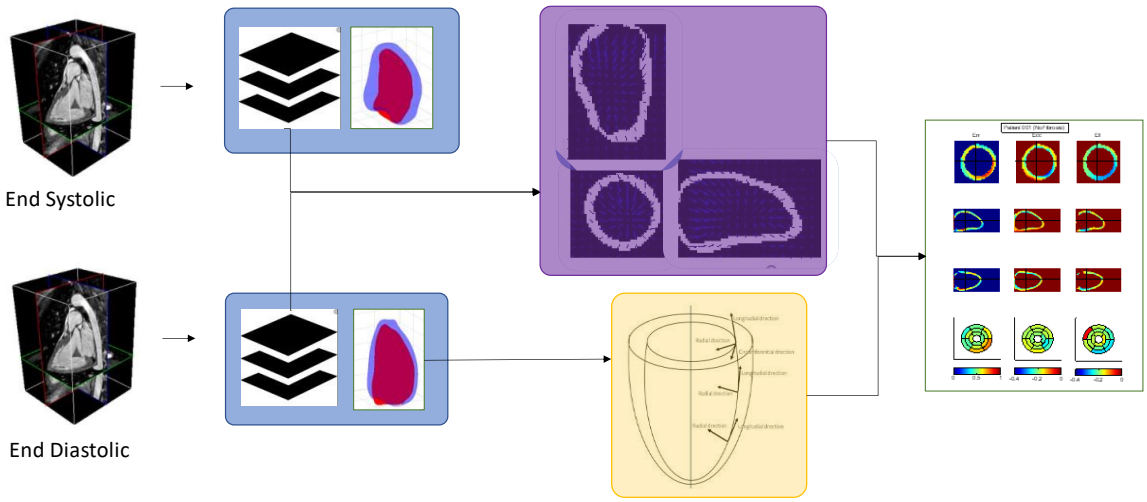

Figure 23. Illustration for 3D strain calcuation workflow

5.3.1 HEART SEGMENTATION AND HEART MODEL CONSTRUCTION

There are two purposes to segment the heart surface: (1) the myocardial mask is subsequently used to extract the motion field. (2) The myocardial surface model is used to determine the local directions, which is then used to generate the longitudinal, radial and circumferential strain.

In the heart surface segmentation, 3-Long axis images are selected, and manual contours were drawn on ED and ES phases. Then the 3D heart model was constructed using the B-spline interpolation algorithm described in [116] [17].

5.3.2 PROPOSED REGISTRATION FOR MOTION FIELD EXTRACTION

The 3D motion field from ED to ES phase was estimated by registering the myocardial masks between ED and ES using a non-rigid registration algorithm. Due to the lack of features for registration, a composite regularization was applied to impose region-wise behavior: outside the myocardium (termed compressible region hereafter), conventional isotropic first-order smoothing is imposed (allowing compressibility, in particular in the blood cavity); inside the myocardium (termed incompressible region hereafter), second-order smoothing is applied, and an incompressibility constraint is added (enforcing $div(u) \approx 0$), as well as a constraint minimizing rotational deformation (enforcing $curl(u) \approx 0$, as local rotational motion causes shearing). As shown hereafter, all these regularization terms involve linear operators, so the calculation of the cost function

gradient is straightforward. Here the binary mask of the myocardial tissue was used instead of the intensity image to improve the accuracy, especially in the case of large motion fields.

Here, the end-diastolic phase was used as the reference phase. The motion field was calculated by minimizing the SSD difference between the reference image and the wrapped image.

$$E = \sum_{x} \|M_{ed}(x+u) - M_{es}(x)\|^2 + \lambda \cdot R$$

Where M_{ed} and M_{es} are the binary masks obtained in ED and ES phase, $\sum_x \|M_{ed}(x+u) - M_{es}(x)\|^2$ measure the similarity between the end-diastolic image and the deformed end-systolic image.

R is the regularization, consist of $\mathrm{R_{compress}}$, $\mathrm{R_{incompress}}$, $\mathrm{R_{div}}$ and $\mathrm{R_{rot}}$.

$$R = R_{compress} + \frac{\lambda_{inc}}{\lambda} R_{incompress} + \frac{\alpha_{div}}{\lambda} \cdot R_{div} + \frac{\alpha_{rot}}{\lambda} R_{rot}$$

The definitions and relevant computations necessary for the optimization (∇R computation) are given below.

- $R_{compress}(u) = \left\| w_{comp} \cdot \nabla u \right\|^2$, with $\nabla R_{compress} = \nabla_x' \cdot w_{comp} \cdot \nabla_x + \nabla_y' \cdot w_{comp} \cdot \nabla_y + \nabla_z' \cdot w_{comp} \cdot \nabla_z$ is the smoothness constraint in compressible area. Here $\nabla = \left[\frac{\partial}{\partial \mathrm{x}} \quad \frac{\partial}{\partial \mathrm{y}} \quad \frac{\partial}{\partial \mathrm{z}}\right]$ and $\mathrm{w_{comp}}$ is the binary mask representing the non-myocardial region.

- $R_{incompress}(u) = \|w_{inc} \cdot \nabla^2 u\|^2$, with $\nabla R_{incompress} = \nabla_x^{2\prime} \cdot w_{inc} \cdot \nabla_x^2 + \nabla_y^{2\prime} \cdot w_{inc} \cdot \nabla_y^2 + \nabla_z^{2\prime} \cdot w_{inc} \cdot \nabla_z^2 + 2\nabla_{xy}{}' \cdot w_{inc} \cdot 2\nabla_{xy} + 2\nabla_{yz}{}' \cdot w_{inc} \cdot 2\nabla_{yz} + 2\nabla_{xz}{}' \cdot w_{inc} \cdot 2\nabla_{xz}$ is the second order smoothing regularization inside the myocardial region and w_{inc} is the binary mask for myocardial region.

- $R_{div}(u) = \|w_{inc} \cdot \nabla \cdot u\|^2 = \|w_{inc} Div(u)\|^2$, with $\nabla R_{div} = Div' \cdot w_{inc} \cdot Div = \begin{bmatrix} \nabla_x' \\ \nabla_y' \\ \nabla_z' \end{bmatrix} \cdot w_{inc} \cdot [\nabla_x \quad \nabla_y \quad \nabla_z]$ where Div=$[\nabla_\mathrm{x} \quad \nabla_\mathrm{y} \quad \nabla_\mathrm{z}]$ is the divergence operator.

- $R_{rot}(u) = \|w_{inc} \cdot \nabla \times u\|^2 = \|w_{inc} \cdot Rot(u)\|^2$, with $\nabla \mathrm{R}_{\mathrm{rot}} = \mathrm{Rot}' \cdot \mathrm{w}_{\mathrm{inc}} \cdot \mathrm{Rot}$ where $\mathrm{Rot} = \begin{bmatrix} 0 & \nabla_z & -\nabla_x \\ -\nabla_z & 0 & \nabla_y \\ \nabla_x & -\nabla_y & 0 \end{bmatrix}$ is the rotational or curl operator.

To solve this function, an iterative method is used and the cost function is linearized in the neighborhood of the current estimate, similar to the optical flow problem in 3.7.7.

$$\sum_{\mathrm{x}} \|\mathrm{M_{ed}}(\mathrm{x}+\mathrm{u}) - \mathrm{M_{es}}(\mathrm{x})\|^2 = \left\|\mathrm{M_{ed,x}u_x} + \mathrm{M_{ed,y}u_y} + \mathrm{M_{ed,z}u_z} + \mathrm{M_{ed}} - \mathrm{M_{es}}\right\|^2$$

Then the cost function to be optimized at each iteration is a linear least squares function of the form $\mathrm{E(u)} = \|\mathrm{Au} - \mathrm{b}\|^2 + \lambda \cdot \mathrm{R(u)}$. This optimization problem can be solved using the conjugate gradient algorithm, with Gauss-Siedel preconditioner. Here

$$\mathrm{A^hA} = \begin{bmatrix} \mathrm{diag(I_x^2)} & \mathrm{diag(I_xI_y)} & \mathrm{diag(I_xI_z)} \\ \mathrm{diag(I_xI_y)} & \mathrm{diag(I_y^2)} & \mathrm{diag(I_yI_z)} \\ \mathrm{diag(I_xI_z)} & \mathrm{diag(I_yI_z)} & \mathrm{diag(I_z^2)} \end{bmatrix} \text{ and } \mathrm{A^hb} = \begin{bmatrix} \mathrm{I_{ed,x}} \cdot (\mathrm{I_{es}(x+u)} - \mathrm{I_{ed}}) \\ \mathrm{I_{ed,y}} \cdot (\mathrm{I_{es}(x+u)} - \mathrm{I_{ed}}) \\ \mathrm{I_{ed,z}} \cdot (\mathrm{I_{es}(x+u)} - \mathrm{I_{ed}}) \end{bmatrix}$$

Deformation u can be obtained by solving

$$(\mathrm{A^hA} + \lambda \cdot \nabla \mathrm{R}) \cdot \mathrm{u} = \mathrm{A^hb} - \lambda \cdot \nabla \mathrm{R} \cdot \mathrm{u_{prev}}$$

5.3.3 STRAIN CALCULATION

5.3.3.1 3D STRAIN CALCULATION

Here the Green-Lagrange strain is used. In the 3D case, if u is the 3D motion field, then strain is defined as a tensor

$$\mathrm{S} = \begin{bmatrix} \varepsilon_x & \varepsilon_{xy} & \varepsilon_{xz} \\ \varepsilon_{xy} & \varepsilon_y & \varepsilon_{yz} \\ \varepsilon_{xz} & \varepsilon_{yz} & \varepsilon_z \end{bmatrix}$$

Where ε_x, ε_y and ε_z are three principal strains and ε_{xy}, ε_{yz} and ε_{xz} are the shear strains.

The relationship between the strain and deformation force F is :

$$\mathrm{S} = \frac{1}{2}(\mathrm{F}' \cdot \mathrm{F} - \mathrm{I}), \text{ where F is the deformation force}$$

$$F = \begin{bmatrix} \frac{\partial u_x}{\partial x} + I & \frac{\partial u_y}{\partial x} & \frac{\partial u_z}{\partial x} \\ \frac{\partial u_x}{\partial y} & \frac{\partial u_y}{\partial y} + I & \frac{\partial u_z}{\partial y} \\ \frac{\partial u_x}{\partial z} & \frac{\partial u_y}{\partial z} & \frac{\partial u_z}{\partial z} + I \end{bmatrix}$$

So that,

$$\varepsilon_x = 0.5(2u_{xx} + u_{xx}^2 + u_{yx}^2 + u_{zx}^2)$$

$$\varepsilon_y = 0.5(2u_{yy} + u_{xy}^2 + u_{yy}^2 + u_{zy}^2)$$

$$\varepsilon_z = 0.5(2u_{zz} + u_{xz}^2 + u_{yz}^2 + u_{zz}^2)$$

$$\varepsilon_{xy} = 0.5(u_{yx} + u_{xy} + u_{xx}u_{xy} + u_{yx}u_{yy} + u_{zx}u_{zy})$$

$$\varepsilon_{xz} = 0.5(u_{zx} + u_{xz} + u_{xx}u_{xz} + u_{yx}u_{yz} + u_{zx}u_{zz})$$

$$\varepsilon_{yz} = 0.5(u_{yz} + u_{zy} + u_{xy}u_{xz} + u_{yy}u_{yz} + u_{zy}u_{zz})$$

In cardiac analysis, the strain tensor is rotated to express deformation values in the longitudinal, circumferential and transmural(radial) directions, which are defined as follows, in Figure 24:

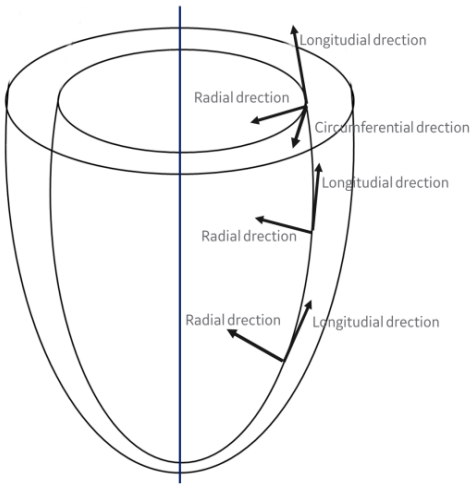

Figure 24. Direction definition for 3D strain calculation

- The radial direction is defined as the normal direction to the endocardial surface;
- the circumferential direction is defined as the cross product between radial direction and z-direction (z being the longitudinal axis of the ventricle).

- The longitudinal direction is defined as the cross product between the circumferential direction and radial direction.

The rotated strain tensor

$$S_{rot} = \begin{bmatrix} e_{radial}{}' \\ e_{circum}{}' \\ e_{longitudial}{}' \end{bmatrix} \cdot S \cdot [e_{radial}, e_{circum}, e_{longitudial}]$$

where $e_{radial}, e_{circum}, e_{longitudial}$ are the normal direction of radial, circumferential and longitudinal direction at each point.

The 16-segment AHA result was calculated according to the definitions in 2.2.7.

5.3.3.2 GLOBAL 2D STRAIN CALCULATION

To validate the proposed calculation scheme, the result was compared with the global 2D strain. The global 2D strain was calculated from the global change in the heart geometry. A left ventricle heart model was constructed from the epi- and endo-cardial contour. The global longitudinal strain GLS was estimated by the shortening in long-axis of the endocardial surface. The global radial strain was estimated as the average wall thickening (WT) on difference slices, and the wall thickness was calculated by find the nearest point on epicardial contour for each endocardial contour. The global circumferential strain was calculated as the average relative perimeter difference on different slices.

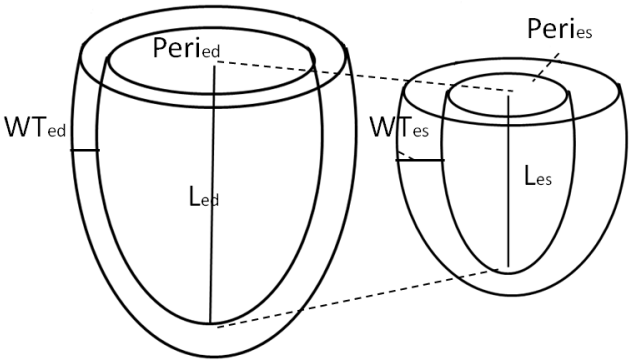

$GLS = (L_{ed} - L_{es})/ L_{ed}$

$GRS = \text{mean}\ (WT_{ed} - WT_{es})/ WT_{ed}$

$GCS = \text{mean}(Peri_{ed} - Peri_{es})/ Peri_{ed}$

Figure 25. Global strain calculation

5.4 STRAIN CURVE ANALYSIS

In this section, we tried to generate the strain curves from the patient data. It is hypothesized that analyzing the 3D deformation curves, extracted from the full dynamic 3D dataset (in this study, 32 cardiac phases for the complete cardiac cycle), can provided more information about regional anomalies than only analyzing the peak strain, which takes only two cardiac phases into account.

The strain curve can be obtained in the same way as described in 5.3 for each cardiac phase. Because only the end-diastolic and end-systolic phases are segmented by the clinical expert, the myocardial mask needs to be obtained in all other phases.

To obtain the myocardium model through the whole cardiac cycle, the manual contours on the ED and ES phases were propagated to the full heart cycle. The initial contour on each phase was estimated as the weighted average of ED and ES contour. w_{ed} and w_{es} are the weighting factor, which is estimated as the correlation coefficient between the image i and ED/ES image

$$C(i, ph) = w_{ed}C(i, ED) + w_{es}C(i, ES)$$

The interpolated contour is used as the initial contour for the phase. Then for each point on the contour, a block of 5x5 patch at ED and ES is used as the feature of the point. And the best matching point along the perpendicular direction of the contour is taken as the final position of the point. Finally, a smoothness of 3 point is applied to remove unreliable points.

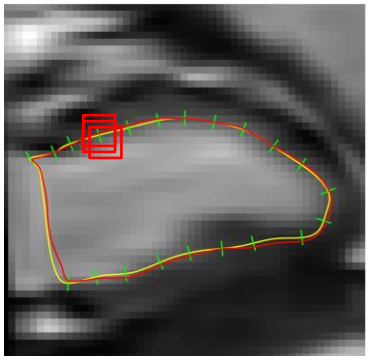

Figure 26. Illustration of block matching. Yellow contour is initial contour; green line is he search direction; red contour is final contour; red rectangles are search window

After segmentation, a 3D surface model is generated using implicit B-spline surface reconstruction described in [116]. The accuracy of the surface reconstruction is validated in [17]. Then the 3D motion field is extracted for each phase by registering the myocardial masks using the region-wise registration with incompressibility and rotational constraints, as described in 5.3.2. Finally, the 3D strain is calculated for each phase as described in 5.3.3.

Chapter 6 Evaluation of optimized T_1 mapping workflow

In this Chapter, the proposed optimization of T_1 mapping workflow in Chapter 4 is evaluated. The result described in this chapter was published in S.Liu et al, "A vectorized Levenberg-Marquardt model fitting algorithm for efficient post-processing of cardiac T_1 mapping MRI" and S.Liu et al, "GPU Implementation of Levenberg-Marquardt Optimization for T_1 Mapping"

6.1 EXPERIMENTS

6.1.1 DATA ACQUISITION

Table 9. Main T1 mapping sequence parameters

Sequence	SMART1Map (Saturation-recovery)	MOLLI (Inversion-recovery)
Number of volunteers	16	12
Flip Angle	45°	45°
Matrix	224x192	160x128
TR	3.95 ms	3.58 ms
TE	1.74 ms	1.56 ms
Readout	bSSFP	bSSFP
Image size	256x256	256x256
Number of images	8	11

16 healthy volunteers were included in the study. For all of them, Saturation Recovery images are acquired using SMART1Map sequence in [26], and for 12 of them, Inversion Recovery images were acquired with MOLLI sequence [21]. In each acquisition, both the pre-contrast and post-contrast (15 min after injection of 0.2 mmol/kg of DOTAREM contrast agent, Guerbet, Villepinte, France) are acquired. The study protocol was approved by the ethics committee and written informed consent was obtained from all volunteers. Image acquisition parameters are listed in Table 9. Saturation times for the SMART1Map sequences were on average: 90, 190, 280, 380, 1370, 2360, 3300 ms + "infinite" time (first image acquired, with no saturation pulse). Inversion times for the MOLLI sequences following a so-called 5(3)3 pattern (1st inversion followed by 5 acquired images, then 3 heart beats of pause, then 2nd inversion followed by 3 images etc…) and were on average: 200, 280, 360, 1220, 1360, 1470, 2340, 2480, 2900, 3340, 4370 ms.

All data were acquired with a General Electric 3T system (Signa HDxt, GE Healthcare, Milwaukee, USA). One short-axis slice was positioned in the mid-cavity and all acquisitions were synchronized to the ECG. Subjects were instructed to hold their breath during the sequence, resulting typically in 8 (SR) to 11 (IR) T1-weighted images being acquired within a breath-hold period. Partial Fourier and parallel imaging (acceleration factor of 2) were used.

6.1.2 VALIDATION OF THE REGISTRATION

To validate the registration result, DICE score for an image series before and after registration was calculated[117]. For a pair of image, the DICE score was calculated using myocardium mask. Here the myocardium mask was generated by manual segmentation of the left ventricular myocardium (i.e. endocardial and epicardial contours) using the software package MASS (Medis, Leiden, the Netherlands). In the manual segmentation, the contours on the image with best contrast were drawn manually and copied to the other images. Correction was made only when necessary. For an image series, the DICE score is defined as the worst DICE score between each image and the reference image:

$\mathrm{DICE} = \min\left(\frac{2\cdot|A_i \cap A_n|}{|A_i|+|A_n|}\right) \ldots i \in \{1: N_t - 1\}$, with A_i the myocardium mask in image i

Note that a DICE score equal to one means the user did not need to edit the copy-pasted contours in an entire series. Differences in DICE scores before/after registration were tested. For statistical significance, a Wilcoxon test is used, with a significance level set to 5%.

Then the effect of registration on T_1 calculation was evaluated using the R^2 error of model fitting, which can be considered as a measurement of the Goodness of the fitting. The R^2 error of the T_1 model fit before and after registration was compared. Here only the standard pixel-wise fitting with 3 parameters fitting model was used. Data from both SR and IR sequences were evaluated and tested for statistical significance. It needs to be mentioned that a mask was defined to select pixels with good fit, as defined by a coefficient of determination $R^2 > 0.97$. This threshold has been proposed in previous

studies on myocardial T_2 mapping as a quality index to exclude outlier pixels/regions from the analysis [85,91].

6.1.3 VALIDATION OF THE T_1 MAPPING WORKFLOW

To evaluate the accuracy and precision of the proposed curve fitting algorithm, simulation experiments were performed first. A numerical phantom made of 6 disk-shaped structures was generated. The T_1 values of those disks ranged from 300ms to 2300ms with a sample interval of 400ms, as shown in Figure 30. Rician noise was added to the image to model the noise observed in actual image acquisition, using the following formula:

$$\mathrm{I}(\mathrm{x},\mathrm{y},\mathrm{t}) = |I_0(x,y,t) + \delta * (randn() + i * randn())|.$$

where $\mathrm{randn}()$ is a normal distribution generator function and δ is the noise level.

The accuracy of T_1 value was measured as the absolute difference between the estimated T_1 value and the ground truth. The precision of the T_1 value was measured by the standard deviation in the disk-shaped region. The effect of the regularization is evaluated by changing the regularization strength μ. It needs to been mentioned that, to evaluate the effect of the regularization, a mask smaller than the original disk-shaped structure was used to exclude boundary artifacts when measuring the mean T_1 value and standard deviation of each region.

Then the proposed model fitting algorithm was validated on volunteer data (describe in 6.1.1). Image registration was performed before curve fitting for all the volunteer data.

The proposed vectorized model fitting was firstly compared against the standard pixel-wise fitting. Both 3-parameter and 2-parameter models were evaluated with data from SR and IR sequences. Resulting model fits were compared in terms of: (i) agreement in T_1 values, as assessed by median differences and 95% confidence intervals; (ii) computational efficiency, as assessed by computation time and number of iterations.

Then the denoising/spatial smoothing ability of the proposed method was tested on the volunteer database by applying the vectorized LM fit with different values of the spatial regularization weight μ.

Finally the impact of the initialization was assessed by comparing the default and the proposed region-based initialization schemes. Detailed description can be found in section 4.3.2. Here, only MOLLI data with 3-parameters model was evaluated as premature stop in local minimum is more often observed in IR sequence. Differences were assessed qualitatively and quantitatively by comparing the differences in T_1 values, and more particularly those in the blood pool, where convergence to local minima appears more often.

All the validation experiments were performed with Matlab 2015a (Mathworks, Natick, USA) running on a computer with Intel® Core™ i5 CPU , 8GB memory (Intel, Santa Clara, USA). Statistical significance was tested using a Wilcoxon signed rank test, with significance level set to 5%.

6.1.4 VALIDATION OF GPU IMPLEMENTATION

To validate the GPU implementation, the images acquired in section 6.1.1 were used. All experiments were performed on computer with Intel® Xeon CPU at 3.30GHz, 64G physical memory. The graphic card is NVIDIA Quadro K4200, with 1344 cores, operating at 784MHz, a 256-bit memory interface, and a 4GB GDDR5 GPU memory with memory bandwidth of 173 GB/s

For pixel-wise curve fitting, the standard sequential c code and the CUDA code were both compiled as a “mex” file to be interfaced with Matlab (Mathworks, Natick, USA) and the C code is used as a reference for the GPU implementation.

For the vectorized curve fitting, the following 3 implementations were compared:

- Initial experiments in Matlab: the Matlab implementation was used as reference because the linear solver in Matlab is highly optimized.
- GPU implementation in Matlab: this was enabled by replacing the array variables by gpuArray ones in Matlab.
- Full CUDA implementation.

6.2 RESULTS

6.2.1 REGISTRATION

The DICE score before and after registration for all the acquisition was measured and the statistic results are reported in Table 10. The results show that the DICE scores are improved for both SMART1Map and MOLLI series. The improvement is statistically significant ($p<0.05$) for all SMART1map (pre- and post- contrast) and for pre-contrast MOLLI. However, the improvement was more pronounced in SMART1Map images than in MOLLI images.

Table 10. Dice scores computed from the myocardial contours before and after registration

		Before registration	After registration	p-value
SMART1map	Pre-contrast	0.8225±0.1438	0.9784± 0.0320	1.2207e-04
	Post-contrast	0.7609± 0.1568	0.9192± 0.0874	1.2207e-04
MOLLI	Pre-contrast	0.8323± 0.0989	0.8977± 0.0623	0.0093
	Post-contrast	0.8364± 0.0985	0.8762± 0.1381	0.3013

The DICE scores for SMART1Map and MOLLI series are plotted in Figure 27. There is one case with post-contrast MOLLI that images registration failed and result in a large decrease of the DICE score, as can be seen in Figure 27 (right). Further investigation showed this failure is caused by the significant contrast change, which was incorrectly corrected during the histogram matching

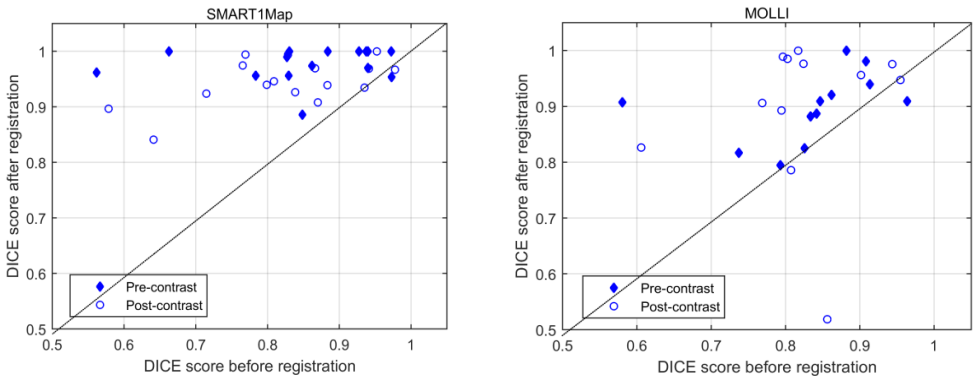

Figure 27. Dice scores before and after registration for (Left) SMART1Map and (Right) MOLLI

The goodness (R^2) values for the T_1 model fits obtained in the myocardium before and after registration are described in Table 11. R^2 was improved for both SMART1Map and MOLLI series and this improvement was statistically significant ($p<0.05$) except in the pre-contrast MOLLI data.

Table 11. R^2 values showing the goodness of the T_1 fitting in the myocardium before and after registration

		Before registration	After registration	p-value
SMART1Map	Pre-contrast	0.9858±0.0076	0.9889± 0.0072	0.0052
	Post-contrast	0.9751± 0.0210	0.9824± 0.0182	4.3778e-04
MOLLI	Pre-contrast	0.9192±0.0402	0.9258± 0.0345	0.3804
	Post-contrast	0.9723± 0.0124	0.9793± 0.0088	0.0068

6.2.2 REGION –BASED INITIALIZATION

Figure 28 demonstrates intermediate results of the fitting using region-based initialization in an example dataset, including the raw image, the segmentation, the initial T_1 for each region and the final T_1 mapping.

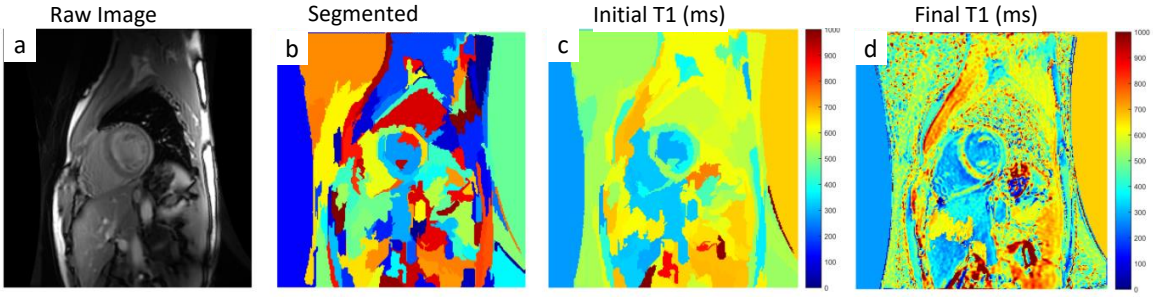

Figure 28. Illustration of the region-based initialization: (a) mean image from the T_1 series (MOLLI); (b) label image from the segmentation; (c) initial T_1 value from each region; (d) final T_1 value obtained with the region-based initialization ($\boldsymbol{\mu = 1e-6}$).

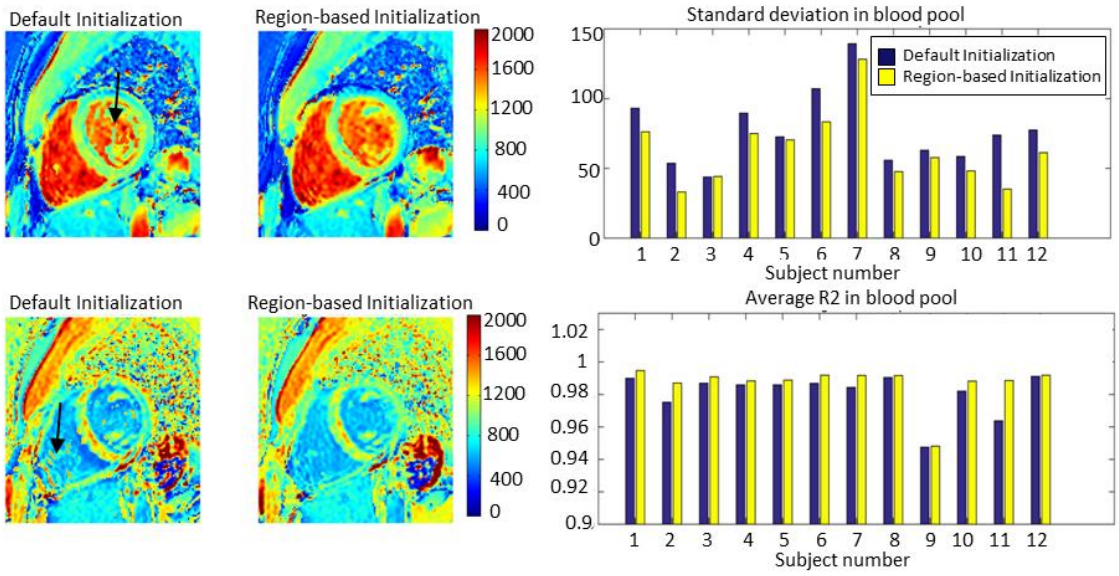

Figure 29. (left) Example T1 maps obtained using default initialization and region-based initialization: pre-contrast image (top), post-contrast image (bottom). Black arrow indicates the wrong curve fitting pixels. (right) Standard deviation of T1 values and average R2 in the blood pool for each subject of our population.

Figure 29 (left) shows an example comparison between default and region-based initialization in pre- and post-contrast MOLLI images. The region-based initialization shows smoother T_1 values in the blood pool. With the default initialization, there is a larger variability of T_1 values in the blood pool region. In the pre-contrast image, a number of pixels from the blood region have values close to the default initial guess of $T_1 = 1000\ \mathrm{ms}$, suggesting incorrect convergence. Then the difference of the region-based

initialization and default initialization was quantified by the standard deviation and the average R^2 in the left ventricle blood pool (Figure 29 Right). The standard deviation decreased from 77.3±26.8 ms to 63.4±26.2 ms (p=9.8e-4) and the average R^2 increased from 0.981±0.013 to 0.987±0.012 (p = 4.9e-4).

6.2.3 Model Fitting validation with simulation

Figure 30 shows the simulation result for saturation recovery using 3 parameter curve fitting. Compared to the pixel-wise curve fitting, the vectorized curve fitting shows less noise. A smoothing effect was observe. As the spatial regularization increases, the smoothing effect gets stronger. This indicate that the vectorized algorithm is more resistant to noise, however, the edges are also blurred. Similar trend was found for inversion recovery. It can also be noted that in the background noise area, where T_1 is undefined, the regularization tends to set the pixels to the initial guess (1000 ms) instead large arbitrary values, which is observed in pixel-wise curve fitting.

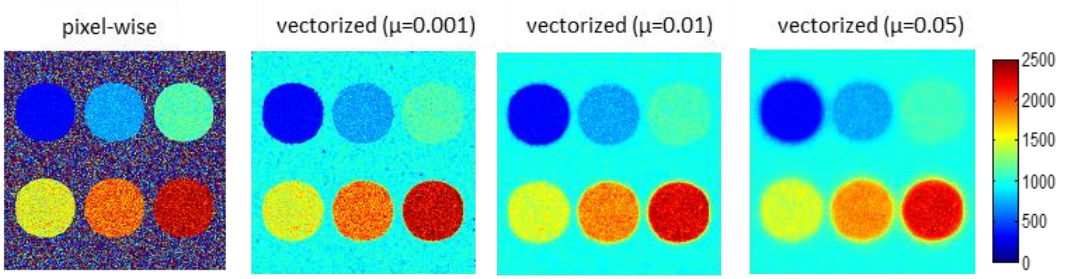

Figure 30. Simulation results for saturation recovery model fitting with different weights of spatial regularization.

To thoroughly quantify the effect of regularization, we measured the average T_1 value with different strengths of spatial regularization, and the result was compared to pixel-wised curve fitting. The statistics of T_1 values for both saturation recovery and inversion recovery, 3 parameter curve fitting and 2 parameter curve fitting are shown in Figure 31(col 1). As the spatial regularization increased, the standard deviation of the estimated T_1 value decreased, which indicate an improved precision of T_1 estimation. However, as the regularization increased, the measured T_1 value deviated from the true T_1 values.

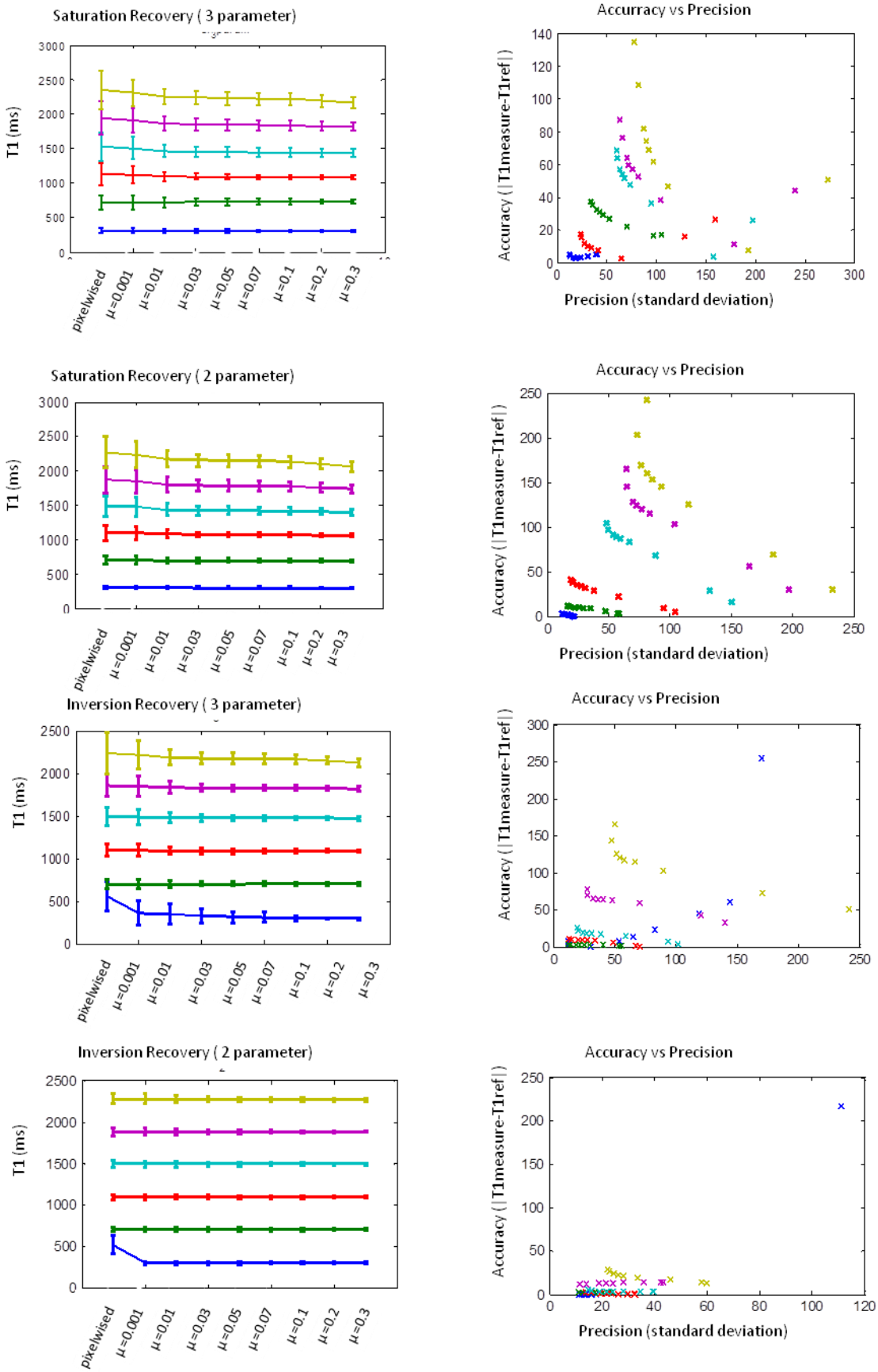

Figure 31. Statistic result for different spatial regularization. (Col 1) Average T_1 value as spatial regularization increased; (Col 2) relationship between accuracy and precision as spatial regularization varies

It needs to be mentioned that, for inversion recovery data, when the T1 value is small (300ms), the pixel-wise curve fitting result is significantly larger than vectorized curve fitting result. This is caused by the premature stop at local minimum, which results in a final value more closed to initial guess (1000ms). With regularization, the measured T1 value can reach global minimum and more close to true value. Figure 31 (col 2) shows the relationship between precision and accuracy as the spatial regularization varies. The shape of these curves is as expected: for each T1 value, as the spatial regularization increases, the precision improves, however, the accuracy gets worse. The point closest to [0 0] corresponds to the optimum regularization. This value is different for different T1 values, however, generally fall in the range [0.001, 0.01].

We further looked at the convergence properties of the optimization. Figure 32 shows the residual as a function of iteration number. The curves generally show quick decline before the 10 iteration. The final residue varies under different regularization, however, in most case $\mu > 0.1$ shows much larger residue, and μ in the range of [0.001, 0.1] gives loser residue, this is consistent with the observation before .

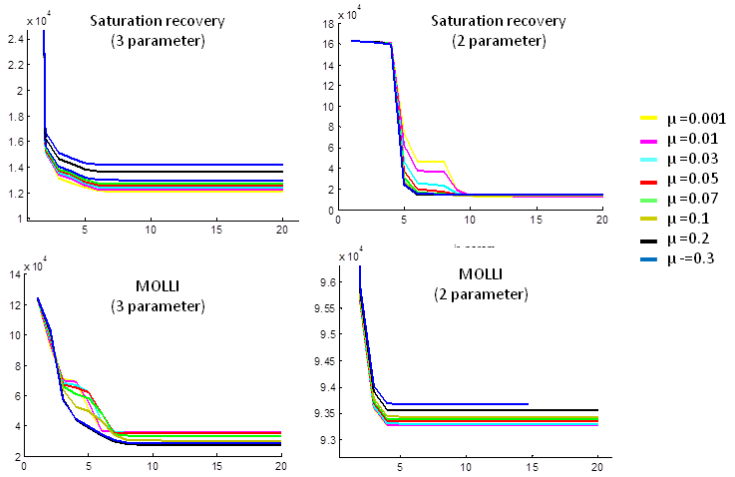

Figure 32. Residual of the T_1 model fitting as a function of Levenberg-Marquardt iterations.

6.2.4 VECTORIZED CURVE FITTING ON PATIENT DATA

In this section, the vectorized curve fitting is validated on clinical data. Pixel-wise curve fitting was used as reference. Figure 33 shows T_1 values obtained from pixel-wise and vectorized model fitting. The pixels in the myocardium and blood pool were compared. Both SMART1Map and MOLLI series were included. For each series, the 3-parameter and

2-parameter models were validated. Most the pixels are along the diagonal line, which indicate good agreement between pixel-wise and vectorized model fitting.

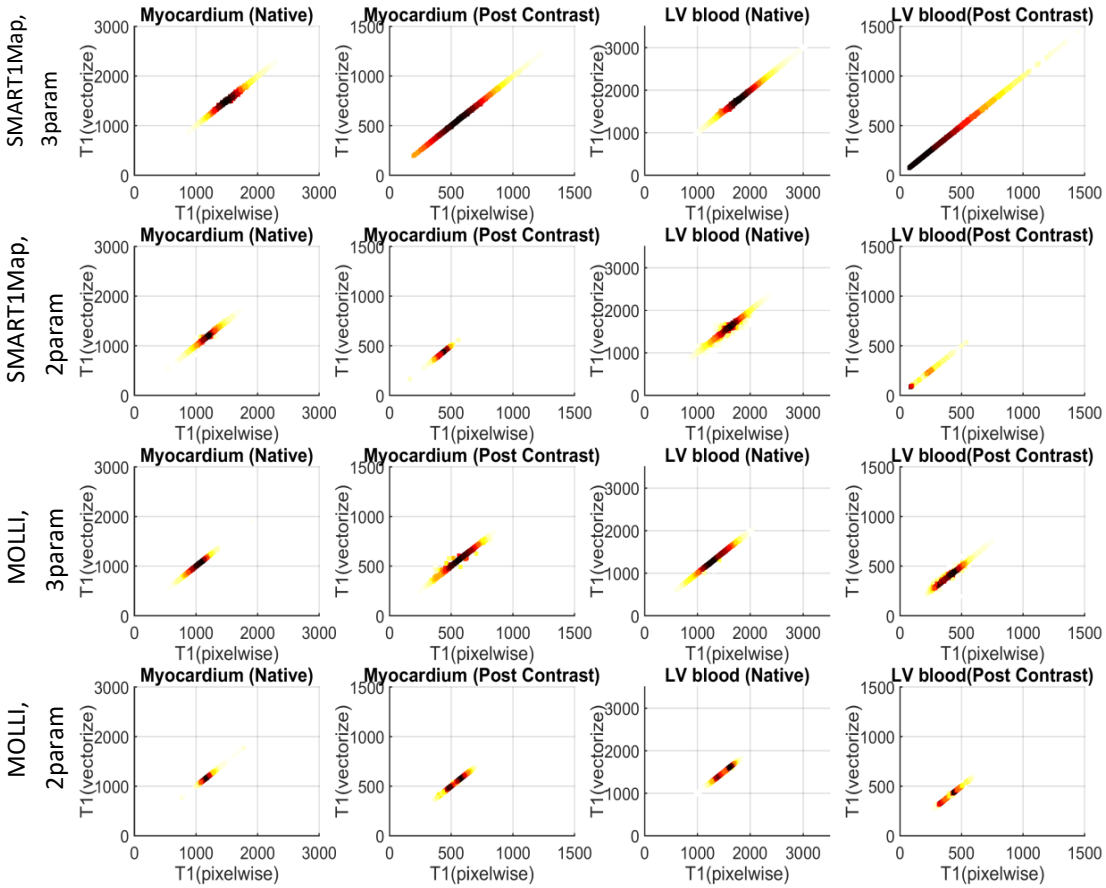

Figure 33. T1 values estimated using the proposed vectorized model fitting versus conventional pixel-wise fitting ; The color shows the density of the point cloud, with black meaning higher density and white meaning lower density: SMART1Map 3-parameter (1st row); SMART1Map, 2-parameter (2nd row); MOLLI, 3-parameter (3rd row); MOLLI, 2-parameter (4th row).

To quantify the difference, the median of the differences in T_1 values and the 95% confidence intervals between vectorized and pixel-wise fitting are reported in Table 12. The vectorized curve fitting was calculated with very small spatial regularization (μ=1e-6). The median values of ΔT_1 are around 0 and the 95% confidence interval of ΔT_1 is smaller than 30ms for both myocardium and blood pool.

Table 13 gives the statistics of the T_1 values in the myocardium and in the blood pool for different sequences and number of parameters using our vectorized model fitting method(μ=1e-6). It needs to be mentioned that the standard deviation is generally higher, because the standard deviations were calculated from all the pixels of the whole

patient database. Table 13 and Table 14 summarize the T_1 values with different spatial regularization. Table 14 gives the T_1 values (mean and standard deviation) computed from the whole database in myocardium and blood pool using increasing μ (=0.005). Minor changes are observed for IR sequences, however the standard deviation is significantly reduced for SR sequences compared to result in Table 13 , which are more susceptible to noise.

Table 12. Agreement between T1 values obtained by conventional pixel-wise LM fit and by the proposed vectorized LM fit (expressed as median difference in ms units, with 95% confidence intervals)

	All pixels (pre-contrast)	All pixels (post-contrast)	Myocardium (pre-contrast)	Myocardium (post-contrast)	Blood (pre-contrast)	Blood (post-contrast)
SMART1Map, (3-param)	-0.1 [-28.2, 15.4]	-0.0 [-22.0, 8.1]	0.7 [-11.9, 13.1]	-0.1 [-4.6, 2.1]	-0.6 [-10.9, 7.8]	0.1 [-1.6, 1.2]
SMART1Map, (2-param)	-0.1 [-34.1, 19.5]	-0.0 [-5.4, 5.9]	0.2 [-12.4, 27.2]	-0.1 [-0.36, 0.2]	-0.2 [-20.3,15.2]	-0.0 [-0.3, 0.1]
MOLLI, (3-param)	-0.0 [-21.8, 10.6]	0.0 [-7.2, 6.4]	0.2 [-3.6, 3.3]	-0.1 [-2.7, 2.2]	-0.3 [-6.8, 2.7]	0.1 [-1.0, 1.9]
MOLLI, (2-param)	-0.0 [-0.5, 0.8]	-0.0 [-0.2, 0.3]	0.1 [-0.5, 0.7]	-0.0 [-0.2, 0.2]	-0.1 [-0.5, 0.5]	-0.0 [-0.1, 0.1]

Table 13. T1 value in myocardium and blood pool with different sequence and number of parameters (μ=1e-6).

	Pre-contrast myocardial T_1 (ms)	Post-contrast myocardial T_1 (ms)	Pre-contrast Blood T_1 (ms)	Post-contrast Blood T_1 (ms)
SMART,3T,3param	1525±246	597±180	1845±330	390±225
SMART,3T,2param	1179±173	423±53	1589±261	265±108
MOLLI,3T,3param	1029±165	563±110	1310±253	407±94
MOLLI,3T,2param	1189±122	536±70	1489±146	416±71

Table 14. T_1 value in myocardium and blood pool with different sequence and number of parameters (μ=0.005)

	Pre-contrast myocardial	Post-contrast myocardial	Pre-contrast blood	Post-contrast blood
SMART,3T,3param	1546±133	579±122	1816±232	378±127
SMARt,3T,2param	1186±157	421±52	1573±237	263±107
MOLLI,3T,3param	1017±148	561±105	1297±249	408±90
MOLLI,2T,2param	1179±101	536±70	1488±146	416±71

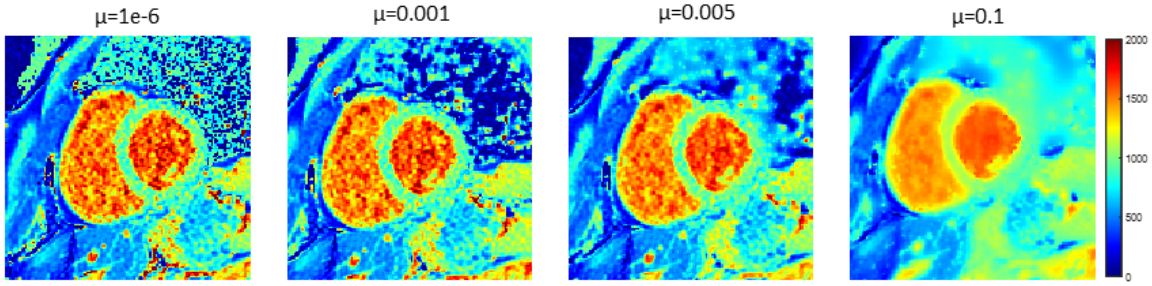

Figure 34. Example T1 map generated with the vectorized LM fitting algorithm using different weights for the spatial regularization

To give a better impression about the effect of vectorized LM fitting and spatial regularization on real data, an example is shown in Figure 34 . When increasing the spatial regularization weight μ, the T_1 map shows a reduced noise level and spatially smoother T_1 values.

6.2.5 GPU IMPLEMENTATION PERFORMANCE

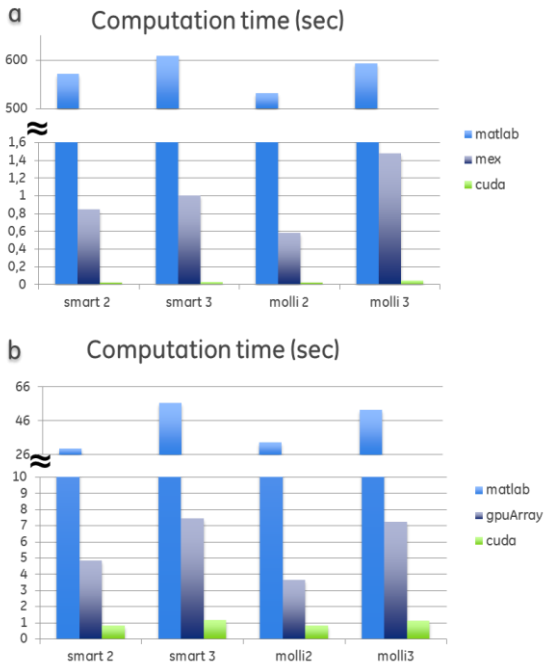

Figure 35. Computation time for T1 mapping (256x256). (a) pixelwised curve fitting; (b) vectroized curve fitting

For the pixel-wise curve fitting, we compared the Matlab code, C code (mex file) and the GPU implementation. For a 256x256 T_1 series, Matlab implementation took approximately 10min to calculate one T_1 map. However, Matlab is well known for its inefficient at for-loop, and It is unfair to compare the Matlab implementation. Therefore, the Matlab mex file was used as a reference. Figure 35(a) shows the computation time of each implementation. The average calculation time using standard C implementation is 0.73±0.16 sec for 2 parameter fitting and 1.21±0.36 sec for 3 parameter curve fitting. The CUDA implementation costs 0.022±0.005 sec and 0.038±0.009 sec for 2- and 3-parameter respectively. The acceleration factor for calculation time is 32 and 31.

For the vectorized curve fitting, the original Matlab implementation costed around 54.39±2.74 sec (3-parameter) and 31.74±4.4 sec (2-parameter) to generate one T_1 map. After replacing the array variables with gpuArray ones, which enables Matlab to calculate

with GPU, the calculation time was reduced to 7.3±0.1 sec (3-parameter) and 4.2±0.7 sec (2-parameter). CUDA implementation further reduces the calculation time to 1.14±0.01 sec (3-parameter) and 0.84±0.02 sec (2-parameter). The acceleration ratio compared to the original Matlab implementation is 47 for 3 parameter case and 38 for 2 parameter case.

Figure 36 further decomposed the computation time of the kernel functions in the vectorized Levenberg-Marquardt algorithm. The figure shows that the filling of $J^T J$ only takes a small amount of time. Most time was spent on the solving of the linear equation.

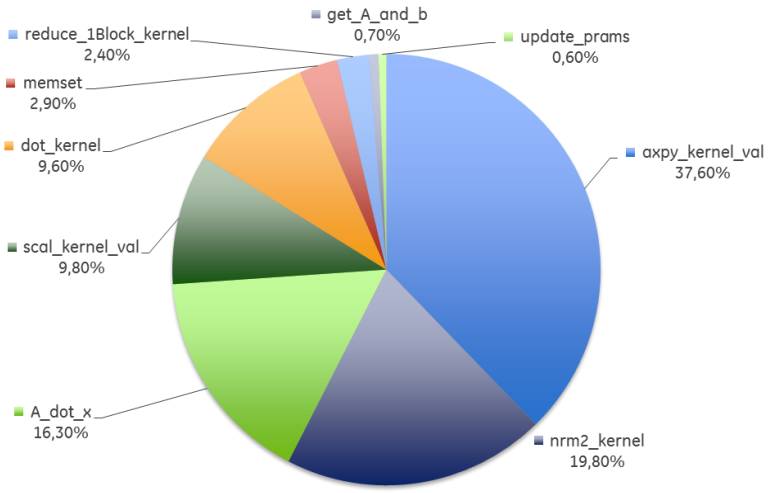

Figure 36. Computation time of kernel functions

6.3 DISCUSSION

In this section, we tried to optimize the T1 mapping workflow by:

- Vectorized curve fitting algorithm
- Region-based initialization
- Non-rigid registration before curve fitting
- GPU computation

The main innovation here is the vectorized curve fitting algorithm, which allows to solve multiple T_1 curve fitting problems simultaneously and allow spatial regularization. In order to evaluate this algorithm we firstly performed simulation experiments for both saturation recovery and inversion recovery sequences. With increased spatial

regularization, better precision was achieved, however, at the cost of reduced spatial resolution. The simulation results show that there is a bias as the spatial regularization increases. This bias effect is more obvious for the saturation-recovery model, while for the inversion-recovery model, the bias is negligible (Figure 31). For saturation-recovery with 3-parameter curve fitting, although the optimal value of the spatial regularization parameter μ varies, the bias remains below 5% when μ is smaller than 0.1. For saturation recovery sequence with 2-parameter curve fitting, the bias is larger, this is also because there is bias introduced by non-central noise and 2-parameter curve fitting cannot compensate for it. It needs to be mentioned that the choice of μ also depends on the intensity of the image signal. In practice, we found that the curve fitting result is not very sensitive, μ between 0.001 and 0.01 providing a good compromise between bias (i.e. accuracy) and variability/uncertainty of the estimate (i.e. precision). In addition, the vectorized curve fitting could be extended to more advanced regularizations, e.g. total variation [118] or other edge-preserving constraints [119]. Future work will focus on the use of such regularizations directly.

Then we validated the algorithm with volunteer data by comparing the proposed vectorized method with the pixel-wise method. The results show that the two methods are in good agreement when mild spatial regularization is applied (Figure 33). The precision of evaluation is measured by the standard deviation. In general, the 2-parameter model fitting results in smaller standard deviations than the 3-parameter model fitting, which is consistent with the previous study that 2-parameter model fitting is more stable. The MOLLI data result in smaller standard deviations than the SMART1Map data, which indicates higher precision. This is caused by the fact that the dynamic range of the IR recovery curve is twice larger compared to the SR recovery curve. T_1 values obtained by SR are higher than those obtained with IR because the saturation recovery acquisition overestimate the T_1 mapping. This trend is in agreement with previous studies [71] for 1.5T.

We have demonstrated the benefit of using our vectorized model fitting method in terms of computation time. Implementing the vectorized algorithm is challenging due to the increased computational complexity (added spatial regularization) and could result a larger computation time. However this is counter-balanced by the use of the conjugate

gradient solvers that can solve the larger sparse matrix inversion at each LM iteration with minimal extra-computation cost. A commonly used strategy to reduce the curve fitting time is to calculate only on the pixels within a pre-computed mask which would further speed-up the computation time. In the context of cardiac T_1 mapping, the mask could be defined as region with enough intensity or only heart region. Both the pixel-wise and the vectorized LM algorithms would benefit from such a strategy. In that case our vectorized LM would be applied to the vector of pixels in the mask of interest instead of the whole image. The computation time in the vectorized LM is dominated by the calculation and the application of the Jacobian matrices (sparse matrix-vector multiplications) and element-wise vector operations within the conjugate gradient solver. Therefore the computation time scales linearly with the number of unknown pixels, both for the pixel-wise and for the vectorized LM.

Another improvement is to use region-based initialization. In the default initialization, 1000ms is used as an initial value for T_1. However, nonlinear optimization is sensitive to initialization and the optimization sometimes stopped at a local minimum. In our experience with myocardial T_1 mapping, pixels in the blood pool are more often affected when a 3-parameter model is used, because the LM algorithm more likely to be trapped in a local minimum. The T_1 value in blood pool is also important because in extra-cellular volume (ECV) calculation, the T_1 value in the blood pool is used as a reference. This happens more often in post-contrast images than pre-contrast images, where T_1 is farther away from this initial value. To optimize the initialization of the nonlinear model fit, a region-based initialization has been proposed. This initialization was found to be more important for MOLLI data, which tends to stop at an inappropriate local minimum when the initialization is not properly set. For SMART1Map, the curve fitting was found to be less sensitive to the initialization, thus the default initialization can also be used.

Besides regularization, other classic extensions of the LM technique can easily be integrated to the proposed framework, e.g. to include robustness to outliers using additional weighting matrices. Furthermore the proposed vectorization strategy is not restricted to LM and could be applied to other nonlinear solvers. The iterative restoration of the signal polarity [75] and phase-sensitive reconstruction [76] could be implemented as a preprocessing step and might improve the result of the vectorized LM fitting further.

Other parameter mapping applications might also benefit from the proposed strategy, including T_2, T_2* mapping and pharmacokinetic model fitting in delayed contrast-enhanced MRI.

6.4 SOFTWARE

Finally, a workflow based software was developed for clinical use. The software allows the user to create a T_1 mapping workflow, with optional steps of image registration, denoising and curve fitting. The design and user interface is shown in Appendix I.

Chapter 7 Evaluation of strain analysis based on 3D cine images

In this chapter, the stain analysis framework proposed in Chapter 5 is evaluated and the results are presented. The binary myocardial mask was used as input for the motion field estimation. The dense motion field was then used to calculate the 3D strain for each point in the myocardial region. Simulation was performed to validate the strain calculation framework. For clinical data, 2D strain was also calculated and used as reference for 3D strain. The strain between patients with and without fibrosis are subsequently compared. Finally, the strain curve for different groups was calculated and compared.

7.1 Experiments

7.1.1 Data Acquisition

18 patients with Duchenne muscular dystrophy were included in this study. The patient population included children and young adults (age = 12.9 ± 4.3 year old, ranging from 6 to 20 years old). The heart rate was 102 ± 18 bpm. The protocol was approved by an ethics committee (clinical study ID C13-04) and written consent was obtained from all patients (and/or their parents when applicable).

Cardiac MRI was performed on a 1.5 T Signa HDxt MR scanner (General Electric, Milwaukee, USA). A conventional imaging protocol, comprising of cine image sequence and tissue characterization sequences, was adapted to these patients to allow the entire examination to be performed under free breathing conditions. This was necessary because these patients were poor breath-holders: the older ones had severe muscular impairment affecting their breathing function in particular, while the younger ones were poorly compliant. Post-contrast cine images were also acquired 2-5 minutes after gadolinium injection. LGE images and T_1 maps were acquired 15 min after injection. These sequences were used to determine myocardial segments whether fibrosis presented (or not) for each patient. Images used for this study included 2D cine stacks covering the left ventricle in three different orientations: short-axis (SAX) stack, horizontal long-axis (HLAX) stack and vertical long-axis (VLAX) stack. The acquisition time for acquiring the 3 cine

stacks was approximately 10 min (SAX stack: 4 min; HLAX stack: 3 min; VLAX stack: 3 min). The image reconstruction comprised a motion correction technique (cine-GRICS) for each 2D cine image stack and a super-resolution technique combining the three stacks into an isotropic 3D cine dataset (1.4 x 1.4 x 1.4 mm^3), as described in [17].

An experience pediatric cardiologist manually drew the contours of endo- and epi-cardial surface on ED and ES images. He also reviewed all LGE, post-contrast T_1 maps and post-contrast cine images to report whether fibrosis was visible and which segment was affected (when applicable), see Table 15 below.

Table 15. Description of patient data.

Patient ID	Age	FE %	Anomaly contraction segments	LGE segments	Pathology
2008-003 01-0001	12	58	N / A	N / A	Duchenne
2008-003 01-0002	10	54	N / A	11 but poor quality	Duchenne
2008-003 01-0004	6	45	diffuse hypokinesia	5,6,11,12,16	Duchenne
2008-003 01-0005	18	52	N / A	11	Duchenne
2008-003 01-0006	16	52	N / A	5.11	Duchenne
2008-003 01-0007	13	54	N / A	5.11	Duchenne
2008-003 01-0008	9	65	N / A	N / A but poor quality	Severe Becker
2008-003 01-0009	20	54	N / A	8	Duchenne
2008-003 01-0010	8	72	N / A	N / A but poor quality	Duchenne
2008-003 01-0011	11	57	N / A	N / A but poor quality	Duchenne
2008-003 01-0014	8	69	N / A	N / A	Duchenne
2008-003 01-0015	11	69	N / A	N / A	Duchenne
2008-003 01-0016	6	66	N / A	N / A	Duchenne
2008-003 01-0017	15	41	N / A	5.11	Duchenne
2008-003 01-0018	20	36	diffuse hypokinesia, apical predominance	5,6,11,12	Duchenne
2008-003 01-0019	18	56	N / A	5,6,11	Duchenne
2008-003 01-0021	9	64	N / A	N / A	Duchenne
2008-003 01-0022	12	57	N / A	5,6,11,12	Duchenne

7.1.2 VALIDATION ON SIMULATION DATA

To validate the registration algorithm and the strain estimation, the left ventricle was modeled as a concentric sphere model (Figure 37). The inner sphere represent the blood pool, and its diameter is 45mm. The space between the two concentric sphere represent the myocardium, where the wall thickness is 10mm. This model was used as ED phase, which is used as reference for registration and strain calculation. The ES phase heart model was generated by resizing the left ventricle model in ED phase. In order to simulate the dynamic motion of the left ventricle, the resizing was done in such a way that the ejection fraction of the left ventricle was 0.7 (which includes the volume of the blood cavity) and the volume of the myocardial region was preserved. The left ventricle model was generated as binary image in a stack of 100x100x80.

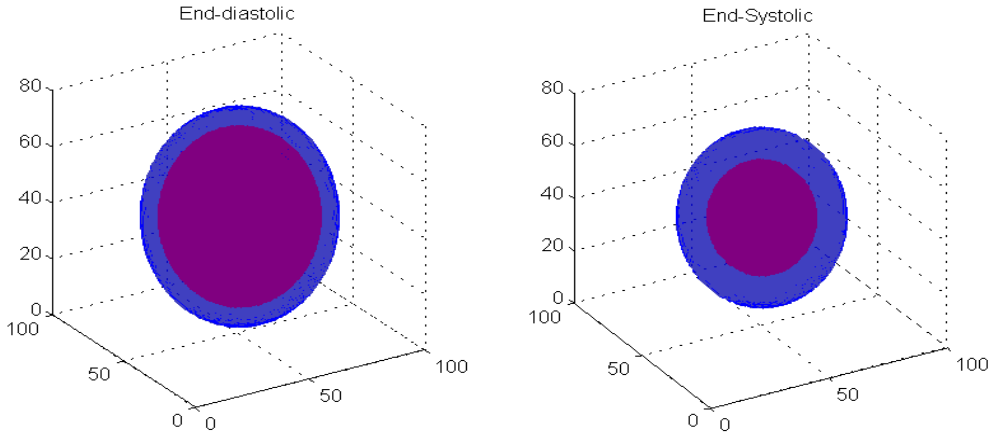

Figure 37. Simulation LV model (a) ED phase (b) ES phase

The dense motion field was firstly calculated using the registration scheme described in 5.3.2. Then the 3D strain was calculated from the motion field, for each voxel in the myocardial mask. For statistic purpose, the average 3D strain was calculated on radial, circumferential and longitudinal directions. Then the myocardial area was further divided into epi- and endo- areas, in which the average strain value was also calculated separately. For comparison purpose, the theoretical strain from the geometry change was calculated, in the same way as the global 2D strain was computed, as described in 5.3.3.

To further validate the consistency of the extracted strain measures, the quantity $(1+\frac{\Delta R}{R})(1+\frac{\Delta C}{C})(1+\frac{\Delta L}{L})$ was checked. This value should be approximately equal to 1 [120]. Because the heart muscle is incompressible, the three-principal strains must satisfy $\varepsilon_x +$

$\varepsilon_y + \varepsilon_z = 1$. For a 3-D patch, if the initial radial, longitudinal and circumferential lengths of the patch are R, L and C, respectively, and the initial volume of the patch is

$$V_0 = RLC.$$

After contraction, the radial, longitudinal and circumferential length become $R + \Delta R$, $L + \Delta L$ and $C + \Delta C$, then the volume is

$$V = (R + \Delta R)(L + \Delta L)(C + \Delta C).$$

Because of the incompressibility of the myocardial tissue,

$$V = V_0$$

So that

$$(R + \Delta R)(L + \Delta L)(C + \Delta C) = RLC$$

Thus

$$(1 + \frac{\Delta R}{R})(1 + \frac{\Delta C}{C})(1 + \frac{\Delta L}{L}) = 1$$

Note that, if we further expand both sides of the equation:

$$\varepsilon_r + \varepsilon_l + \varepsilon_c + \varepsilon_r\varepsilon_l + \varepsilon_r\varepsilon_c + \varepsilon_c\varepsilon_l = 0$$

Ignoring the second order product, then $\varepsilon_r + \varepsilon_l + \varepsilon_c \approx 0$

Here we define the quality check as

$$QualityCheck = (1 + \frac{\Delta R}{R})(1 + \frac{\Delta C}{C})(1 + \frac{\Delta L}{L})$$

7.1.3 VALIDATION ON CLINICAL DATA

For the clinical data, the same processing was performed as for simulation data. The motion field was extracted using the algorithm described in 5.3.2 and 3D strain is estimated using the dense motion field. The 3D peak strain is first compared to the 2D

strain as defined in Figure 25. Then patients are divided as two groups, with fibrosis in segment 11 and without fibrosis in segment 11, the 16-segment result of 3D strains are analyzed. Finally, strain curves for whole cardiac cycle were calculated, and comparison between the two groups was performed.

7.2 RESULTS

7.2.1 SIMULATION RESULT

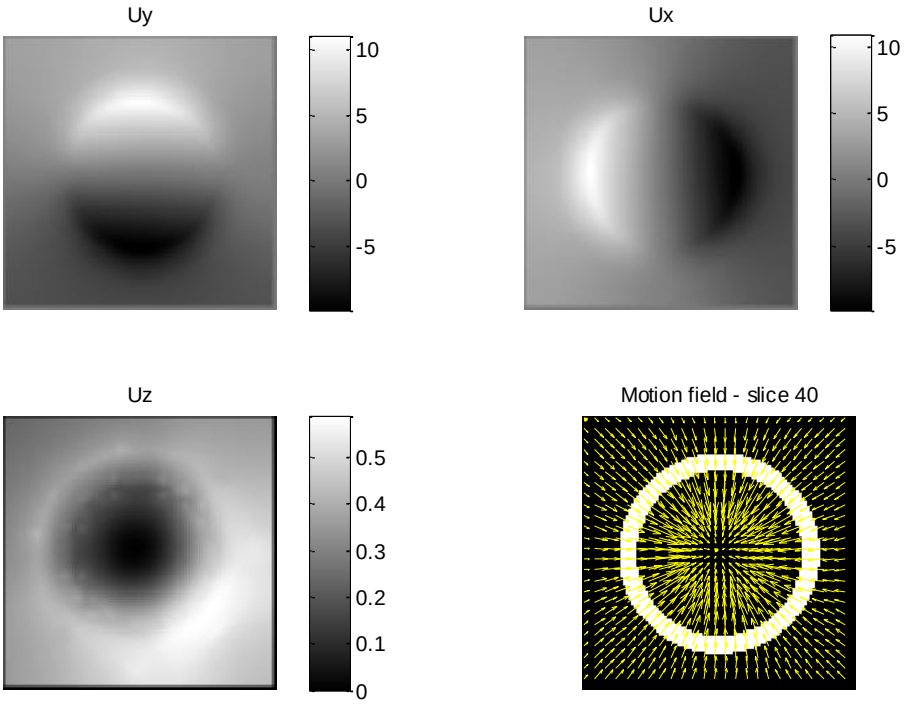

Figure 38. Motion field of simulated heart model (slice 40)

Figure 38 shows a slice of the 3D motion field extracted from the myocardial mask using the incompressibility regulated the registration described in 5.3.2. Compared to the motion field without regularization, the motion field is smoother and more consistent.

Figure 39 shows the estimated strain from the motion field in 3 different slices. In general, the endocardial surface shows larger stain than the epicardial surface, which is consistent with the LV contraction model, that the endocardial surface has larger motion than the epicardial surface.

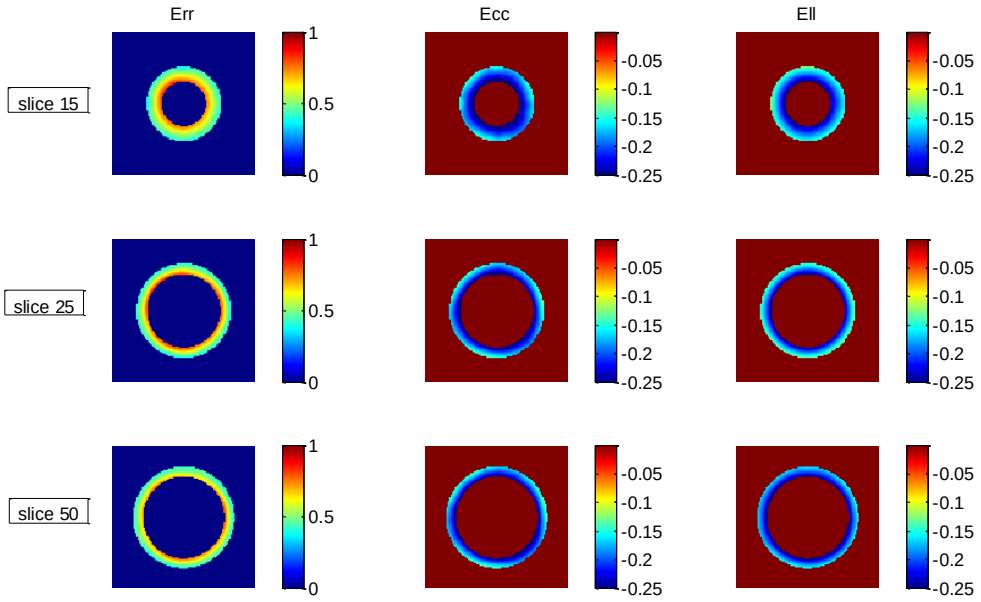

Figure 39. Estimated strain from motion field

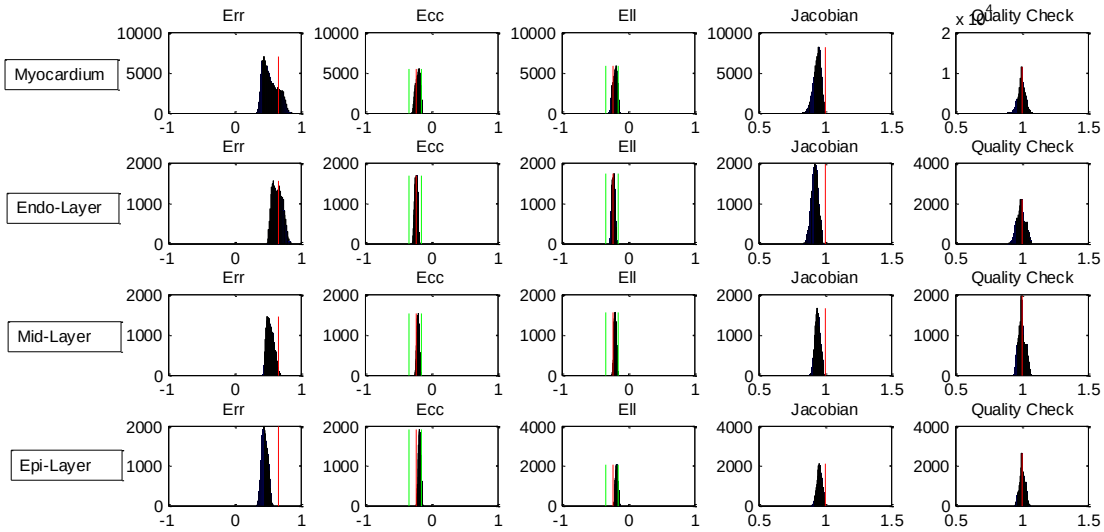

Figure 40. Statistic distribution of 3D strain. The red line is the reference value for myocardium, the green line is the reference value for epi- and endo-cardium.

Figure 40 (col 1-3) shows the statistical distribution of the strain value on different myocardial layer as well as on the whole myocardium. The red line is the theoretical value and the green line in Ecc and Ell are the theoretical value on the epi- and endo- surface. The radial strain shows significant differences on different layers. For circumferential and longitudinal strain, the 3D strain falls in the interval defined by the theoretical value. Figure 40 (col 4) shows the distribution of the Jacobian index. The Jacobian determinant is an indicator of spatial convergence. Jacobian determinant larger than 1 means spatial

divergent and smaller than 1 means spatial convergent. Here the Jacobian determinant is around 0.9, which might be caused by the imperfection of the motion field extraction. Figure 40 (col 5) show the quality check defined in 7.1.2. The quality check is 1.00 ±0.03, indicating good agreement with physical model.

Table 16. Strain from simulated data.

Theoretical	Radial strain(%)		Circumferential strain(%)		Longitudinal strain(%)	
	Epi	Endo	Epi	Endo	Epi	Endo
	66.9	66.9	-13.6±4.2	-29.6±10.2	-14.9	-33
Estimated	Radial strain(%)		Circumferential strain(%)		Longitudinal strain(%)	
	55.5±11.4		-19.6±3.3		-19.3±3.2	
	Epi	Endo	Epi	Endo	Epi	Endo
	41.8±2.7	74.8±4.4	-15.7±1.7	-25±1.1	-15.3±1.5	-24.6±1

Table 16 compares the theoretical strain calculated from the geometry change and the estimated strain from the motion field (Figure 25). Compared to the theoretical strain, the average 3D radial strain is underestimated (55.5% versus 66.9%). However, further decomposition on the radial direction gives a detailed distribution of the 3D radial strain, ranging from 41.8% to 74.8%. The circumferential strain and the longitudinal strain are approximately in the same range.

7.2.2 CLINICAL DATA RESULT

7.2.2.1 MOTION FIELD EXTRACTION

The average ejection fraction for the patient data is 52.24% ± 8.47%. The myocardial volume ratio between ED and ES phase is 0.97±0.10, indicating that the assumption of incompressibility of myocardium volume is reasonable.

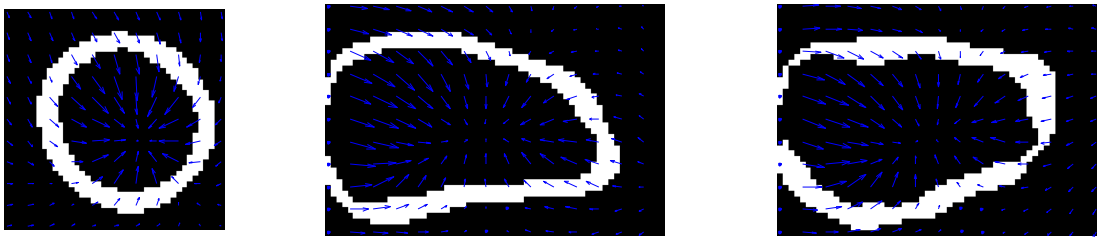

Figure 41. Motion field from myocardial mask registration with incompressibility regularization and rotational regularization

The motion field was extracted using the non-rigid registration algorithm with incompressibility regularization described in 5.3.2. Figure 41 shows an example of the motion field extracted from the myocardial mask. Figure 42 shows the 3D surface reconstructed from the short axis contours and 3 LAX contours.

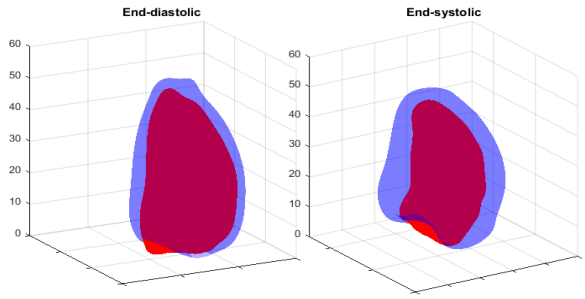

Figure 42. Example of 3D heart model recontructed from LAX contours

7.2.2.2 GLOBAL STRAIN : 3D VS 2D GLOBAL STRAIN

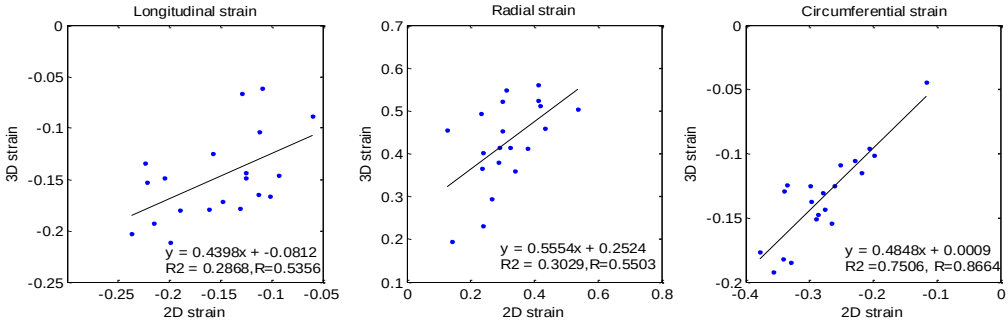

Figure 43. 3D strain versus 2D gloal strain.

Figure 43 compares the 3D peak strain with the 2D strain obtained from the global geometry change. The circumferential strain shows a good linear relationship (correlation coefficient R=0.8664), while the linear relationship between longitudinal and radial strain is less strong, with correlation coefficient 0.5356 and 0.5503, respectively.

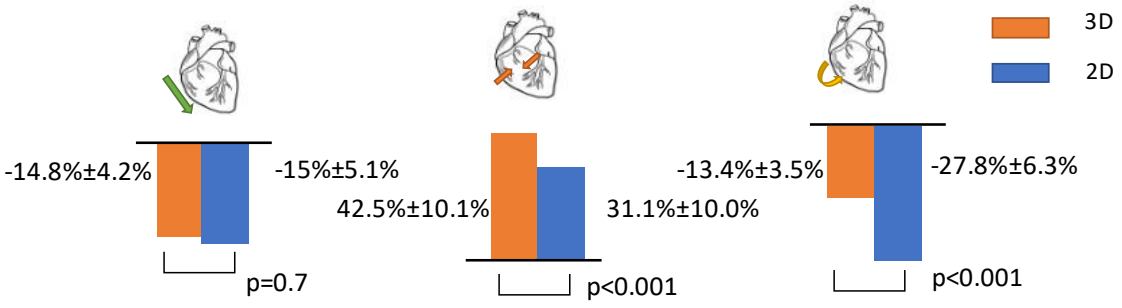

Figure 44. Comparison between 3D strain and 2D strain from all patient data

Figure 44 compares the 2D strain and 3D strain. The 3D radial strain is significantly larger than the 2D and the 3D circumferential strain is significantly smaller than the 2D strain. The difference between the longitudinal strain is not significant.

7.2.2.3 CORRELATION BETWEEN STRAIN AND EJECTION FRACTION

Figure 45 shows the relationship between 2D strain calculated from the contours and ejection fraction. The green points represent the patients without fibrosis in segment 5 or 11, and the red points represent the patients with fibrosis in segment 5 or 11. Patients with fibrosis show lower ejection fraction (<55%) compared with patients without fibrosis (>55%). However, some patients without fibrosis also show smaller ejection fraction. Patients with fibrosis also show smaller longitudinal, radial and circumferential strains. The result is consistent with the ejection fraction. The correlation coefficient between the longitudinal, radial circumferential and ejection fraction are -0.67 (p=0.011), 0.35 (p=0.12), -0.92 (p=0).

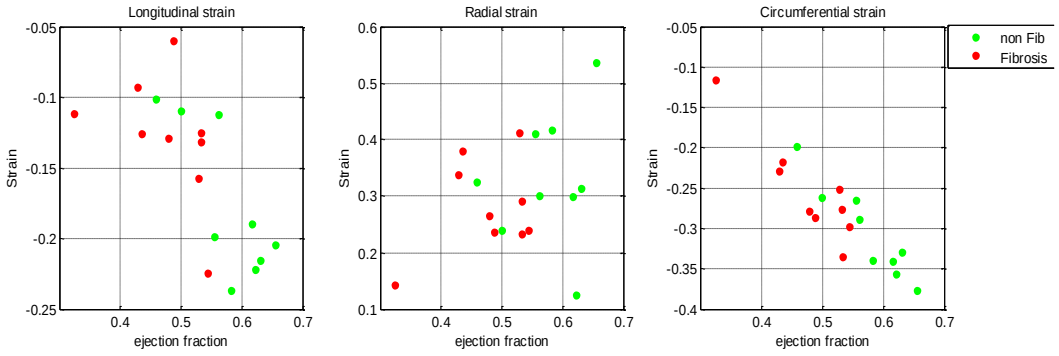

Figure 45. 2D strain versus ejection fraction

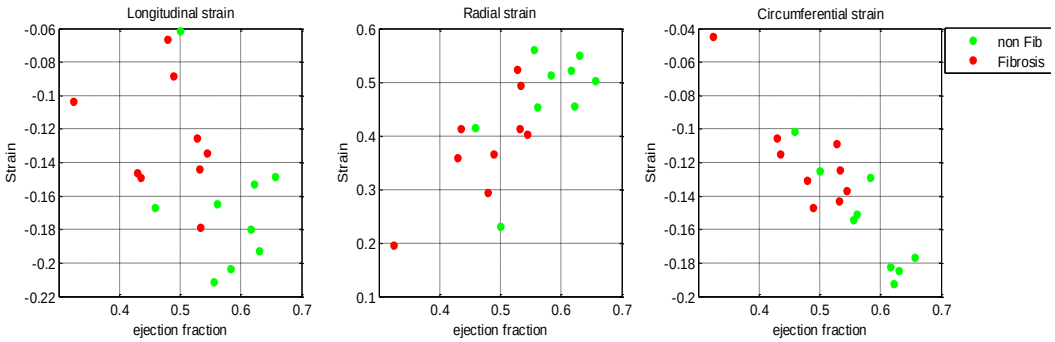

Figure 46. 3D strain versus ejection fraction

Figure 46 shows the correlation between the 3D strain and the ejection fraction. Compared to the 2D strain, the 3D radial strain shows better correlation with ejection fraction with correlation coefficient of 0.74 (p=0.0002). However the linear correlation in

longitudinal direction and circumferential direction are worse, with correlation coefficient of -0.41 (p=0.068) and -0.89 (p=0) respectively. The correction coefficient is summarized in Table 17.

Table 17. Correlation coefficient between strain and ejection fraction.

	Radial strain	Circumferential strain	Longitudinal strain
2D strain[114]	0.709	-0.775	-0.638
3D strain[114]	0.742	-0.862	-0.720
2D strain	0.35	-0.92	-0.67
3D strain	0.74	-0.89	-0.41

7.2.2.4 STRAIN DIFFERENCE BETWEEN PATIENT GROUPS

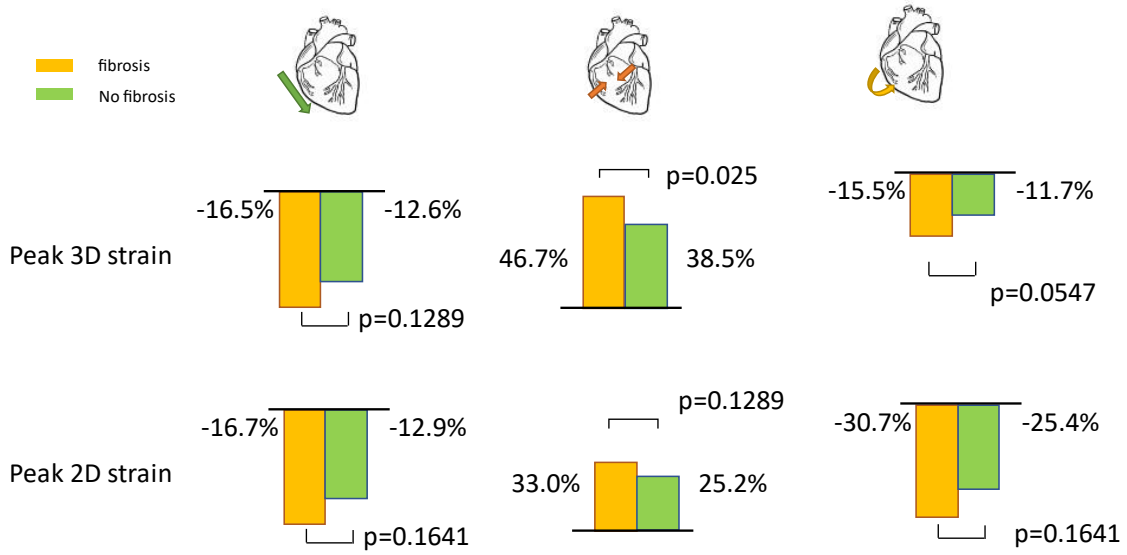

Figure 47. Comparison of strain between patients with and without fibrosis. (Row 1) 3D strain (Row 2) 2D strain

In this section, the global strain for patient with and without fibrosis is compared. Figure 47 shows the average 3D strain and 2D strain for these two patient group. The difference between those two groups are not significant for both 2D and 3D global strain. The result is also summarized in Table 18.

Table 18. Comparison between 3D strain calcuated from mask registration and 2D global strain

	Longitudinal			**Radial**			**Circumferential**		
	2D	3D	pValue	2D	3D	pValue	2D	3D	pValue
All patients	-15% ±5.1%	-14.8% ±4.2%	P=0.7	31.1% ±10.0%	42.5% ±10.1%	p<0.001	-27.8% ±6.3%	-13.4% ±3.5%	p<0.001
Non fibrosis	-16.7% ±5.3%	-16.5 ±4.4%	p=0.5	33.0% ±11.6%	46.7% ±10.1%	p=0.02	-30.7% ±5.7%	-15.5% ±3.2%	p=0.004
Fibrosis	-12.9% ±4.5%	-12.6% ±3.4%	p=1	28.2% ±8.3%	38.5% ±9.9%	p=0.004	-25.4% ±6.3%	-11.7% ±3.1%	p=0.004
pValue	p=0.1641	p=0.1289		p=0.1289	p=0.25		p=0.1641	p=0.0547	

7.2.2.5 *Regional Strain*

We further looked at the regional strain for different patient group in this section. Figure 48 gives example strain maps for a patient without Fibrosis (Patient 001) and with Fibrosis (Patient019). Three orthogonal planes were taken and the 3D strain for each pixel is shown in color coded image. The radial strain, circumferential strain and longitudinal strain for each segment is visualized at the bottom using bull's eye plot. Compared to patient 001 (no fibrosis), patient 019 (with fibrosis) shows lower strain value in all direction, especially in the segments where fibrosis exists.

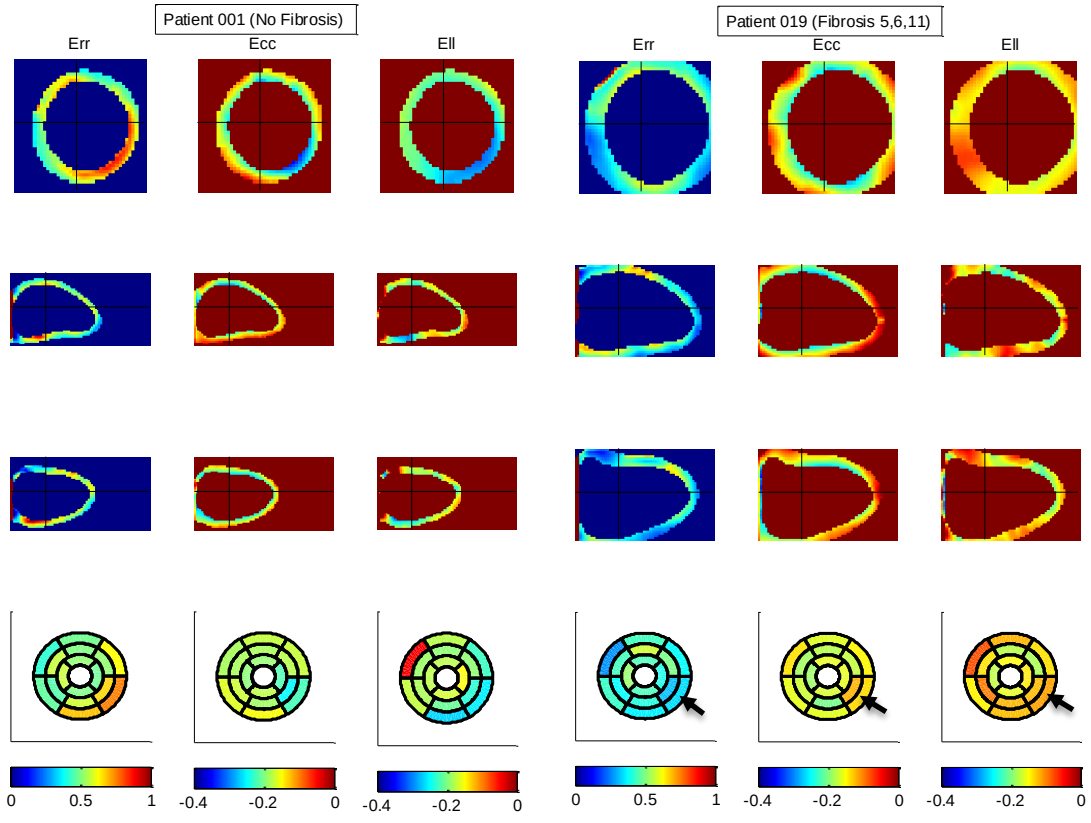

Figure 48. (left)Patient 001 , no fibrosis (right) Patient 019, fibrosis in segment 5,6,11

The patients were divided into two groups, with fibrosis in segment 11 and without fibrosis in segment 11. Figure 49 shows the average 3D strain in AHA-17 segment model. Compared to the patients with no fibrosis, the patients with fibrosis have smaller radial strain (Figure 49 Left)and lower circumferential strain (Figure 49 Middle). The difference in longitudinal strain (Figure 49 Right) is more complex. Segment 4,5,10,11 has smaller strain (marked as "-") while the other segment has larger (marked as "+") or similar strain.

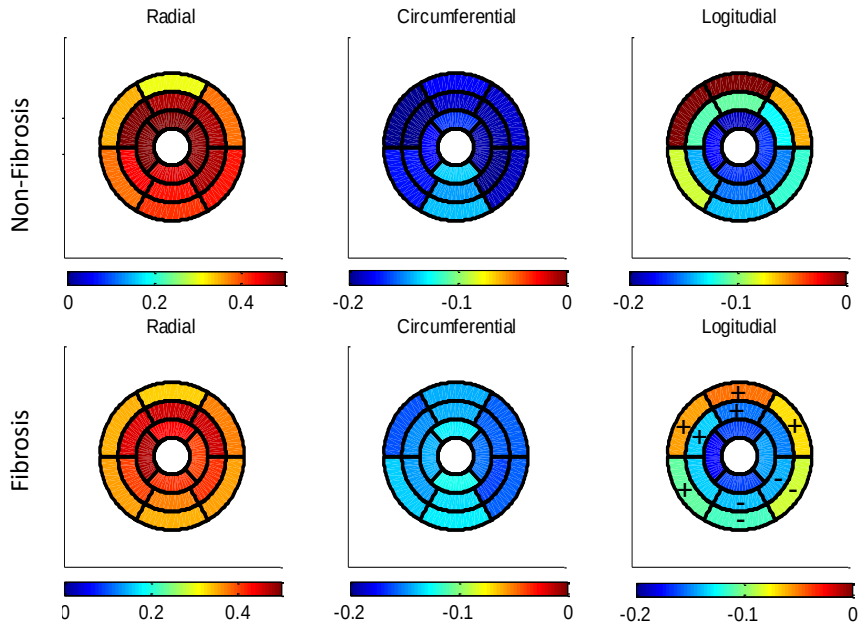

Figure 49. Average strain value on different group. The plus/minus sign represent relative value compared to non-fibrosis patients

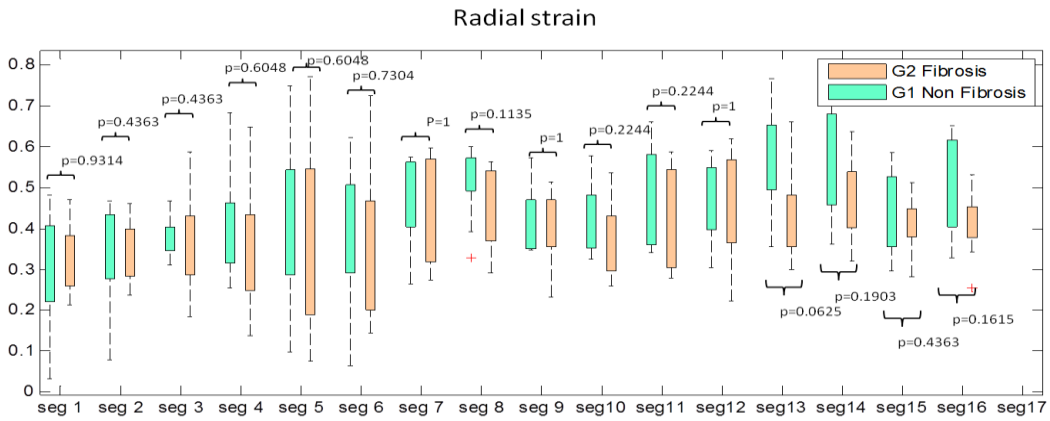

Figure 50. Segment-wise radial strain comparison between patient with fibrosis and without fibrosis. [*] indicate a significant difference between the two groups.

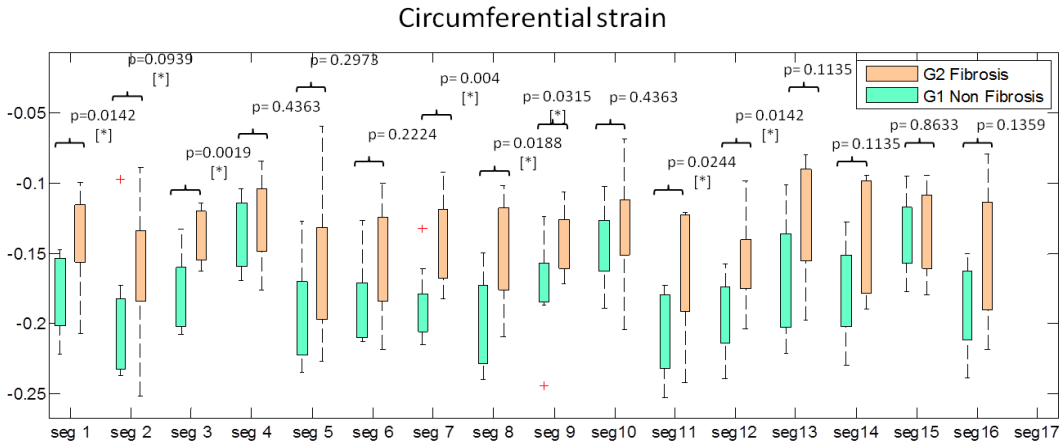

Figure 51. Segment-wise circumferential strain comparison between patient with fibrosis and without fibrosis. [*] indicate a significant difference between the two groups.

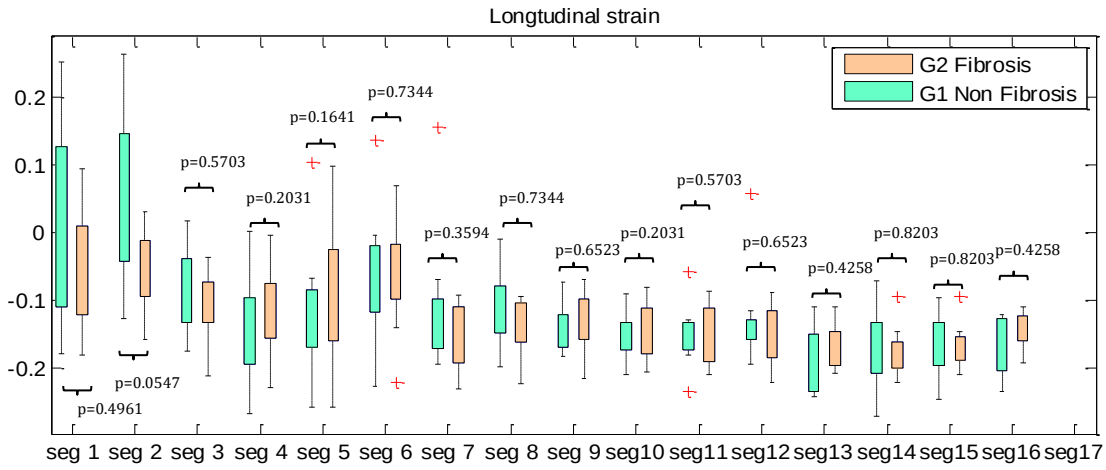

Figure 52. Segment-wise longitudinal strain comparison between patient with fibrosis and without fibrosis. [*] indicate a significant difference between the two groups

To further investigate the significant of the difference, the strain value for each segment was compared and the result is shown in Figure 50 - Figure 52. The difference in radial strain (Figure 52) and longitudinal strain (Figure 52) is not significant for all the segment. In circumferential strain (Figure 51), some segments show significant difference:

- In segment 11 , the circumferential strain for patient with fibrosis is significantly larger with p=0.0244.
- In segment 2,3,8,9, which is the septum area.
- In segment 1,7, which is the anterior region.

7.2.3 Strain Curve analysis Results

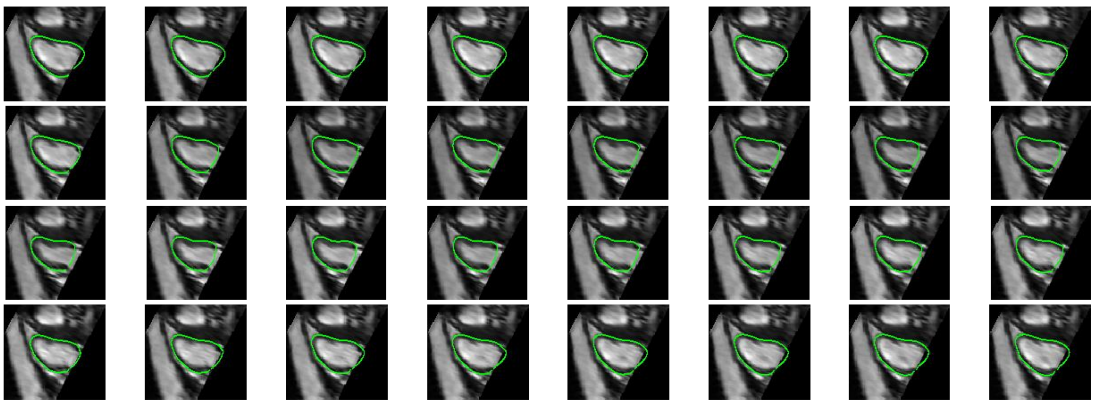

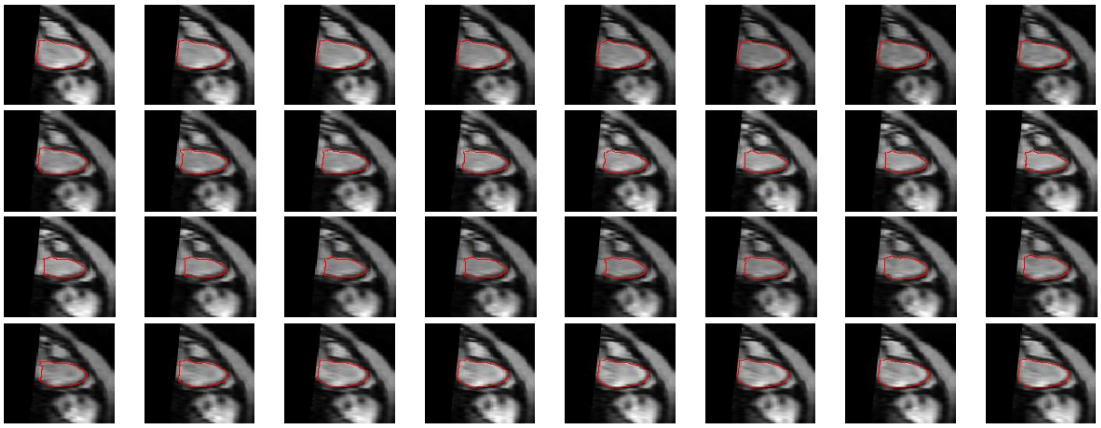

Figure 53. Example of epi and Endo cardial contours from the tracking algorithm

In order to calculate the strain curve, the heart model for each cardiac phase is obtained using the contour propagation in 5.4. Figure 53 shows an example of tracked contours. Figure 54 and Figure 55 gives an example of the strain curve for a patient with fibrosis in segment 11 (Figure 54) and a patient without fibrosis in segment 11(Figure 55).

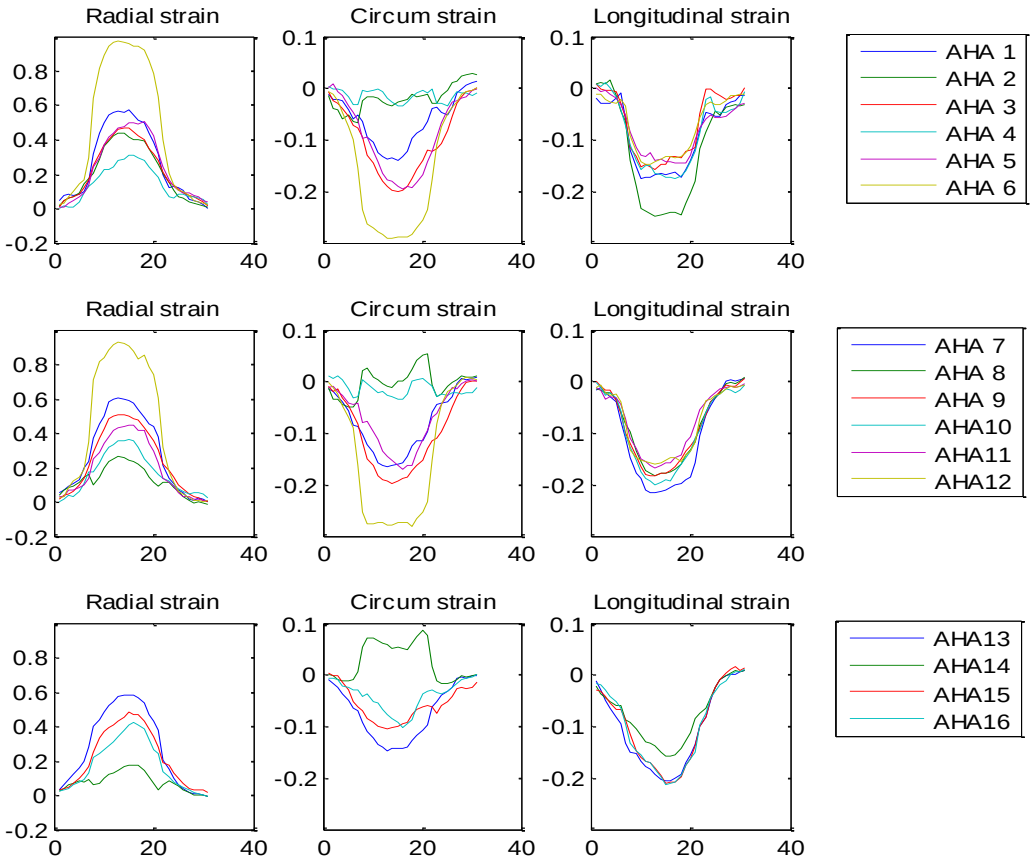

Figure 54. Strain curve patient nr.2 (fibrosis in segment 11)

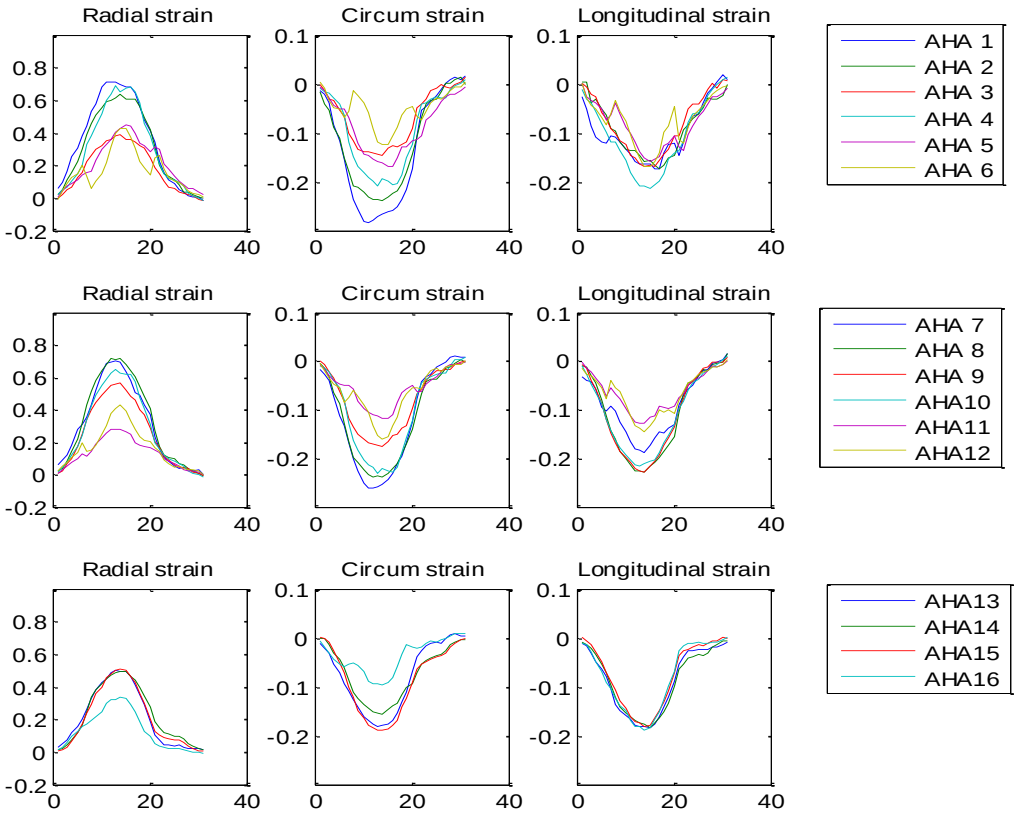

Figure 55. Strain curve patient nr.8 (no fibrosis in segment 11)

Table 19 shows the strain curves from all the patients. First column shows the patient Id and status of fibrosis. Second column shows the strain curve in radial, circumferential and longitudinal direction. Patients with fibrosis are marked with orange background. In general, patients with fibrosis have more inconsistent strain curve. The abnormal curves either have very large absolute value or reversed strain than normal strain, as indicated by the black arrow. However, some patients without fibrosis also shows similar curve, but less often.

Table 19. Strain curve for all the patients. Each plot contains curves for 16 segments.

patient	Err	Ecc	Ell
001 (n/a)	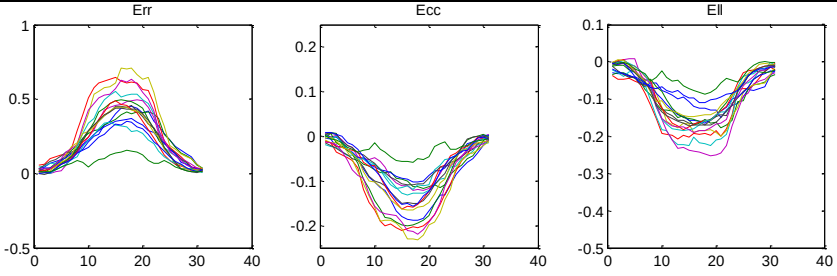		

002 (11)	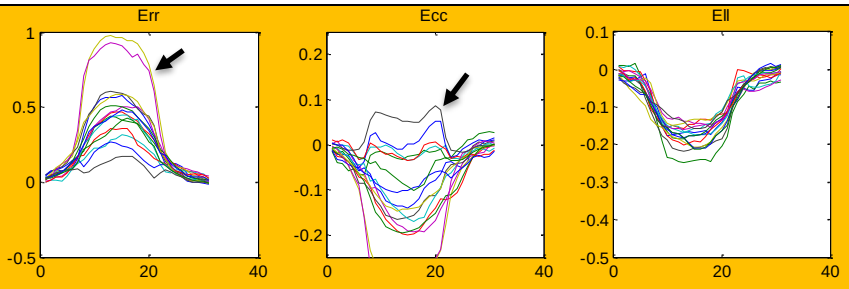
004 (5,6,11,12,16)	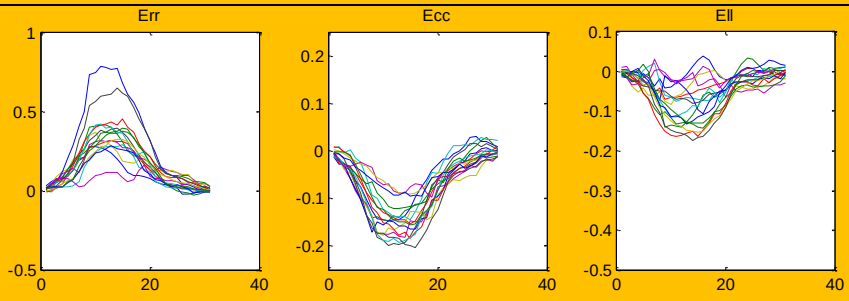
005 (11)	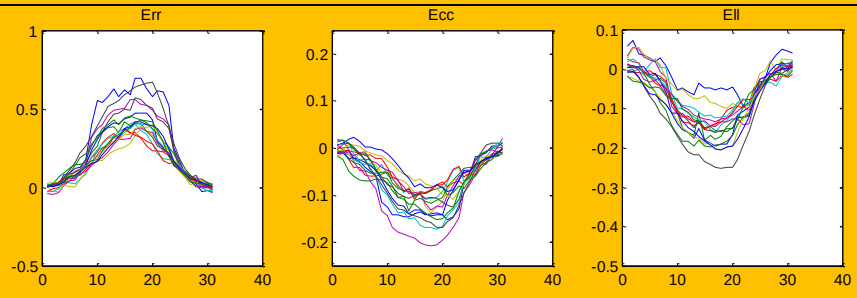
006 (5,11)	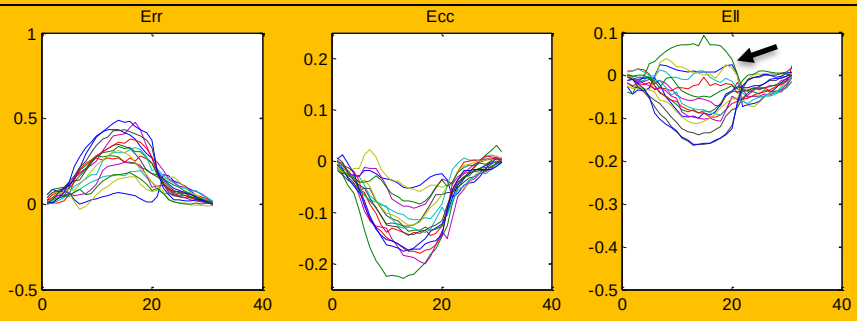
007 (5,11)	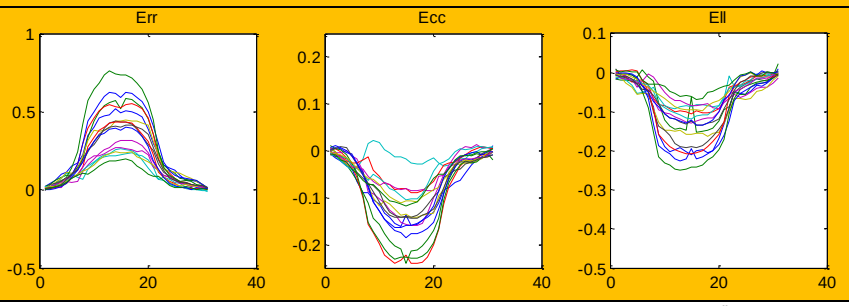
008 (n/a)	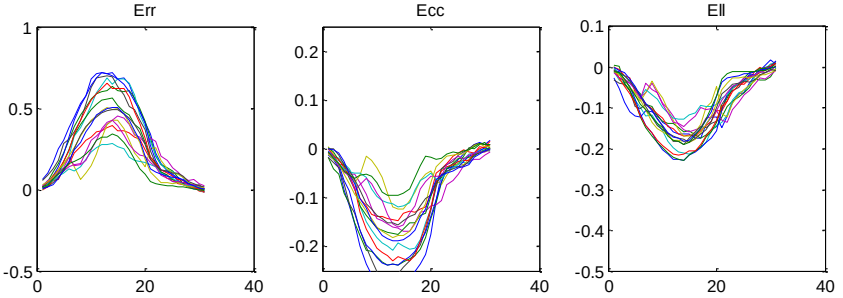

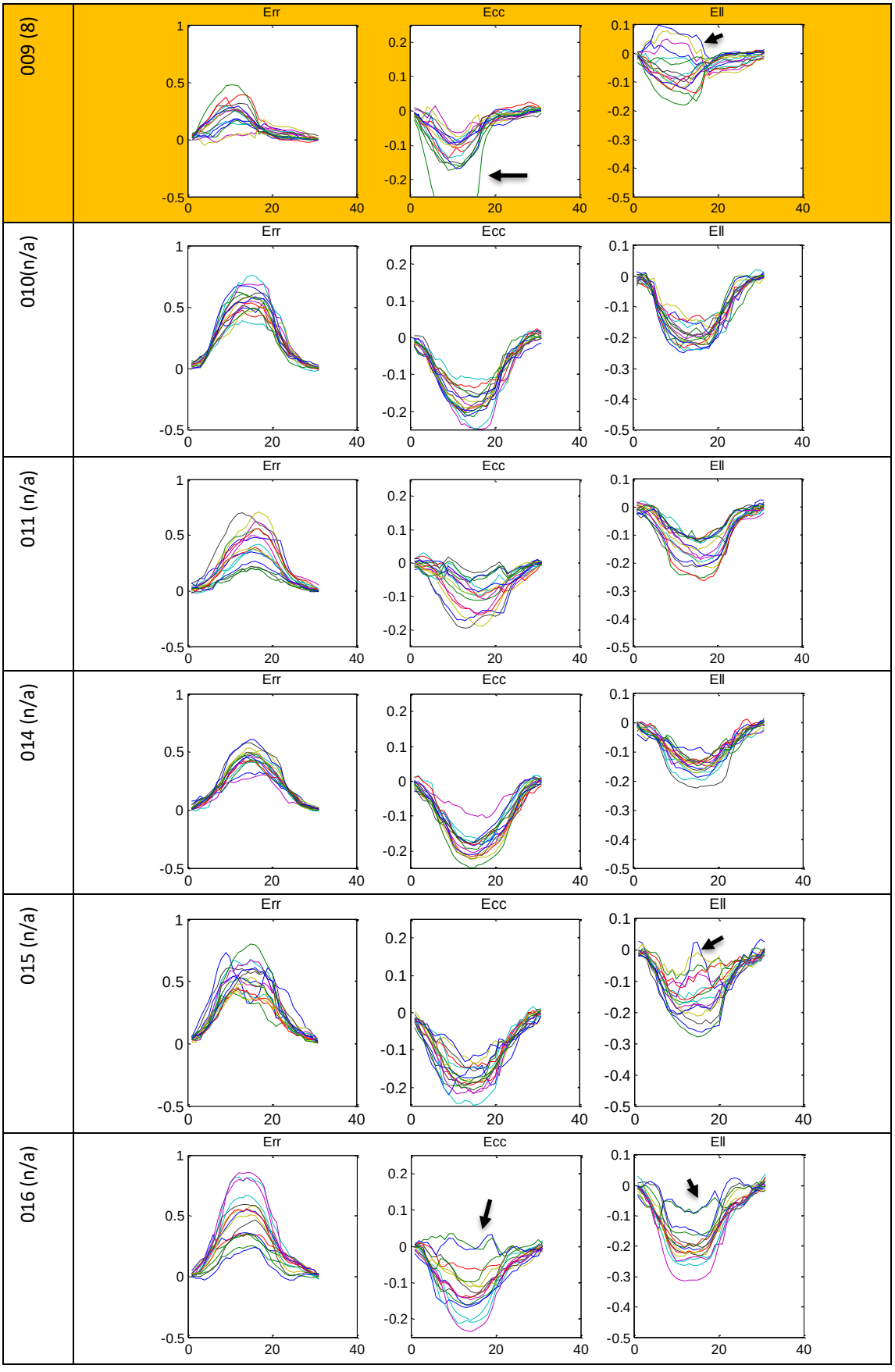
009 (8)
010(n/a)
011 (n/a)
014 (n/a)
015 (n/a)
016 (n/a)
Err
Ecc
Ell

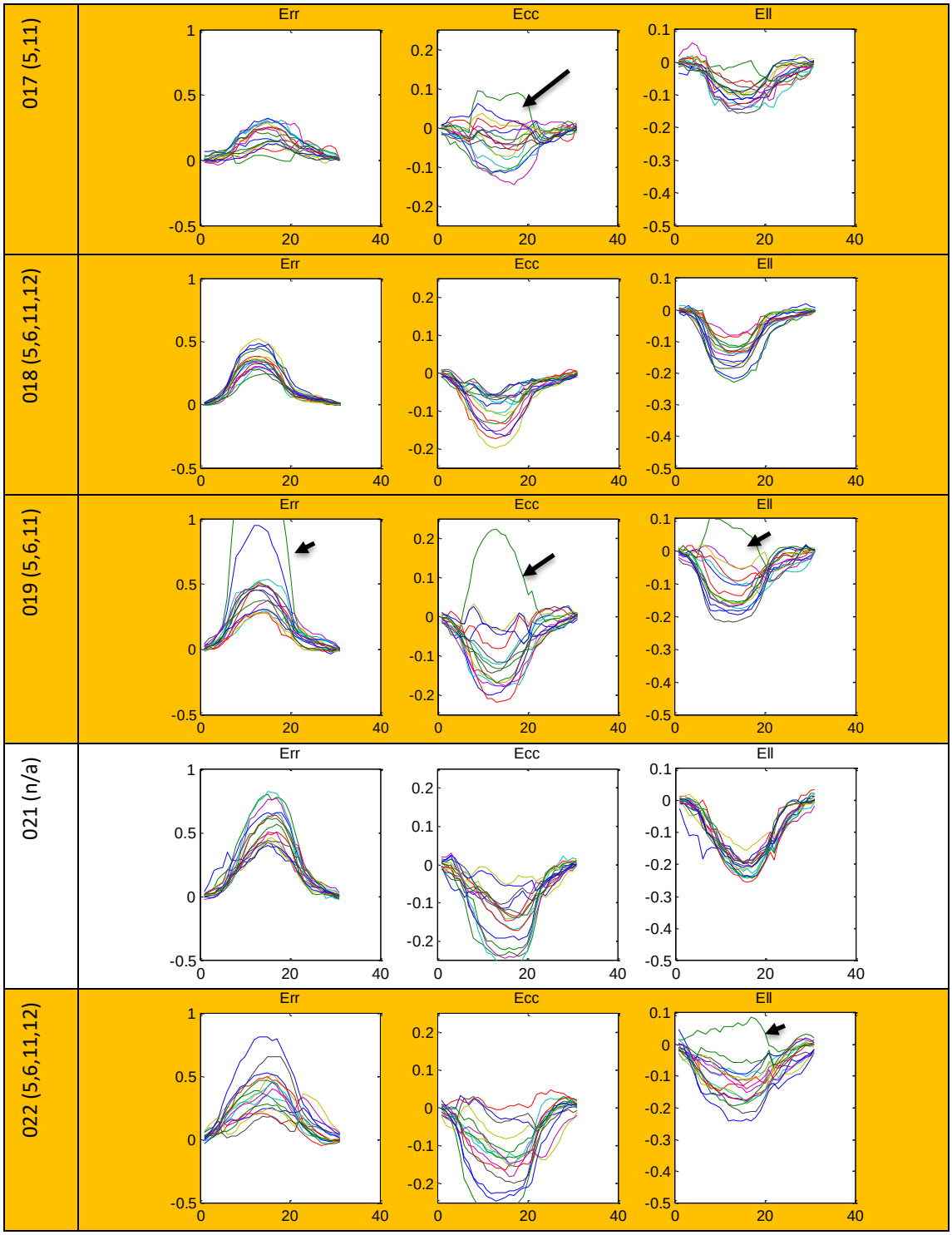

For each patient, the average strain curve was calculated by averaging the strain curves of the different segments. The correlation between the strain curve of each segment and the average strain curve was calculated and the result for all the patients is summarized in Figure 56. This measure is called correlation index in the remainder. For patients with fibrosis, the correlation index for circumferential strain is significantly smaller than the index for the patients without fibrosis in most segment, except segment 5, 11.

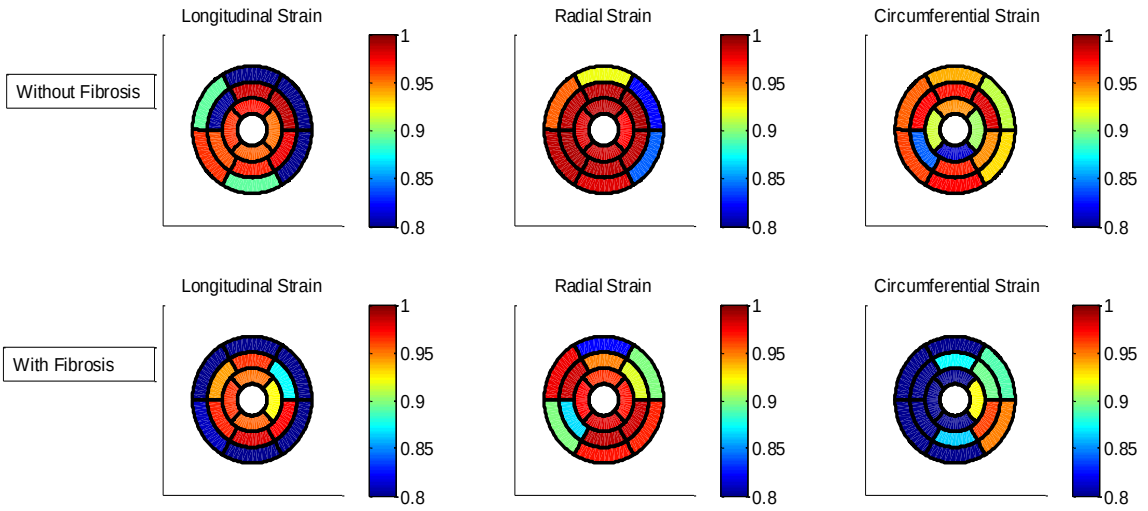

Figure 56. Correlation index, i.e. correlation between the strain curve of a segment and the average strain curve of all segments.

7.3 DISCUSSION

7.3.1 MOTION FIELD EXTRACTION

Most deformation field based methods have been based on gray scale image registration. Some researchers also used surface registration to extract the motion field. Others combined the image information with the heart model [121]. In this experiment, the motion field was extracted by registering the myocardial mask. This method is a hybrid method that incorporates the surface/model information into the registration. It keeps the important information of the myocardial boundary, but omits the detailed information inside the myocardium. For the heart model, this is acceptable because the left ventricle is approximately a cylindrical structure with uniform gray level, so the gray level information within the myocardium is considered unreliable for motion tracking.

The region-wise regularization with incompressibility and rotational constraints was introduced according to the incompressibility property of the myocardium and showed improved registration result. In addition, the rotational regularization was added to mimic the coherent contraction of the myocardial fiber. It prevents the registration from artificially introduced, large, unphysical local shearing in cases where the contours cannot be perfectly matched under the incompressibility assumption (due to inaccuracies in the segmentation).

7.3.2 STRAIN VALUES COMPARED TO PREVIOUS STUDY

In this chapter, the 3D Lagrange strain was calculated and validated on DMD patients, with and without fibrosis in segment 5 or 11. The absolute value of 3D strain is different from that reported in [100]. The longitudinal strain and radial strain are generally larger, while the circumferential strain is in the same range (Table 6, Figure 44). It also needs to be mentioned that, the strain value calculated by different tools may be different [14],[95]. This difference could be caused by several reasons, for example, imaging modality or tracking methods.

Although the strain values from different studies are different, the patients with fibrosis show smaller absolute strain in longitudinal, radial and circumferential directions. This trend is the same as reported in [100], but the difference is not as significant as reported in [100], which compared the DMD patients with the control group, while in our study we compared the DMD patients with and without fibrosis.

7.3.3 STRAIN MEASUREMENT : 3D VERSUS 2D STRAIN

Currently, 2D strain is more widely used in clinical applications. However, 2D strain is subject to the out-of-plan movement. Therefore, 3D strain is gaining more and more interest. In our study, the difference between 3D strain and 2D strain is significant for radial and circumferential strain and not significant for longitudinal strain (Figure 44).

The correlation between strain and ejection fraction was further investigated. Compared with the result in [114], the circumferential strain obtained in this study shows slightly stronger linear correlation with ejection fraction for both 2D and 3D strain. The 3D radial strain is similar to that in [114], while the 2D strain is much worse. For longitudinal strain, the 2D result is slightly improved, but the 3D result is worse. It needs to be mentioned that the 3D and 2D directions are actually defined differently, which explains why the strain decomposition is also different.

7.3.4 REGIONAL STRAIN

Currently, research on DMD patients has been focus on global strain. In this chapter, the regional strain, including peak systolic strain and strain curves, were analyzed. For DMD patients, it was shown in [102] that circumferential strain decreased compared with the control group. In this study, we further showed that, for DMD patients with fibrosis, the circumferential strain in the septum and anterior region is significantly lower than patients without fibrosis in segment 5 or 11.

The correlation index, defined as the correlation between the strain curve of a segment and the average strain curve of all segments, also shows lower values in circumferential strain in general (Figure 56), whereas in segment 5 or 11 the correlation is relatively high. This seems to indicate that the global circumferential strain can be better explained by the regional strain in segment 5 and 11. Since the global circumferential strain is significantly smaller, this could be caused by the lower contractility in segments 5 and 11. The lower correlation index of the other segments could also mean that there is more variability across different segments, which is an indicator of contractile dysfunction.

Chapter 8 Conclusions and future WORK

8.1 CONCLUSIONS

This work is motivated by the emerging of new MRI imaging technologies and new image reconstruction methods. The aim is to investigate how image processing methods can be used to extract valid clinical information from MRI images. In this work, two topics were selected, myocardial T_1 mapping and myocardial strain analysis based on 3D isotropic cine images.

- Thanks to the development of cardiac gating and motion correction, T_1 mapping is becoming more common in medical centers. However, there are several problems. First, the raw image is subject to image noise and cardiac motion. Therefore, post processing is required. To solve this problem, a vectorized Levenberg-Marquardt algorithm that processing the image as a whole was proposed. This method uses the information of the neighboring pixels, therefore provides more robust results and is less subject to the local minimum problem. Secondly, researches from different groups are based on different MR sequences and different curve fitting methods. Therefore, different methods and workflows need to be compared. To solve this problem, images acquired with different sequences, MOLLI and SMART1Map, were collected. 3-parameter and 2-parameter fitting models were compared. In addition, to support validation work for clinical researchers, a software was implemented, allowing the proposed fitting methods to be applied on different sequence and with different models. Finally, due to the expectation of 3D T_1 mapping in the near future, an initial implementation on GPU was conducted.

- Currently, most cardiac function analysis is based on 2D cine stacks. However, with new image reconstruction technology, 3D isotropic cine imaging has become possible. Compared to 2D imaging, 3D cine-based analysis is less subject to through-plane motion and could potentially provide a better estimate of cardiac function. The work on strain analysis is triggered by this new imaging data.

Problems in strain analysis include motion field estimation and strain analysis. In this work, the motion field was extracted using image registration of myocardial masks. This method is fast and takes into account the information of the heart model. In addition, physical constraints, such as incompressibility regularization and rotation regularization, were added to improve the motion field extraction. Compared to 2D global strain, the 3D radial strain shows larger values and the 3D circumferential strain has smaller values. The difference between 3D and 2D strain values is significant for radial and circumferential direction, while the difference in longitudinal strain is not significant. In this work, the DMD patient data were divided into two groups, patients with fibrosis and without fibrosis. The regional 3D strains were compared between different groups. A significant difference was found in circumferential strain in the septum and anterior region. Furthermore, the strain curves for different patient groups were calculated and a correlation index was proposed to distinguish abnormal segments in terms of strain curve patterns. The correlation index of circumferential strain showed smaller value for DMD patients with fibrosis and could potentially be used as a parameter to assess the progressive status of DMD patients.

8.2 FUTURE WORK

Motion information is very important in cardiac analysis. In cardiac T_1 mapping, motion introduces misalignment between images, and needs to be corrected. In cardiac strain analysis, motion provides information about the contractile function of myocardial tissue. In this study, the motion information is extracted using an image registration technique. However, in recent years, machine learning has been proved to be an useful tool not only for tasks such as object recognition, but also for motion estimation. One example is FlowNet, which is proposed by Phlipp Fischer et al in [122] and validated with synthetic data sets. Eddy Ilg et al further improved the accuracy for small motion by introducing an end-to-end learning concept [123]. Hopefully this technique could improve the motion estimation.

In Chapter 4, spatial regularization was applied to improve T_1 mapping. The workflow was validated on 16 patients. Pre-contrast and post-contrast images were acquired for each

patient using MOLLI and SMART1Map sequence. However, validation on a larger scale clinical data could still be interesting. In addition, new analysis methods such as machine learning might also be worth investigating.

In Chapter 5, the myocardial strain is analyzed on DMD patients with and without fibrosis. The research compared the global peak strain, regional peak strain and regional strain curves among the two groups. Further investigation could be on the following areas:

- Strain pattern analysis. In this work, the strain curve is calculated and the correlation to the average strain curve is calculated and compared. However, it would be interesting to do further data mining to extract more information from the strain curves, and machine learning could be helpful in this area.

- Comparative study of different imaging modalities. Currently, most strain studies are based on ultrasound images and tagged MR images. In these two methods, motion is encoded by labeling the tissue during the imaging process. In cine images, on the other hand, motion is estimated by matching the images. Therefore, the motion estimation may not match the actual motion. However, this does not prevent us from extracting clinically valid information using this method.

- Compare the patient group with healthy control group or perform long-term monitoring of patient status. In this work, the comparison is done between patients with and without fibrosis. However, due to individual differences, the statistics might not be significant. To validate this method more thoroughly, it would be interesting to compare the patient group with control group. It would also be interesting to follow up the patients and see if this method can be used to evaluate the patient's status.

Reference

[1] N. Townsend, L. Wilson, P. Bhatnagar, K. Wickramasinghe, M. Rayner, M. Nichols, Cardiovascular disease in Europe: epidemiological update 2016, Eur. Heart J. 37 (2016) 3232–3245. https://doi.org/10.1093/eurheartj/ehw334.

[2] European heart network, European Cardiovascular Disease Statistics 2017, (n.d.). http://www.ehnheart.org/cvd-statistics.html (accessed March 21, 2020).

[3] WHO | Global atlas on cardiovascular disease prevention and control, (n.d.). https://www.who.int/cardiovascular_diseases/publications/atlas_cvd/en/ (accessed March 21, 2020).

[4] D.C. Lee, M. Markl, E. Dall'Armellina, Y. Han, S. Kozerke, T. Kuehne, S. Nielles-Vallespin, D. Messroghli, A. Patel, T. Schaeffter, O. Simonetti, A.M. Valente, J.W. Weinsaft, G. Wright, S. Zimmerman, J. Schulz-Menger, The growth and evolution of cardiovascular magnetic resonance: a 20-year history of the Society for Cardiovascular Magnetic Resonance (SCMR) annual scientific sessions, J. Cardiovasc. Magn. Reson. 20 (2018) 8. https://doi.org/10.1186/s12968-018-0429-z.

[5] S. Valbuena-López, R. Hinojar, V.O. Puntmann, Cardiovascular Magnetic Resonance in Cardiology Practice: A Concise Guide to Image Acquisition and Clinical Interpretation, Rev. Esp. Cardiol. Engl. Ed. 69 (2016) 202–210. https://doi.org/10.1016/j.rec.2015.11.011.

[6] T.A. Treibel, S.K. White, J.C. Moon, Myocardial Tissue Characterization: Histological and Pathophysiological Correlation, Curr. Cardiovasc. Imaging Rep. 7 (2014). https://doi.org/10.1007/s12410-013-9254-9.

[7] V.M. Ferreira, S.K. Piechnik, M.D. Robson, S. Neubauer, T.D. Karamitsos, Myocardial Tissue Characterization by Magnetic Resonance Imaging, J. Thorac. Imaging. 29 (2014) 147–154. https://doi.org/10.1097/RTI.0000000000000077.

[8] P. Montant, M. Sigovan, D. Revel, P. Douek, MR imaging assessment of myocardial edema with T2 mapping, Diagn. Interv. Imaging. 96 (2015) 885–890. https://doi.org/10.1016/j.diii.2014.07.008.

[9] Prognostic Value of Cardiac Magnetic Resonance Stress Tests | Circulation, (n.d.). https://www.ahajournals.org/doi/10.1161/CIRCULATIONAHA.106.652016 (accessed April 17, 2020).

[10] A. Menini, P.-A. Vuissoz, J. Felblinger, F. Odille, Joint Reconstruction of Image and Motion in MRI: Implicit Regularization Using an Adaptive 3D Mesh, in: Proc. 15th Int. Conf. Med. Image Comput. Comput.-Assist. Interv. - Vol. Part I, Springer-Verlag, Berlin, Heidelberg, 2012: pp. 264–271. https://doi.org/10.1007/978-3-642-33415-3_33.

[11] M.E. Crowe, A.C. Larson, Q. Zhang, J. Carr, R.D. White, D. Li, O.P. Simonetti, Automated rectilinear self-gated cardiac cine imaging, Magn. Reson. Med. 52 (2004) 782–788. https://doi.org/10.1002/mrm.20212.

[12] P. Kellman, H. Xue, K. Chow, B.S. Spottiswoode, A.E. Arai, R.B. Thompson, Optimized saturation recovery protocols for T1-mapping in the heart: influence of sampling strategies on precision, J. Cardiovasc. Magn. Reson. 16 (2014). https://doi.org/10.1186/s12968-014-0055-3.

[13] G. Ramos-Llorden, A.J. den Dekker, G. Van Steenkiste, J. Van Audekerke, M. Verhoye, J. Sijbers, Simultaneous motion correction and T1 estimation in quantitative T1 mapping: An ML restoration approach, in: IEEE, 2015: pp. 3160–3164. https://doi.org/10.1109/ICIP.2015.7351386.

[14] M.S. Amzulescu, M. De Craene, H. Langet, A. Pasquet, D. Vancraeynest, A.C. Pouleur, J.L. Vanoverschelde, B.L. Gerber, Myocardial strain imaging: review of general principles, validation, and sources of discrepancies, Eur. Heart J. - Cardiovasc. Imaging. 20 (2019) 605–619. https://doi.org/10.1093/ehjci/jez041.

[15] T.J. Sumpf, M. Uecker, S. Boretius, J. Frahm, Model-based nonlinear inverse reconstruction for T2 mapping using highly undersampled spin-echo MRI, J. Magn. Reson. Imaging. 34 (2011) 420–428. https://doi.org/10.1002/jmri.22634.

[16] MRI sequences: spin echo, gradient echo, echo planar, IMAIOS. (n.d.). https://www.imaios.com/en/e-Courses/e-MRI/MRI-Sequences (accessed June 27, 2019).

[17] F. Odille, A. Bustin, S. Liu, B. Chen, P.-A. Vuissoz, J. Felblinger, L. Bonnemains, Isotropic 3D cardiac cine MRI allows efficient sparse segmentation strategies based on 3D surface reconstruction, Magn. Reson. Med. 79 (2018) 2665–2675. https://doi.org/10.1002/mrm.26923.

[18] K.W. Cummings, S. Bhalla, C. Javidan-Nejad, A.J. Bierhals, F.R. Gutierrez, P.K. Woodard, A pattern-based approach to assessment of delayed enhancement in nonischemic cardiomyopathy at MR imaging, Radiogr. Rev. Publ. Radiol. Soc. N. Am. Inc. 29 (2009) 89–103. https://doi.org/10.1148/rg.291085052.

[19] P.K. Kim, Y.J. Hong, D.J. Im, Y.J. Suh, C.H. Park, J.Y. Kim, S. Chang, H.-J. Lee, J. Hur, Y.J. Kim, B.W. Choi, Myocardial T1 and T2 Mapping: Techniques and Clinical Applications, Korean J. Radiol. 18 (2017) 113–131. https://doi.org/10.3348/kjr.2017.18.1.113.

[20] P. Haaf, P. Garg, D. R.Messroghli, D. A.Broadbent, J. P.Greenwood, S. Plein, Cardiac T1 Mapping and Extracellular Volume (ECV) in clinical practice: a comprehensive review, J. Cardiovasc. Magn. Reson. 18 (2016). https://doi.org/10.1186/s12968-016-0308-4.
[21] D.R. Messroghli, A. Radjenovic, S. Kozerke, D.M. Higgins, M.U. Sivananthan, J.P. Ridgway, Modified Look-Locker inversion recovery (MOLLI) for high-resolutionT1 mapping of the heart, Magn. Reson. Med. 52 (2004) 141–146. https://doi.org/10.1002/mrm.20110.
[22] D. Dabir, N. Child, A. Kalra, T. Rogers, R. Gebker, A. Jabbour, S. Plein, C.-Y. Yu, J. Otton, A. Kidambi, A. McDiarmid, D. Broadbent, D.M. Higgins, B. Schnackenburg, L. Foote, C. Cummins, E. Nagel, V.O. Puntmann, Reference values for healthy human myocardium using a T1 mapping methodology: results from the International T1 Multicenter cardiovascular magnetic resonance study, J. Cardiovasc. Magn. Reson. Off. J. Soc. Cardiovasc. Magn. Reson. 16 (2014) 69. https://doi.org/10.1186/s12968-014-0069-x.
[23] C.T. Sibley, J. Huang, M. Ugander, A. Oki, J. Han, M.S. Nacif, A. Greiser, D.R. Messroghli, P. Kellman, A.E. Arai, D.A. Bluemke, S. Liu, Myocardial and blood T1 quantification in normal volunteers at 3T, J. Cardiovasc. Magn. Reson. 13 (2011) P51. https://doi.org/10.1186/1532-429X-13-S1-P51.
[24] F. von Knobelsdorff-Brenkenhoff, M. Prothmann, M.A. Dieringer, R. Wassmuth, A. Greiser, C. Schwenke, T. Niendorf, J. Schulz-Menger, Myocardial T1 and T2 mapping at 3 T: reference values, influencing factors and implications, J. Cardiovasc. Magn. Reson. 15 (2013) 53. https://doi.org/10.1186/1532-429X-15-53.
[25] J.J. Lee, S. Liu, M.S. Nacif, M. Ugander, J. Han, N. Kawel, C.T. Sibley, P. Kellman, A.E. Arai, D.A. Bluemke, Myocardial T1 and extracellular volume fraction mapping at 3 tesla, J. Cardiovasc. Magn. Reson. 13 (2011) 75. https://doi.org/10.1186/1532-429X-13-75.
[26] J.A. Stainsby, G.S. Slavin, Myocardial T1 mapping using SMART1Map: initial in vivo experience, J. Cardiovasc. Magn. Reson. 15 (2013) P13. https://doi.org/10.1186/1532-429X-15-S1-P13.
[27] A.H. Ellims, L.M. Iles, L. Ling, B. Chong, I. Macciocca, G.S. Slavin, J.L. Hare, D.M. Kaye, S.F. Marasco, C.A. McLean, P.A. James, D. du Sart, A.J. Taylor, A comprehensive evaluation of myocardial fibrosis in hypertrophic cardiomyopathy with cardiac magnetic resonance imaging: linking genotype with fibrotic phenotype, Eur. Heart J. Cardiovasc. Imaging. 15 (2014) 1108–1116. https://doi.org/10.1093/ehjci/jeu077.
[28] A.N. Bhuva, T.A. Treibel, H. Bulluck, J. Simpson, C. Manisty, J. Moon, Precision and reproducibility of blood T1 estimation: implications of T1 star on ECV calculation, J. Cardiovasc. Magn. Reson. 17 (2015) 1. https://doi.org/10.1186/1532-429X-17-S1-P4.
[29] I.I. Rabi, N.F. Ramsey, J. Schwinger, Use of Rotating Coordinates in Magnetic Resonance Problems, Rev. Mod. Phys. 26 (1954) 167–171. https://doi.org/10.1103/RevModPhys.26.167.
[30] M. Markl, Velocity Encoding and Flow Imaging, (2006).
[31] R.J. van der Geest, P. Garg, Advanced Analysis Techniques for Intra-cardiac Flow Evaluation from 4D Flow MRI, Curr. Radiol. Rep. 4 (2016). https://doi.org/10.1007/s40134-016-0167-7.
[32] S. Crandon, M.S.M. Elbaz, J.J.M. Westenberg, R.J. van der Geest, S. Plein, P. Garg, Clinical applications of intra-cardiac four-dimensional flow cardiovascular magnetic resonance: A systematic review, Int. J. Cardiol. 249 (2017) 486–493. https://doi.org/10.1016/j.ijcard.2017.07.023.
[33] S. Mori, J. Zhang, Principles of diffusion tensor imaging and its applications to basic neuroscience research, Neuron. 51 (2006) 527–539. https://doi.org/10.1016/j.neuron.2006.08.012.
[34] P.J. Basser, J. Mattiello, D. LeBihan, MR diffusion tensor spectroscopy and imaging, Biophys. J. 66 (1994) 259–267. https://doi.org/10.1016/S0006-3495(94)80775-1.
[35] C. Mekkaoui, T.G. Reese, M.P. Jackowski, H. Bhat, D.E. Sosnovik, Diffusion MRI in the heart, Nmr Biomed. 30 (2017). https://doi.org/10.1002/nbm.3426.
[36] C.R. Comeau, S.G. Luebchow, Cardiac MR: A Practical Imaging Guide, (n.d.) 66.
[37] G. Hermosillo, C. Chefd'hotel, K.-H. Herrmann, G. Bousquet, L. Bogoni, K. Chaudhuri, D.R. Fischer, C. Geppert, R. Janka, A. Krishnan, B. Kiefer, I. Krumbein, W. Kaiser, M. Middleton, W. Ou, J.R. Reichenbach, M. Salganicoff, M. Schmitt, E. Wenkel, S. Wurdinger, L. Zhang, Image Registration in Medical Imaging: Applications, Methods, and Clinical Evaluation, in: A.S. El-Baz, R. Acharya U, A.F. Laine, J.S. Suri (Eds.), Multi Modality State---Art Med. Image Segmentation Regist. Methodol. Vol. II, Springer New York, New York, NY, 2011: pp. 263–313. https://doi.org/10.1007/978-1-4419-8204-9_11.
[38] F. Odille, A. Menini, J. Escanyé, P. Vuissoz, P. Marie, M. Beaumont, J. Felblinger, Joint Reconstruction of Multiple Images and Motion in MRI: Application to Free-Breathing Myocardial$\rm T_2$Quantification, IEEE Trans. Med. Imaging. 35 (2016) 197–207. https://doi.org/10.1109/TMI.2015.2463088.

[39] J. Mitra, R. Marti, A. Oliver, X. Llado, J.C. Vilanova, F. Meriaudeau, A comparison of thin-plate splines with automatic correspondences and B-splines with uniform grids for multimodal prostate registration, in: K.H. Wong, D.R. Holmes III (Eds.), 2011: p. 79642T. https://doi.org/10.1117/12.877956.
[40] M.Y. CHU, MUTUAL INFORMATION BASED NON-RIGID IMAGE REGISTRATION USING ADAPTIVE GRID GENERATION: GPU IMPLEMENTATION AND APPLICATION TO BREAST MRI, (n.d.) 94.
[41] H. Kushner, G. Yin, Stochastic Approximation and Recursive Algorithms and Applications, 2nd ed., Springer-Verlag, New York, 2003. //www.springer.com/la/book/9780387008943 (accessed June 16, 2018).
[42] S. Klein, J.P.W. Pluim, M. Staring, M.A. Viergever, Adaptive Stochastic Gradient Descent Optimisation for Image Registration, Int. J. Comput. Vis. 81 (2009) 227. https://doi.org/10.1007/s11263-008-0168-y.
[43] B. A. Murtagh, R. Sargent, A Constrained Minimization Method with Quadratic Convergence, 1969.
[44] R. Fletcher, Practical Methods of Optimization | Wiley Online Books, (1987). https://onlinelibrary.wiley.com/doi/book/10.1002/9781118723203 (accessed July 6, 2019).
[45] B. Fischer, J. Modersitzki, Fast diffusion registration, 2002. https://doi.org/10.1090/conm/313/05372.
[46] B. Fischer, J. Modersitzki, Curvature Based Image Registration, J. Math. Imaging Vis. 18 (2003) 81–85. https://doi.org/10.1023/A:1021897212261.
[47] V. Vishnevskiy, T. Gass, G. Székely, O. Goksel, Total Variation Regularization of Displacements in Parametric Image Registration, in: H. Yoshida, J.J. Näppi, S. Saini (Eds.), Abdom. Imaging Comput. Clin. Appl., Springer International Publishing, Cham, 2014: pp. 211–220. https://doi.org/10.1007/978-3-319-13692-9_20.
[48] E. Haber, S. Heldmann, J. Modersitzki, A Framework for Image-Based Constrained Registration with an Application to Local Rigidity, (n.d.) 16.
[49] J. Modersitzki, Image Registration with Local Rigidity Constraints, in: A. Horsch, T.M. Deserno, H. Handels, H.-P. Meinzer, T. Tolxdorff (Eds.), Bildverarb. Für Med. 2007, Springer Berlin Heidelberg, Berlin, Heidelberg, 2007: pp. 444–448. https://doi.org/10.1007/978-3-540-71091-2_89.
[50] Numerical optimization for constrained image registration - Haber - 2010 - Numerical Linear Algebra with Applications - Wiley Online Library, (n.d.). https://onlinelibrary.wiley.com/doi/abs/10.1002/nla.715 (accessed June 19, 2018).
[51] C. Broit, Optimal Registration of Deformed Images, PhD Thesis, University of Pennsylvania, 1981.
[52] A. Sotiras, C. Davatzikos, N. Paragios, Deformable Medical Image Registration: A Survey, IEEE Trans. Med. Imaging. 32 (2013) 1153–1190. https://doi.org/10.1109/TMI.2013.2265603.
[53] G.E. Christensen, Deformable Shape Models For Anatomy, 1994.
[54] E. Haber, J. Modersitzki, Volume Preserving Image Registration, in: C. Barillot, D.R. Haynor, P. Hellier (Eds.), Med. Image Comput. Comput.-Assist. Interv. – MICCAI 2004, Springer Berlin Heidelberg, 2004: pp. 591–598.
[55] J. Han, J. Hornegger, T. Kuwert, W. Bautz, Feature Constrained Non-rigid Image Registration, n.d.
[56] G.E. Christensen, M.I. Miller, M.W. Vannier, U. Grenander, Individualizing neuro-anatomical atlases using a massively parallel computer, Computer. 29 (1996) 32–38. https://doi.org/10.1109/2.481434.
[57] C.B. Fookes, A.J. Maeder, Comparison of popular non-rigid image registration techniques and a new hybrid mutual information-based fluid algorithm, in: The Australian Pattern Recognition Society, Brisbane, Australia, 2003: pp. 57–62. http://www.aprs.org.au/wdic2003/ (accessed June 30, 2019).
[58] J.P. Thirion, Image matching as a diffusion process: an analogy with Maxwell's demons, Med. Image Anal. 2 (1998) 243–260.
[59] X. Pennec, P. Cachier, N. Ayache, Understanding the "Demon's Algorithm": 3D Non-rigid Registration by Gradient Descent, in: C. Taylor, A. Colchester (Eds.), Med. Image Comput. Comput.-Assist. Interv. – MICCAI'99, Springer Berlin Heidelberg, Berlin, Heidelberg, 1999: pp. 597–605. https://doi.org/10.1007/10704282_64.
[60] B.B. Avants, C.L. Epstein, M. Grossman, J.C. Gee, Symmetric diffeomorphic image registration with cross-correlation: evaluating automated labeling of elderly and neurodegenerative brain, Med. Image Anal. 12 (2008) 26–41. https://doi.org/10.1016/j.media.2007.06.004.
[61] J. Ashburner, A fast diffeomorphic image registration algorithm, NeuroImage. 38 (2007) 95–113. https://doi.org/10.1016/j.neuroimage.2007.07.007.
[62] T. Vercauteren, X. Pennec, A. Perchant, N. Ayache, Diffeomorphic demons: efficient non-parametric image registration, NeuroImage. 45 (2009) S61-72. https://doi.org/10.1016/j.neuroimage.2008.10.040.

[63] M.F. Beg, M.I. Miller, A. Trouvé, L. Younes, Computing Large Deformation Metric Mappings via Geodesic Flows of Diffeomorphisms, Int. J. Comput. Vis. 61 (2005) 139–157. https://doi.org/10.1023/B:VISI.0000043755.93987.aa.
[64] M. Burger, J. Modersitzki, L. Ruthotto, A Hyperelastic Regularization Energy for Image Registration, SIAM J. Sci. Comput. 35 (2013) B132–B148. https://doi.org/10.1137/110835955.
[65] S. Darkner, M.S. Hansen, R. Larsen, M.F. Hansen, Efficient Hyperelastic Regularization for Registration, in: A. Heyden, F. Kahl (Eds.), Image Anal., Springer Berlin Heidelberg, 2011: pp. 295–305.
[66] D. Sun, S. Roth, M.J. Black, Secrets of optical flow estimation and their principles, in: 2010 IEEE Comput. Soc. Conf. Comput. Vis. Pattern Recognit., 2010: pp. 2432–2439. https://doi.org/10.1109/CVPR.2010.5539939.
[67] T. Brox, J. Malik, Large Displacement Optical Flow: Descriptor Matching in Variational Motion Estimation, IEEE Trans. Pattern Anal. Mach. Intell. 33 (2011) 500–513. https://doi.org/10.1109/TPAMI.2010.143.
[68] J.R. Burt, S.L. Zimmerman, I.R. Kamel, M. Halushka, D.A. Bluemke, Myocardial T1 Mapping: Techniques and Potential Applications, RadioGraphics. 34 (2014) 377–395. https://doi.org/10.1148/rg.342125121.
[69] C.M. Kramer, Y. Chandrashekhar, J. Narula, T1 Mapping by CMR in Cardiomyopathy: A Noninvasive Myocardial Biopsy?, JACC Cardiovasc. Imaging. 6 (2013) 532–534. https://doi.org/10.1016/j.jcmg.2013.02.002.
[70] D.R. Messroghli, K. Walters, S. Plein, P. Sparrow, M.G. Friedrich, J.P. Ridgway, M.U. Sivananthan, MyocardialT1 mapping: Application to patients with acute and chronic myocardial infarction, Magn. Reson. Med. 58 (2007) 34–40. https://doi.org/10.1002/mrm.21272.
[71] P. Kellman, M.S. Hansen, T1-mapping in the heart: accuracy and precision, J. Cardiovasc. Magn. Reson. 16 (2014) 1–20. https://doi.org/10.1186/1532-429X-16-2.
[72] M.A. Castro, J. Yao, C. Lee, Y. Pang, E. Baker, J. Butman, D. Thomasson, Improved T 1 mapping by motion correction and template based B 1 correction in 3T MRI brain studies, in: X.P. Hu, A.V. Clough (Eds.), 2009: p. 726202. https://doi.org/10.1117/12.811180.
[73] S. Roujol, M. Foppa, S. Weingärtner, W.J. Manning, R. Nezafat, Adaptive registration of varying contrast-weighted images for improved tissue characterization (ARCTIC): Application to T_1 mapping: Motion Correction for T_1 Mapping, Magn. Reson. Med. 73 (2015) 1469–1482. https://doi.org/10.1002/mrm.25270.
[74] H. Xue, S. Shah, A. Greiser, C. Guetter, A. Littmann, M.-P. Jolly, A.E. Arai, S. Zuehlsdorff, J. Guehring, P. Kellman, Motion correction for myocardial T1 mapping using image registration with synthetic image estimation, Magn. Reson. Med. 67 (2012) 1644–1655. https://doi.org/10.1002/mrm.23153.
[75] S. Nekolla, T. Gneiting, J. Syha, R. Deichmann, A. Haase, T1 maps by K-space reduced snapshot-FLASH MRI, J. Comput. Assist. Tomogr. 16 (1992) 327–332.
[76] H. Xue, A. Greiser, S. Zuehlsdorff, M.-P. Jolly, J. Guehring, A.E. Arai, P. Kellman, Phase-sensitive inversion recovery for myocardial T_1 mapping with motion correction and parametric fitting, Magn. Reson. Med. 69 (2013) 1408–1420. https://doi.org/10.1002/mrm.24385.
[77] S. Robinson, G. Grabner, S. Witoszynskyj, S. Trattnig, Combining phase images from multi-channel RF coils using 3D phase offset maps derived from a dual-echo scan, Magn. Reson. Med. 65 (2011) 1638–1648. https://doi.org/10.1002/mrm.22753.
[78] J. Lee, J. Shin, D.-H. Kim, MR-based conductivity imaging using multiple receiver coils, Magn. Reson. Med. 76 (2016) 530–539. https://doi.org/10.1002/mrm.25891.
[79] J. Shao, S. Rapacchi, K.-L. Nguyen, P. Hu, Myocardial T1 mapping at 3.0 tesla using an inversion recovery spoiled gradient echo readout and bloch equation simulation with slice profile correction (BLESSPC) T1 estimation algorithm: FLASH-MOLLI with BLESSPC T1 Mapping, J. Magn. Reson. Imaging. 43 (2016) 414–425. https://doi.org/10.1002/jmri.24999.
[80] M.S. Sussman, I.Y. Yang, K.-H. Fok, B.J. Wintersperger, Inversion group (IG) fitting: A new T_1 mapping method for modified look-locker inversion recovery (MOLLI) that allows arbitrary inversion groupings and rest periods (including no rest period): IG MOLLI Fitting Algorithm for Arbitrary Groupings, Magn. Reson. Med. 75 (2016) 2332–2340. https://doi.org/10.1002/mrm.25829.
[81] K. Chow, J.A. Flewitt, J.D. Green, J.J. Pagano, M.G. Friedrich, R.B. Thompson, Saturation recovery single-shot acquisition (SASHA) for myocardial T_1 mapping: SASHA for T_1 Mapping, Magn. Reson. Med. 71 (2014) 2082–2095. https://doi.org/10.1002/mrm.24878.
[82] M. Doneva, P. Börnert, H. Eggers, C. Stehning, J. Sénégas, A. Mertins, Compressed sensing reconstruction for magnetic resonance parameter mapping, Magn. Reson. Med. 64 (2010) 1114–1120. https://doi.org/10.1002/mrm.22483.

[83] J.V. Velikina, A.L. Alexander, A. Samsonov, Accelerating MR parameter mapping using sparsity-promoting regularization in parametric dimension: Accelerating MR Parameter Mapping, Magn. Reson. Med. 70 (2013) 1263–1273. https://doi.org/10.1002/mrm.24577.
[84] D.H.J. Poot, S. Klein, Detecting statistically significant differences in quantitative MRI experiments, applied to diffusion tensor imaging, IEEE Trans. Med. Imaging. 34 (2015) 1164–1176. https://doi.org/10.1109/TMI.2014.2380830.
[85] F. Odille, J.-M. Escanyé, D. Atkinson, L. Bonnemains, J. Felblinger, Nonrigid registration improves MRI T_2 quantification in heart transplant patient follow-up: Registration of Heart Transplant T_2 Data, J. Magn. Reson. Imaging. 42 (2015) 168–174. https://doi.org/10.1002/jmri.24741.
[86] K. LEVENBERG, A METHOD FOR THE SOLUTION OF CERTAIN NON-LINEAR PROBLEMS IN LEAST SQUARES, Q. Appl. Math. 2 (1944) 164–168.
[87] D.W. Marquardt, An Algorithm for Least-Squares Estimation of Nonlinear Parameters, J. Soc. Ind. Appl. Math. 11 (1963) 431–441. https://doi.org/10.1137/0111030.
[88] J.J. Moré, The Levenberg-Marquardt algorithm: Implementation and theory, in: G.A. Watson (Ed.), Numer. Anal., Springer Berlin Heidelberg, Berlin, Heidelberg, 1978: pp. 105–116. http://link.springer.com/10.1007/BFb0067700 (accessed August 16, 2016).
[89] F. Odille, J.A. Steeden, V. Muthurangu, D. Atkinson, Automatic segmentation propagation of the aorta in real-time phase contrast MRI using nonrigid registration, J. Magn. Reson. Imaging. 33 (2011) 232–238. https://doi.org/10.1002/jmri.22402.
[90] P.F. Felzenszwalb, D.P. Huttenlocher, Efficient Graph-Based Image Segmentation, Int. J. Comput. Vis. 59 (2004) 167–181. https://doi.org/10.1023/B:VISI.0000022288.19776.77.
[91] L. Bonnemains, T. Villemin, J.-M. Escanye, G. Hossu, F. Odille, F. Vanhuyse, J. Felblinger, P.-Y. Marie, Diagnostic and prognostic value of MRI T2 quantification in heart transplant patients, Transpl. Int. 27 (2014) 69–76. https://doi.org/10.1111/tri.12222.
[92] A.V. Knyazev, I. Lashuk, Steepest Descent and Conjugate Gradient Methods with Variable Preconditioning, SIAM J. Matrix Anal. Appl. 29 (2008) 1267–1280. https://doi.org/10.1137/060675290.
[93] G. Salvo, V. Pergola, B. Fadel, Z. Bulbul, P. Caso, Strain echocardiography and myocardial mechanics: From basics to clinical applications, J. Cardiovasc. Echography. 25 (2015) 1. https://doi.org/10.4103/2211-4122.158415.
[94] O.A. Smiseth, H. Torp, A. Opdahl, K.H. Haugaa, S. Urheim, Myocardial strain imaging: how useful is it in clinical decision making?, Eur. Heart J. 37 (2016) 1196–1207. https://doi.org/10.1093/eurheartj/ehv529.
[95] Association Between Layer-Specific Longitudinal Strain and Risk Factors of Heart Failure and Dyspnea: A Population-Based Study - Journal of the American Society of Echocardiography, (n.d.). https://www.onlinejase.com/article/S0894-7317(19)30152-X/fulltext (accessed May 25, 2019).
[96] J.-O. Choi, S.W. Cho, Y.B. Song, S.J. Cho, B.G. Song, S.-C. Lee, S.W. Park, Longitudinal 2D strain at rest predicts the presence of left main and three vessel coronary artery disease in patients without regional wall motion abnormality, Eur. J. Echocardiogr. J. Work. Group Echocardiogr. Eur. Soc. Cardiol. 10 (2009) 695–701. https://doi.org/10.1093/ejechocard/jep041.
[97] G. Nigro, L.I. Comi, L. Politano, R.J. Bain, The incidence and evolution of cardiomyopathy in Duchenne muscular dystrophy, Int. J. Cardiol. 26 (1990) 271–277.
[98] A. Fayssoil, S. Abasse, K. Silverston, Cardiac Involvement Classification and Therapeutic Management in Patients with Duchenne Muscular Dystrophy, J. Neuromuscul. Dis. 4 (n.d.) 17–23. https://doi.org/10.3233/JND-160194.
[99] E. Imbalzano, C. Zito, S. Carerj, G. Oreto, G. Mandraffino, M. Cusmà-Piccione, G. Di Bella, C. Saitta, A. Saitta, Left Ventricular Function in Hypertension: New Insight by Speckle Tracking Echocardiography: Preclinical Systolic Dysfunction in Hypertension, Echocardiography. 28 (2011) 649–657. https://doi.org/10.1111/j.1540-8175.2011.01410.x.
[100] W.H. Jo, L.Y. Eun, J.W. Jung, J.Y. Choi, S.W. Gang, Early Marker of Myocardial Deformation in Children with Duchenne Muscular Dystrophy Assessed Using Echocardiographic Myocardial Strain Analysis, Yonsei Med. J. 57 (2016) 900–904. https://doi.org/10.3349/ymj.2016.57.4.900.
[101] K. Mori, Y. Hayabuchi, M. Inoue, M. Suzuki, M. Sakata, R. Nakagawa, S. Kagami, K. Tatara, Y. Hirayama, Y. Abe, Myocardial strain imaging for early detection of cardiac involvement in patients with Duchenne's progressive muscular dystrophy, Echocardiogr. Mt. Kisco N. 24 (2007) 598–608. https://doi.org/10.1111/j.1540-8175.2007.00437.x.
[102] K.N. Hor, J. Wansapura, L.W. Markham, W. Mazur, L.H. Cripe, R. Fleck, D.W. Benson, W.M. Gottliebson, Circumferential strain analysis identifies strata of cardiomyopathy in Duchenne muscular

dystrophy: a cardiac magnetic resonance tagging study, J. Am. Coll. Cardiol. 53 (2009) 1204–1210. https://doi.org/10.1016/j.jacc.2008.12.032.
[103] A. Scatteia, A. Baritussio, C. Bucciarelli-Ducci, Strain imaging using cardiac magnetic resonance, Heart Fail. Rev. 22 (2017) 465–476. https://doi.org/10.1007/s10741-017-9621-8.
[104] Y. Gan, Q. Chen, S. Zhang, S. Ju, Z.-Y. Li, MRI-based strain and strain rate analysis of left ventricle: a modified hierarchical transformation model, Biomed. Eng. OnLine. 14 (2015) S9. https://doi.org/10.1186/1475-925X-14-S1-S9.
[105] K. Mangion, H. Gao, C. McComb, D. Carrick, G. Clerfond, X. Zhong, X. Luo, C.E. Haig, C. Berry, A Novel Method for Estimating Myocardial Strain: Assessment of Deformation Tracking Against Reference Magnetic Resonance Methods in Healthy Volunteers, Sci. Rep. 6 (2016) 38774. https://doi.org/10.1038/srep38774.
[106] H. Gao, A. Allan, C. McComb, X. Luo, C. Berry, Left ventricular strain and its pattern estimated from cine CMR and validation with DENSE, Phys. Med. Biol. 59 (2014) 3637–3656. https://doi.org/10.1088/0031-9155/59/13/3637.
[107] T. Mansi, J.-M. Peyrat, M. Sermesant, H. Delingette, J. Blanc, Y. Boudjemline, N. Ayache, Physically-Constrained Diffeomorphic Demons for the Estimation of 3D Myocardium Strain from Cine-MRI, in: N. Ayache, H. Delingette, M. Sermesant (Eds.), Funct. Imaging Model. Heart, Springer Berlin Heidelberg, Berlin, Heidelberg, 2009: pp. 201–210. https://doi.org/10.1007/978-3-642-01932-6_22.
[108] Current State of Three-Dimensional Myocardial Strain Estimation Using Echocardiography - Journal of the American Society of Echocardiography, (n.d.). http://www.onlinejase.com/article/S0894-7317(12)00795-X/fulltext (accessed March 21, 2017).
[109] R.J. Taylor, W.E. Moody, F. Umar, N.C. Edwards, T.J. Taylor, B. Stegemann, J.N. Townend, K.N. Hor, R.P. Steeds, W. Mazur, F. Leyva, Myocardial strain measurement with feature-tracking cardiovascular magnetic resonance: normal values, Eur. Heart J. – Cardiovasc. Imaging. 16 (2015) 871–881. https://doi.org/10.1093/ehjci/jev006.
[110] E.J. Keller, S. Fang, K. Lin, B.H. Freed, P.M. Smith, B.S. Spottiswoode, R. Davids, M. Carr, M.-P. Jolly, M. Markl, J.C. Carr, J.D. Collins, The consistency of myocardial strain derived from heart deformation analysis, Int. J. Cardiovasc. Imaging. (2017). https://doi.org/10.1007/s10554-017-1090-6.
[111] M. Carlsson, N.F. Osman, P.C. Ursell, A.J. Martin, M. Saeed, Quantitative MR measurements of regional and global left ventricular function and strain after intramyocardial transfer of VM202 into infarcted swine myocardium, Am. J. Physiol. - Heart Circ. Physiol. 295 (2008) H522–H532. https://doi.org/10.1152/ajpheart.00280.2008.
[112] R. Jasaityte, B. Heyde, V. Ferferieva, B. Amundsen, D. Barbosa, D. Loeckx, G. Kiss, F. Orderud, P. Claus, H. Torp, J. D'hooge, Comparison of a new methodology for the assessment of 3D myocardial strain from volumetric ultrasound with 2D speckle tracking, Int. J. Cardiovasc. Imaging. 28 (2012) 1049–1060. https://doi.org/10.1007/s10554-011-9934-y.
[113] Sato Tomoyuki, Calderon-Anyosa Renzo J, Banerjee Anirban, Abstract 16027: Superiority of 3D Strain Over 2D Strain in Single Right Ventricle of Children, Circulation. 136 (2017) A16027–A16027. https://doi.org/10.1161/circ.136.suppl_1.16027.
[114] J. Nguyen, M. Vezza, R. Mulyala, H. Singh, Comparison of 2d and 3d Strain Using Cardiovascular Magnetic Resonance Feature Tracking, J. Am. Coll. Cardiol. 71 (2019) A1603. https://doi.org/10.1016/S0735-1097(18)32144-2.
[115] A. Satriano, B. Heydari, M. Narous, D.V. Exner, Y. Mikami, M.M. Attwood, J.V. Tyberg, C.P. Lydell, A.G. Howarth, N.M. Fine, J.A. White, Clinical feasibility and validation of 3D principal strain analysis from cine MRI: comparison to 2D strain by MRI and 3D speckle tracking echocardiography, Int. J. Cardiovasc. Imaging. 33 (2017) 1979–1992. https://doi.org/10.1007/s10554-017-1199-7.
[116] M. Rouhani, A.D. Sappa, E. Boyer, Implicit B-Spline Surface Reconstruction, IEEE Trans. Image Process. 24 (2015) 22–32. https://doi.org/10.1109/TIP.2014.2366374.
[117] L.R. Dice, Measures of the Amount of Ecologic Association Between Species, Ecology. 26 (1945) 297–302. https://doi.org/10.2307/1932409.
[118] L.I. Rudin, S. Osher, E. Fatemi, Nonlinear total variation based noise removal algorithms, Phys. Nonlinear Phenom. 60 (1992) 259–268. https://doi.org/10.1016/0167-2789(92)90242-F.
[119] A. Bustin, P. Ferry, A. Codreanu, M. Beaumont, S. Liu, D. Burschka, J. Felblinger, A.C.S. Brau, A. Menini, F. Odille, Impact of denoising on precision and accuracy of saturation-recovery-based myocardial T_1 mapping: Myocardial T_1 Mapping Denoising, J. Magn. Reson. Imaging. (2017). https://doi.org/10.1002/jmri.25684.

[120] L. Bonnemains, A.S. Guerard, P. Soulié, F. Odille, J. Felblinger, Myocardial volume change during cardiac cycle derived from three orthogonal systolic strains: towards a quality assessment of strains, Acta Radiol. Stockh. Swed. 1987. 60 (2019) 286–292. https://doi.org/10.1177/0284185118783777.

[121] X. Papademetris, A.J. Sinusas, D.P. Dione, R.T. Constable, J.S. Duncan, Estimation of 3-D left ventricular deformation from medical images using biomechanical models, IEEE Trans. Med. Imaging. 21 (2002) 786–800. https://doi.org/10.1109/TMI.2002.801163.

[122] P. Fischer, A. Dosovitskiy, E. Ilg, P. Häusser, C. Hazırbaş, V. Golkov, P. van der Smagt, D. Cremers, T. Brox, FlowNet: Learning Optical Flow with Convolutional Networks, ArXiv150406852 Cs. (2015). http://arxiv.org/abs/1504.06852 (accessed June 21, 2019).

[123] E. Ilg, N. Mayer, T. Saikia, M. Keuper, A. Dosovitskiy, T. Brox, FlowNet 2.0: Evolution of Optical Flow Estimation with Deep Networks, ArXiv161201925 Cs. (2016). http://arxiv.org/abs/1612.01925 (accessed June 21, 2019).

List of Figures

List of Tables

List of publications

Journal papers

Shufang Liu, Aurelien Bustin, Pauline Ferry, Andrei Codreanu, Darius Burschka, Anne Menini, Freddy Odille. : "A vectorized Levenberg-Marquardt model fitting algorithm for efficient post-processing of cardiac T1 mapping MRI". Computers in Biology and Medicine, Page 106-115, Volumn 96,2018.

Bustin A, Ferry P, Codreanu A, Beaumont M, **Liu Shufang**, Burschka D, Felblinger J, Brau A, Menini A, Odille F. Impact of a Joint Anisotropic Denoising Technique on Precision and Accuracy of Myocardial T1 Mapping. Journal of Magnetic Resonance Imaging. 2017 Nov;46(5):1377-1388. doi: 10.1002/jmri.25684. Epub 2017 Apr 4.

Odille F, Bustin A, **Liu S**, Chen B, Vuissoz PA, Felblinger J, Bonnemains L. Isotropic 3D cardiac cine MRI allows efficient sparse segmentation strategies based on 3D surface reconstruction. Magn Reson Med. 2018 May;79(5):2665-2675. doi: 10.1002/mrm.26923. Epub 2017 Oct 2.

Conference papers

S Liu, A Bustin, D Burschka, A Menini, F Odille. GPU Implementation of Levenberg-Marquardt Optimization for T1 Mapping Inproceedings. 2017 Computing in Cardiology (CinC), pp. 1-4, 2017, ISSN: 2325-887X. **Oral presentation and CINC Young Investigator Award Finalist.**

Liu S., Zhang L., Ferry P., Codreanu A., Menini A., Odille F.: "A Robust Motion Correction Tool for Cardiac Extracellular Volume Mapping". ISMRM, Singapore, 2016. May 7th-13th, 2016 (Participation and Poster Presentation)

Bustin A., Menini A., **Liu S**., Rincon T., Burschka D., Janich M,. Wolff S., Shubayev O., Stanley D., Odille F., Brau A.: "Motion Compensated Reconstruction in Accelerated Single-Shot Cardiac MRI". ISMRM, Toronto, 2015. May 30th- June 5th, 2015 (Co-authorship of Poster)

Bustin A, Menini A, **Liu S**, Burschka D, Codreanu A, Al-Mallah M, Janich M, Brau A, Odille F. Saturation-based Myocardial T1 Mapping with Denoising: Initial Comparative Study with MOLLI. Journal of Cardiovascular Magnetic Resonance, x(Supplx):Px, 2017.

Ferry P, Codreanu A, **Liu S**, Bustin A, Brau A, Beaumont M, Martin J, Glenn S. T1 Mapping in healthy subjects using SMART1Map at 3T: a Comparison with MOLLI. Journal of Cardiovascular Magnetic Resonance, x(Suppl x):Px, 2017.

F Odille, **S Liu**, P van Dam, J Felblinger. Statistical variations of heart orientation in healthy adults Inproceedings. 2017 Computing in Cardiology (CinC), pp. 1-4, 2017, ISSN: 2325-887X.

Odille F, **Liu S**, Bustin A, Felblinger J, Bonnemains L: "Strain measurements from 3D isotropic cine MRI: Relation with fibrosis in a Duchenne patient population". ISMRM, Paris, 2018. June 16th-21th, 2018 (Participation and Poster Presentation)

Appendix I

A software for clinical study purpose is implemented. The software integrated non-registration module, de-noise module and curve fitting module. It allows flexible choose processing steps, eg. including/removing processing steps or add additional steps. Regional result and point result can be reported.